MEASUREMENT OF CAROTID ARTERY WALL THICKNESS AND DIAMETERS FROM MAGNETIC RESONANCE AND ULTRASOUND IMAGES

A THESIS

Submitted in partial fulfillment of the requirements for the degree of

DOCTOR OF PHILOSOPHY

by

KRISHNA KUMAR P

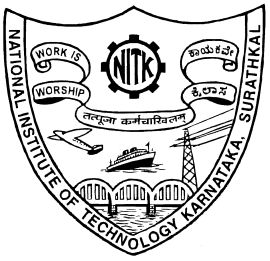

DEPARTMENT OF COMPUTER SCIENCE AND ENGINEERING

NATIONAL INSTITUTE OF TECHNOLOGY KARNATAKA
SURATHKAL, MANGALORE - 575025, INDIA

November 2017

DECLARATION

I hereby ***declare*** that the Research Thesis entitled **MEASUREMENT OF CAROTID ARTERY WALL THICKNESS AND DIAMETERS FROM MAGNETIC RESONANCE AND ULTRASOUND IMAGES** which is being submitted to the ***National Institute of Technology Karnataka, Surathkal*** in partial fulfillment of the requirements for the award of the Degree of ***Doctor of Philosophy*** is a ***bona fide report of the research work carried out by me***. The material contained in this thesis has not been submitted to any University or Institution for the award of any degree.

KRISHNA KUMAR P
Register No.: CS13F04
Department of Computer Science and Engineering

Place: NITK - Surathkal

Date:

CERTIFICATE

This is to *certify* that the Research Thesis entitled **MEASUREMENT OF CAROTID ARTERY WALL THICKNESS AND DIAMETERS FROM MAGNETIC RESONANCE AND ULTRASOUND IMAGES**, submitted by **Krishna Kumar P** (Register Number: CS13F04) as the record of the research work carried out by him, is *accepted* as the *Research Thesis submission* in partial fulfillment of the requirements for the award of degree of ***Doctor of Philosophy***.

Dr. Jeny Rajan
Research Guide
Assistant Professor
Department of Computer Science and Engineering
NITK Surathkal - 575025

Chairman - DRPC
(Signature with Date and Seal)

This thesis is
dedicated to
My Mother

ACKNOWLEDGEMENTS

It would not have been possible to write this doctoral thesis without the help and support of the kind people around me, to only some of whom it is possible to give particular mention here.

First and foremost, I want to offer this endeavour to the GOD Almighty for the wisdom she bestowed upon me, the strength, peace of mind and good health in order to furnish this research. I would like to express my gratitude towards my family for the encouragement which helped me in completion of this thesis.

I take this opportunity to thank Department of Computer Science and Engineering, National Institute of Technology, Karnataka for providing the facility to carry out my research work.

It is a genuine pleasure to express my deep sense of thanks and gratitude to my mentor, philosopher and guide Dr. Jeny Rajan, Department of Computer Science and Engineering, National Institute of Technology, Karnataka. His dedication and keen interest on me at every stage of my research had been solely responsible for completing my work.

I owe a deep sense of gratitude to Dr. Jasjit Suri, Stroke Monitoring Division, AtheroPoint, Roseville, CA, USA, and Dr. C Kesavadas, Department of Imaging Sciences and Interventional Radiology, Sree Chitra Tirunal Institute of Medical Sciences and Technology Trivandrum, Kerala for their help in collecting data, timely suggestions with kindness and enthusiasm.

I would like to thank my committee members, Dr. Jidesh P, Department of Mathematics and Dr. Shashidhar G Koolagudi, Department of Computer Science and Engineering, National Institute of Technology, Karnataka for their advice and unsurpassed knowledge.

Last but not least, I would like to thank my friends and colleagues at the National Institute of Technology, Karnataka for their encouragement and moral support which made my stay and studies in Surathkal more enjoyable.

(Krishna Kumar P)

ABSTRACT

One of the most common causes of cardiovascular diseases (CVD) is atherosclerosis which is the continuous build-up of fatty deposits (plaques) on the inner walls of the blood vessels (arteries). The incidence of ischemic strokes is highly associated with the rupture of atherosclerotic plaques in the common carotid artery (CCA). To assess carotid atherosclerosis, non-invasive imaging modalities such as magnetic resonance (MR) and ultrasound (US) imaging are preferred over other invasive methods due to their safer profile and ability to explore atherosclerosis in its early stages. It has been increasingly accepted that the wall thickness and diameter measurements of the CCA can serve as early indicators of CVD development. However, manual measurement of these quantities is tedious, error-prone and subjected to observer variability. Hence, there is a growing interest for the development of automated software systems for the measurement of wall thickness and diameters of the CCA from MR and US images. The development of such automated systems was the primary objective of this research.

MR and US images are generally corrupted with noise which makes their interpretation and further processing difficult. This necessitates the task of denoising as a pre-processing stage which can improve the performance of image segmentation techniques. For this reason, a robust denoising filter (NLML_{DCT}) has been proposed in this thesis to reduce the Rician noise in MR images by integrating discrete cosine transform into the conventional non-local maximum likelihood (NLML) method. Whereas, one of the widely accepted method named OBNLM is adopted in our work to reduce the speckle noise in US images.

We have proposed novel algorithms for delineation of the carotid artery borders from MR and US images. The wall thickness of the CCA has been measured from T1-

weighted MR images using an active contour method combined with localized particle swarm optimization. This combination of global and localized segmentation strategy helped us to reduce the edge leaking problem to some extent. Due to better reliability, the diameters of the CCA have been measured from B-mode US images via a region-based approach. For this measurement, we have delineated the lumen-intima and media-adventitia borders of the CCA using a scale-space based strategy. This automated segmentation system has been further improved using an iterative spatial transformation based technique for handling curved vessels. Comprehensive statistical data analysis was performed to ensure the superior performance of the proposed techniques against the manual expert tracings.

Keywords: Carotid Artery; MRI; Ultrasound; Denoising; Segmentation.

TABLE OF CONTENTS

ACKNOWLEDGEMENTS **ii**

ABSTRACT **iii**

LIST OF TABLES **viii**

LIST OF FIGURES **xi**

ABBREVIATIONS **xii**

1 INTRODUCTION **1**

1.1 Imaging of Cardiovascular Diseases: Background 1

1.1.1 Risk of cardiovascular diseases 1

1.1.2 Imaging Modalities for Carotid Atherosclerosis 3

1.1.3 A Brief Review of MR and US Imaging with Basic Principles 5

1.1.4 Wall thickness and Diameters of the Carotid Artery 7

1.1.5 Significance of MR and US Image Denoising 8

1.2 Motivation 9

1.3 Problem Statement 9

1.4 Research Objectives 10

1.5 Major Contributions of the Thesis 11

1.6 Organization of the Thesis 11

2 CAROTID ARTERY SEGMENTATION APPROACHES **13**

2.1 MR and US for Carotid Artery Imaging 13

2.2 Segmentation from MR Images 14

2.3 Segmentation from US Images 18
2.3.1 General Framework for Carotid Artery Segmentation 21
2.3.2 Challenges during Segmentation 32
2.3.3 Validation Metrics 36
2.4 Summary 40

3 MAGNETIC RESONANCE IMAGE DENOISING AND MEASUREMENT OF CAROTID ARTERY WALL THICKNESS 41

3.1 DCT Based NLML Filter for MR Image Denoising 42
3.1.1 Data Distribution and Signal Estimation in MRI 44
3.1.2 Signal Estimation using NLML Method 45
3.1.3 NLML$_{DCT}$ Filter for MR Image Denoising 46
3.1.4 Experimental Results 47
3.2 Carotid Artery Wall Segmentation from MRI 57
3.2.1 Global Region based Lumen Segmentation 57
3.2.2 Morphological Gradient 60
3.2.3 PSO based Localized Outer Wall Segmentation 61
3.2.4 Experimental Results 62
3.3 Summary 68

4 MEASUREMENT OF ARTERIAL DIAMETERS FROM CAROTID ULTRASOUND IMAGES 69

4.1 Speckle Noise in US Images 69
4.2 Automated Carotid Lumen Segmentation System 70
4.2.1 Scale-Space based Global Segmentation 72
4.2.2 Region based Local Shape Extraction 73
4.3 Improved System for LD Measurement in Curved Vessels 73
4.3.1 Spatial Transformation 76
4.4 Experimental Results 80
4.4.1 Dataset 80

4.4.2 Evaluation Methodology 80
4.4.3 Results and Analysis 81
4.5 Discussion 88
4.6 Summary 89

5 CLINICAL SIGNIFICANCE AND IMPLICATIONS OF CAROTID ARTERIAL DIAMETERS 91

5.1 Clinical Significance of LD and IAD 91
5.2 Relationship of Carotid Arterial Diameters and Plaque Score 93
5.2.1 Correlation between LD/IAD and Plaque Score 93
5.3 Computation of Stenosis Severity Index 96
5.4 Summary 97

6 CONCLUSIONS AND FUTURE WORK 99

6.1 Conclusions 99
6.2 Future Work 101

APPENDIX 103

A Polyline Distance Metric and Precision of Merit 103

A.1 Polyline Distance Metric 103
A.2 Precision of Merit 104

REFERENCES 105

LIST OF TABLES

2.1 Overview of region-based techniques proposed in the literature . . . 27

2.2 Overview of boundary-based techniques proposed in the literature . 31

3.1 NLML$_{DCT}$ Denoising Algorithm 47

3.2 Time Complexity Analysis of Denoising Algorithms 48

3.3 Quantitative analysis on experimental Kiwi fruit image 53

3.4 Performance of Auto CAWT against Manual CAWT 65

3.5 Dice similarity and Jaccard index 65

3.6 Previous studies describing carotid artery segmentation methods . . 67

4.1 Algorithm for Spatial Transformation 77

4.2 Auto LD Performance 83

4.3 Auto IAD Performance 83

4.4 Dice similarity and Jaccard index for LR 83

4.5 Dice similarity and Jaccard index for IAR 84

4.6 T - test for Auto LD vs. Manual tracings 88

4.7 T - test for Auto IAD vs. Manual tracings 88

5.1 Risk analysis based on SSI 97

LIST OF FIGURES

1.1 Illustrating the common carotid artery and its main branches (Staff, 2014). 3

1.2 Lumen-intima (LI) and media-adventitia (MA) interfaces of the carotid artery in B-mode US image. 7

2.1 General flow diagram showing segmentation of the carotid MR images. 15

2.2 Meijer Carotid Arc: illustrates the standardized approach for carotid ultrasound scanning which will give a set of reproducible images. Reprinted from (Stein *et al.*, 2008), with permission from Elsevier. 20

2.3 General flow diagram showing the region-based and boundary-based lumen segmentation in B-mode US images. 22

2.4 Illustrating the variation of carotid artery images across different patients. (a) Curved lumen diameter (LD) borders; (b) High plaque deposit and narrowing of carotid artery; (c) Low contrast image with jugular vein interference. (d) Image having poor contrast difference at near wall. 34

3.1 Rician Bias : This experiment was conducted with $\sigma_g = 1$ and varying a from 0.5 to 20. 43

3.2 Visual quality comparison: (a) Ground Truth (GT) (b) GT corrupted with noise (with σ_g = 15) (c) noisy image denoised with NLML$_C$ (d) noisy image denoised with NLML$_{DCT}$. 49

3.3 Visual quality comparison : (First column) Ground Truth (Second column) enlarged view of the area marked in red color(Third column) enlarged view after denoised with NLML$_C$ (Fourth column) enlarged view after denoised with NLML$_{DCT}$. 50

3.4 Quantitative analysis : (a) PSNR plot of NLML$_C$ and NLML$_{DCT}$ for various search window size (b) Mean SSIM plot of NLML$_C$ and NLML$_{DCT}$ for various search window size (c) Execution time comparison of NLML$_C$ and NLML$_{DCT}$ for various search window size (d) and (e) Mean SSIM and PSNR plot of NLML$_C$ and NLML$_{DCT}$ after varying σ_g from 10 to 40. 52

3.5 Experiments on real data : **(a)** Noisy carotid MR image **(b)** Denoised with NLML_C **(c)** Denoised with NLML_{DCT}, **(d)**enlarged view of the region marked in red in (a), **(e)** and **(f)** enlarged views of the corresponding region marked in red from (b) and (c), **(g)** enlarged view of the region marked in green in (a), **(h)** and **(i)** enlarged views of the corresponding region marked in green from (b) and (c). 55

3.6 Experiments on MR image of a Kiwi fruit : **(a)** Original image reconstructed with 1 average **(b)** Original image reconstructed with 12 averages **(c)** image (a) denoised with NLML_C method **(d)** image (a) denoised with NLML_{DCT} method **(e)** and **(f)** residual images (with respect to (b)) of (c) and (d) (in the scale 0-150). 56

3.7 Flow diagram showing the segmentation of inner and outer walls of the carotid artery from MR images. 58

3.8 Segmentation results using the proposed method: (a) Denoised MR image of the carotid artery b) Cropped ROI c) Automated lumen border (d) Morphological gradient (e) PSO output f) Automated Outer wall border (g) Overlays on ROI (h) Overlays on raw image. 63

4.1 Flow diagram of the region based approach for lumen segmentation. 71

4.2 Segmentation results on a single image: (a) Cropped image (b) bright adventitial border points detected using vertical profile analysis (c) Spline fitted on these points to show the adventitial borders (d) the resulting ROI is marked with a rectangle extracted using global-shape extraction system (e) binary lumen obtained from the classifier in the ROI using local region-based system (f) final lumen borders after smoothing and spline fitting. 74

4.3 Flow diagram of the iterative lumen delineation system. 75

4.4 Flow diagram of the stage-2 of the automated lumen delineation system. 76

4.5 Illustrating the algorithmic steps on a single image having curvature. (a) Curved ROI, (b) Lumen axis on the ROI, (c) Transformed ROI, (d) Adventitial borders on the transformed ROI, (e) Binary lumen from classifier, (f) LD borders on the transformed ROI, (g) LD borders on the inverse transformed ROI, (h) LD borders on the original ROI. 78

4.6 Carotid Auto LD borders compared against the manual tracings on the grayscale images of four patients for both simple scale-space and transformation based iterative methods. Carotid Auto LD borders are shown in solid white; while manual LD borders are shown in dashed white (Auto SS Automated Simple scale-space, Auto SST Automated scale-space with Transformation, Reader Manual Reader). 79

4.7 Scatter diagrams showing the correlation between (a) carotid Auto SS LD and manual-1 LD, (b) carotid Auto SS LD and manual-2 LD, (c) carotid Auto SST LD and manual-1 LD, (d) carotid Auto SST LD and manual-2 LD. 85

4.8 Bland-Altman plots between (a) carotid Auto SS LD and manual-1 LD, (b) carotid Auto SS LD and manual-2 LD, (c) carotid Auto SST LD and manual-1 LD, (d) carotid Auto SST LD and manual-2 LD. 86

4.9 Scatter diagrams showing the correlation between (a) carotid Auto SS IAD and manual-1 IAD, (b) carotid Auto SS IAD and manual-2 IAD. Bland-Altman plots between (c) carotid Auto SS IAD and manual-1 IAD, (d) carotid Auto SS IAD and manual-2 IAD. 87

5.1 (a) Scatter diagram showing the positive correlation between Auto LD and PS (b) Auto IAD and PS; (c) Bland-Altman plot of PS with Auto LD (d) PS with Auto IAD. 95

5.2 Representative image of a patient with high stroke risk (SSI = 55%). 98

5.3 (a) Cumulative frequency plot of SSI, (b) Scatter diagram showing the negative correlation between Mean carotid Auto LD and SSI. 98

ABBREVIATIONS

ACM	Active Contour Model
ASM	Active Shape Model
CAWT	Carotid Artery Wall Thickness
CC	Coefficient of Correlation
CCA	Common Carotid Artery
CT	Computed Tomography
CVD	Cardio Vascular Disease
DCT	Discrete Cosine Transform
DDC	Discrete Dynamic Contour
DSC	Dice Similarity Coefficient
DSA	Digital Subtraction Angiography
DP	Dynamic Programming
ECA	External Carotid Artery
ECST	European Carotid Surgery Trial
GT	Ground Truth
HT	Hough's Transform
IAD	Inter-Adventitial Diameter
ICA	Internal Carotid Artery
IMT	Intima-Media Thickness
IVUS	Intravascular Ultrasound
JI	Jaccard Index
JV	Jugular Vein
LD	Lumen Diameter
LI	Lumen-Intima

LSM	Level Set Method
MA	Media-Adventitia
MAD	Mean Absolute Distance
MRA	Magnetic Resonance Angiography
MG	Morphological Gradient
MRI	Magnetic Resonance Imaging
MWT	Mean Wall Thickness
NASCET	North American Symptomatic Carotid Endarterectomy Trial
NLM	Non Local Means
NLML	Non Local Maximum Likelihood
OEM	Original Equipment Manufacturer
PDF	Probability Density Function
PDM	Polyline Distance Metric
PET	Positron Emission Tomography
PoM	Precision of Merit
PS	Plaque Score
PSNR	Peak Signal to Noise Ratio
PSO	Particle Swarm Optimization
RANSAC	Random Sample Consensus
ROC	Receiver Operating Characteristic
ROI	Region of Interest
SNR	Signal to Noise Ratio
SSI	Stenosis Severity Index
SSIM	Structural Similarity Index Matrix
US	Ultrasound
WHO	World Health Organization

CHAPTER 1

INTRODUCTION

The area of medical image processing has undergone a dramatic expansion in the last decade and has already become an important part of clinical routine. Computer softwares assist physicians in the interpretation of medical images. Imaging techniques such as X-ray, magnetic resonance imaging (MRI), and ultrasound (US) imaging yield a great deal of information, which the radiologist has to analyze and evaluate comprehensively in a short time. Early detection of the disease will allow the physicians to follow up on the patient. Hence, the goal is to derive better tools that help to interpret the images.

In this Chapter, we present a brief overview of different medical image processing techniques associated with the analysis of cardiovascular diseases (CVD). In Section 1.1 we present the original aspects of this work and explain how image processing helps in the assessment of the risk of CVDs. Section 1.2 presents the motivation for the proposed work. In Section 1.3, we describe the problem statement which is followed by research objectives in Section 1.4. Section 1.5 explains the major contributions of this thesis. Finally, in Section 1.6, a guide to this thesis contents is presented.

1.1 Imaging of Cardiovascular Diseases: Background

1.1.1 Risk of cardiovascular diseases

Cardiovascular diseases (CVD) such as stroke and heart attack are identified as the number one cause of human deaths worldwide. A report of the world health organization (WHO) published in 2012 says that approximately 17.5 million people are died because

of CVDs (i.e. 31% of all global deaths). Out of them, around 6.7 million people were died due to stroke. Moreover it is estimated that, by 2030, over 23 million people will die from CVDs each year since most of the low to middle income countries are seriously affected by CVDs (WHO, 2016). Further in near future, the South Asian subcontinent will have to carry around 60% of the world's CVD burden despite only accounting for 20% of the world's population (IHA, 2015).

The major risk factors of CVD events include age, gender, family history, excessive use of tobacco and alcohol, unhealthy diet, obesity, physical inactivity, hypertension, diabetes and hyperlipidaemia (Organization and UNAIDS, 2007). However, one of the most common reasons for CVDs is atherosclerosis which is the continuous build-up of fatty deposits (plaques) on the inner walls of the vessels (arteries) that supply blood to the heart or brain. This significantly reduces the blood flow and causes inflammation in the arterial wall (Woollard and Geissmann, 2010). Atherosclerosis may be present in different sites of the body, including the coronary arteries, the superficial femoral artery, the aorta, and the carotid arteries.

The incidence of ischemic stroke is highly associated with the rupture of atherosclerotic plaques in the carotid artery which are located at both sides of the neck (Carr *et al.*, 1996). Carotid arteries are responsible for supplying blood to the brain and muscles of the face. Each carotid starts as a common carotid artery (CCA), which forks into two branches: internal carotid artery (ICA) and external carotid artery (ECA) (see Figure 1.1). The risk of stroke increases with the severity of carotid stenosis (the narrowing of the artery caused by plaque). Atherosclerosis changes the mechanical properties of the carotid artery wall by making it stiffer (Lamont *et al.*, 2000). The accumulated plaque causes narrowing or constriction of the inner surface (lumen) of the carotid artery which in turn results in irregularity of the artery (Mughal *et al.*, 2011). The degree of luminal narrowing is considered as an indirect measure of stenosis severity due to carotid atherosclerosis.

Several studies have demonstrated that patients with carotid atherosclerotic plaques

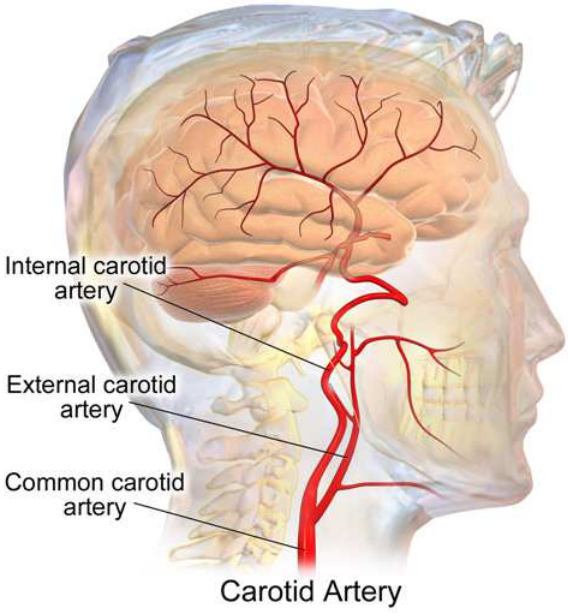

Figure 1.1: Illustrating the common carotid artery and its main branches (Staff, 2014).

carry an increased risk of cardiovascular events (Hollander *et al.*, 2002; Grønholdt *et al.*, 2001; Nambi *et al.*, 2010). Further, coronary plaque vulnerability may be assessed by evaluating plaque characteristics in the carotid arteries (Naghavi *et al.*, 2003). Currently, identifying patients that are having plaques in the coronary artery is challenging. Moreover, the intima-media thickness (IMT) and diameter measurements of carotid arteries are proved to be associated with both coronary risk factors and CVDs (Kablak-Ziembicka *et al.*, 2004; Bots *et al.*, 1997). Hence, monitoring of the changes occurring in the carotid artery via imaging techniques may provide us a new clinical and practical strategy to treat patients with severe cardiovascular complications. Further, this will assist in the effective management of the atherosclerotic disease patients (Suri *et al.*, 2010). To assess carotid atherosclerosis, different imaging techniques have been used.

1.1.2 Imaging Modalities for Carotid Atherosclerosis

Atherosclerosis imaging encompasses several established techniques and experimental radiological methods and modalities. These include Digital Subtraction Angiography

(DSA), Computed Tomography (CT), Positron Emission Tomography (PET), MRI, and US imaging (Saba *et al.*, 2014*b*). These techniques aid in the detection and diagnosis of atherosclerosis and provide detail on arterial morphology. Further, this helps to assess the disease severity which is indispensable to everyday clinical practice and cardiovascular research. For example, DSA allows clear visualization of blood vessels in a bony or dense soft tissue environment. CT assists in the visualization of the artery morphology and the stenosis whereas PET provides a non-invasive method to measure biological processes that are relevant to atherosclerosis (Gillard *et al.*, 2006). However, there is no single imaging modality that can produce definitive information about the state of atherosclerosis and each technique has its own drawback. Some may be invasive in nature, use ionizing radiation, inject contrast agents, low patient tolerability, or simply the insufficiency of information obtained.

It is unquestionable that every imaging modality is limited by differing degrees of technical difficulty, in addition to potential adverse effects and costs. However, the use of imaging modalities such as MR and US imaging are preferred over other invasive and non-invasive methods for the assessment of atherosclerotic plaque burden (Blum and Nahir, 2013). This is due to their safer profile, especially regarding their use in asymptomatic populations (Achenbach *et al.*, 2001; Ibáñez *et al.*, 2007). Further, these modalities have the ability to explore atherosclerosis in its early stages. This is the reason why imaging of atherosclerosis by MRI and US is widely accepted today for the mass screening of asymptomatic patients. MRI provides high-resolution images of the carotid artery without involving ionizing radiation which can be repeated sequentially over time. The MR imaging is based on the radio frequency signal and offer important diagnostic information that cannot be obtained with the use of other imaging techniques (Orel and Schnall, 2001). However, there are certain risks involved in doing MRI on people with prostheses, artificial heart valves, implants, or any metal device in their body. This is because that MR imaging needs highly powerful magnets as part of the imaging process. In addition to that, patients with a pacemaker cannot be recommended for MRI. These adverse effects together with high cost of imaging make it necessary to

have another alternative imaging technique. Non-invasive and inexpensive US imaging could be a better choice in this regard. US is recognized as a simple and rapid imaging method which allows real-time dynamic examination of the carotid artery (Sidhu, 2000). However, difficulty in imaging deeper structures, operator-dependency and poor repeatability are the main drawbacks identified with US imaging (Patil and Dasgupta, 2012). However, it is reassuring to see that recent studies have established moderate to good inter-observer reliability and advances in technology allows increased resolution for the transducers. Hence, MR and US imaging together have emerged as the leading non-invasive imaging modalities for atherosclerotic diagnosis. The basic acquisition principles of these two techniques along with their applicability in carotid imaging are discussed in the next section.

1.1.3 A Brief Review of MR and US Imaging with Basic Principles

MRI is a unique tool which provides high resolution images of the carotid artery using radio frequency waves. These radio frequency signals are typically generated from hydrogen atoms (protons) in the water which are present in plenty inside the human body. The subject (patient) will be placed in a strong magnetic field with the application of a radio frequency pulse. This causes the spin of the hydrogen nuclei to align in a specific direction which later release radio signals when the magnetic field gets turned off. These radio signals are captured using a scanner and fed into a computer which translates them to 2D/3D MR images. The emitted radio signal from different body tissues varies according to the water concentration in the tissue and the relaxation times (T1 and T2). Thus, we obtain different signal intensities for T1-weighted, T2-weighted, and proton-density-weighted MR images. MRI has the ability to distinguish the boundaries of the carotid artery with good reproducibility and can assist in plaque characterization (Yuan *et al.*, 2008). Further, the measurement of carotid artery wall thickness (CAWT) can be a useful biomarker for the degree of carotid stenosis (Saba *et al.*, 2014*a*).

Unlike MRI, medical ultrasound or ultrasonography uses high frequency sound

waves ($> 20,000$ HZ) for imaging (Carovac *et al.*, 2011). The sound waves propagate through the human body which are subjected to partial reflection and partial scattering due to the acoustic heterogeneity of different tissues (fat, muscle cells, cysts, blood vessels etc.). Based on the time of arrival of reflected waves, the depth of penetration can be measured which will be processed to form an image (Treeby *et al.*, 2012). The speed of sound wave varies in relation to the change in elasticity or mechanical weakening of arteries. Elasticity is directly related to the sound speed as given by Newton-Laplace equation as (Rayleigh, 1945):

$$c = \sqrt{\frac{K}{\rho}} \tag{1.1}$$

where c, K and ρ are the sound speed, elastic modulus and density, respectively. For example, the speed is found to be highest for calcified plaque and lowest in the fatty plaque (AbuRahma *et al.*, 2002). Similarly, different tissues reflect varying degrees of sound (sound echoes) which were recorded and displayed as an image. The simplest type of US is A-mode (amplitude mode) which is used for diagnosis in ophthalmology (Lizzi and Coleman, 2004). Other common types of US include Doppler US (display blood flow through vessels), intravascular ultrasound or IVUS (give inside view of blood vessels), ultrasonic elastography (to measure stiffness of tissue) and 3D-US (Weismann *et al.*, 2011). However, the most well-known type is B-mode (brightness mode) US image, which displays the acoustic impedance of a two-dimensional cross-section of a tissue. Here, the intensity of the echo is represented by modulation of the brightness of the spot, while the position of the echo is determined from the angular position of the transducer and the transit time of the acoustical pulse and its echo. B-mode ultrasonography is widely used in carotid imaging because of its low cost and ability to provide real-time information about both the lumen and vessel wall (Stein *et al.*, 2008).

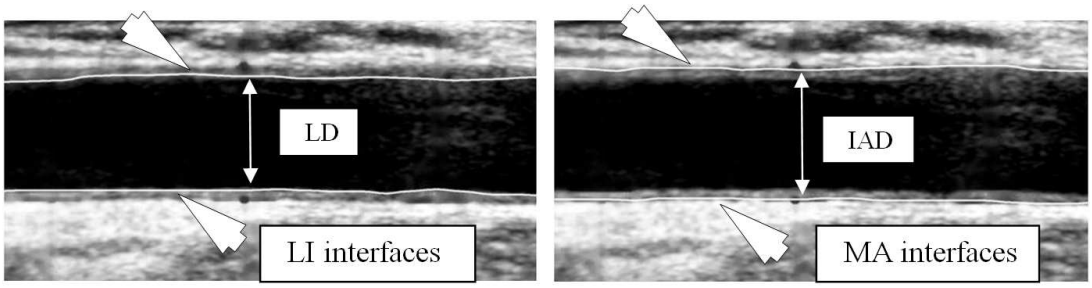

Figure 1.2: Lumen-intima (LI) and media-adventitia (MA) interfaces of the carotid artery in B-mode US image.

1.1.4 Wall thickness and Diameters of the Carotid Artery

It has been increasingly accepted that carotid artery wall thickness and diameter measurements can serve as early indicators of cardiovascular disease development. These parameters are frequently measured in screening tests (examinations performed to detect disease at its earliest stage) for the selection of patients for surgery. An irregular thickening of the carotid artery walls or lumen narrowing may signal the development of atherosclerotic plaques. In addition to this, the wall thickness and diameters of the CCA have been related to several atherosclerosis risk factors and to prevalent and incident coronary artery disease (Wasserman *et al.*, 2005). Figure 1.2 illustrates the lumen-intima (LI) and media-adventitia (MA) interfaces of an US image. LD is measured as the average distance between the two LI interfaces (distal and proximal) and similarly IAD is measured as the average distance between the two MA interfaces.

Currently, the physicians measure the wall thickness and diameters of the carotid artery using manual methods. However, manual measurement is tedious, error-prone and has poor inter and intra-observer agreement (Saba *et al.*, 2012). There is increasingly growing interest among physicians for the development of automated software systems for segmentation of the CCA and measurement of wall thickness and diameters. Further, considering the development of faster hardware and better image reconstruction tools in recent years, it is now possible to accurately compute these parameters.

1.1.5 Significance of MR and US Image Denoising

The noise in medical images generally arise due to sensor imperfection, poor illumination or transmission errors. The noise present in images makes its interpretation more difficult. This necessitates the task of denoising as a pre-processing stage which may improve the performance of image segmentation techniques. It is possible to find a large number of denoising techniques in the literature including both linear and non-linear models. A good image denoising model is the one which remove noise without affecting important image features such as edges.

The carotid MR images are often corrupted by Rician noise which causes a hindrance on the carotid artery morphology (Rajan *et al.*, 2011). This affects the performance of segmentation algorithms as well as diagnostic accuracy. A simple method for denoising the images is to use local averaging. However, this can results in loss of image contrast if the shape of the filter mask is not selected appropriately. Moreover, the interface between the carotid artery and the blood may not be represented by a sharp intensity gap after smoothing. Thus, we need adaptive filters which can preserve the spatial structure of the image while smoothing it.

The noise in carotid US images is often characterized as a random granular texture called speckle. Speckle noise results from the constructive and destructive interference of ultrasound echoes made by reflectors spaced closer together than the ultrasound system's resolution limit (Milkowski *et al.*, 2009). Speckle is often modeled as a multiplicative noise under the assumption of direct proportion to the local grey level in the image (Michailovich and Tannenbaum, 2006). Considerable work has been done to reduce the speckle by incorporating different distributions such as Rayleigh distribution, Rician distribution, Gamma distribution, K-distribution and Nakagami distribution in the denoising algorithms (Hruska and Oelze, 2009; Shankar, 2000; Tao *et al.*, 2006). For automatic segmentation, it is often preferred to smooth out the speckle texture while preserving the sharp boundaries.

1.2 Motivation

Physicians perform the diagnosis of a vascular disease based on different factors such as clinical history, medical test results and medical images. However, in certain cases the diagnosis becomes quite difficult as the physician has to analyze a huge amount of data in a short time. Further, the diagnosis can be influenced by the specialization and experience of physicians. With the advances in medical imaging technology, computer softwares are increasingly being used to aid the physicians for the detection and interpretation of diseases in a short duration. These softwares provide an assessment of the disease using image-based information alone or in combination with other relevant diagnostic data and are used by clinicians as a decision support in developing their diagnoses. Further, it can be useful in the effective management of vascular diseases both in terms of early detection of diseases and as a supporting tool for the selection of patients for surgery. In order to achieve the above goals, the system output needs to be at a sufficient level of sensitivity and specificity. Moreover, the output should be in a format which can be easily understood by a clinician. In fact, developing software tools for radiological image processing is one of the challenging problems in the medical domain. Since accurate diagnosis of a disease depends on both image acquisition and interpretation, modern diagnostic systems are built by incorporating the cutting-edge computing and data processing technologies. Some of these tools require manual interventions, while some are fully automatic. Even though, computer based diagnostic systems are commercially available, fully automated approaches have not yet been completely formalized in the literature. This deficiency has led to difficulty in their use for fast diagnostic purpose.

1.3 Problem Statement

Atherosclerosis is a vascular disease which affects the size and shape of the carotid artery and is a major cause of stroke and transient ischemic attack. So far a num-

ber of studies have been investigated the predictive and preventive measures for carotid atherosclerosis based on different imaging techniques. Among this, non-invasive carotid imaging methods such as MR and US are considered to be a reliable technique to measure the carotid arterial morphology. The quantification of carotid artery stenosis via imaging techniques guides physicians to take a decision regarding surgical interventions. The method of measurement of stenosis used in the European Carotid Surgery Trial (ECST) and in the North American Symptomatic Carotid Endarterectomy Trial (NASCET) is based on the carotid artery LD measured from B-mode US (Warlow, 1991; Collaborators *et al.*, 1991). Further, there are studies which confirm the association of LD and IAD with other cardiovascular biomarkers (Polak *et al.*, 2014). It is proved that the plaque characteristics can be better analyzed from MR images and the wall thickness measured from MR images have been shown to correlate well with ultrasound IMT (Underhill *et al.*, 2006). However, the main pre-requisite for the measurement of these parameters is to locate the contours which describe the boundaries of the CCA. Manual tracing process used in this regard is time consuming and highly subjective. Computer based fully automated image analysis procedures can solve this problem.

1.4 Research Objectives

This work aims to develop automated algorithms that assist in patient risk prediction in atherosclerotic cases from MR and US images of the CCA. The important objectives of this work are:

1. To develop/improve image denoising methods for MR images.
2. To develop algorithms for automated segmentation of the CCA from MR and US images.
3. To measure and validate the carotid artery wall thickness (CAWT) of the CCA from MR images.

4. To measure and validate the lumen diameter (LD) and inter-adventitial diameter (IAD) of the CCA from US images.

5. To correlate the carotid arterial diameters with other clinical risk factors for cardiovascular risk prediction.

1.5 Major Contributions of the Thesis

This thesis contributes novel algorithms for the carotid artery wall thickness and diameter measurements from MR and US images. Further, the thesis presents a robust denoising algorithm for MR images. The major contributions are listed below:

- Developed an improved denoising algorithm (NLML$_{DCT}$) for denoising MR images. This was an improved version of the conventional NLML approach.
- Proposed a novel strategy for the segmentation of lumen and outer wall contours of the carotid artery from T1-weighted MR images and measured the carotid artery wall thickness.
- A fully automated region-based method is developed for the segmentation of the CCA from B-mode US images and measured the lumen and inter-adventitial diameters.
- The measurement accuracy is further improved by using a spatial transformation based iterative approach for handling curved vessels.
- The clinical significance and implications of arterial diameters were studied.

1.6 Organization of the Thesis

The remaining part of the thesis are organized as follows: Chapter 2 presents a brief literature review of the carotid artery segmentation techniques in both MR and US images while providing a general framework for segmentation. The theoretical background of different techniques are furthermore explained.

Chapter 3 introduces a robust denoising technique for MR images based on non-local maximum likelihood (NLML) paradigm in discrete cosine transform (DCT) framework. This is an improved version of the conventional NLML in which the intensity similarity of the pixel neighborhoods has been computed in the DCT subspace. Furthermore, a semi-automatic method for carotid artery wall segmentation in MR image has been proposed and experimentally validated.

Chapter 4 starts with a discussion in regard to the issue of speckle in carotid ultrasound images. The main focus of the chapter is to develop an accurate carotid lumen segmentation system for US images. A fully automated region-based approach is proposed which combines the scale-space strategy with pixel-classification. This approach is further improved using a spatial transformation for handling curved vessels.

The relationship of carotid arterial diameters and other clinical risk factors is studied in Chapter 5 along with clinical significance and implications of LD/IAD and wall thickness. A comparison with other similar studies is attempted wherever possible.

In the last chapter, Chapter 6, we provide a brief discussion on the findings of this work along with the concluding remarks and future work suggestions.

CHAPTER 2

CAROTID ARTERY SEGMENTATION APPROACHES

In this chapter, we present the theoretical background of the carotid artery segmentation methods using MR and US images. Section 2.1 briefly discuss the practice of MR and US imaging of carotid artery in a clinical environment. Then in Section 2.2, a literature review of the carotid lumen and outer wall segmentation from MR images is presented. Section 2.3 explores the carotid artery segmentation and LD/IAD measurement techniques in US images along with a general framework for segmentation. A few important evaluation metrics are discussed for evaluating the segmentation methods.

2.1 MR and US for Carotid Artery Imaging

MR and US imaging have their own specific strengths and weaknesses, understanding the uses of each modality appropriately can result in a much better, more accurate diagnosis. In clinical practice, US imaging combined with MRI of the carotid arteries is valuable in diagnostic work-up to demonstrate the presence, location and extent of carotid narrowing. However, it appears premature for routine application of MRI as an imaging modality to assess the carotid plaque characteristics associated with plaque vulnerability. Although MRI still holds promise, clinical application for plaque characterization would require consensus regarding MRI settings and confirmation through histology. The general inclusion criteria for performing MRI of the carotid arteries are the following: presence of an ultrasound analysis that showed a carotid stenosis $\geq 50\%$ and evidence of plaque alteration (an irregular surface, intra-plaque hemorrhage, ulceration). Overall, no optimal single or combined imaging work-up for carotid stenosis has

been defined yet. Due to this reason, we focus on developing automatic carotid artery segmentation strategies for both MR and US imaging modalities.

2.2 Segmentation from MR Images

The degree of carotid atherosclerosis can be determined by evaluating the artery wall quantitatively. This in turn requires the segmentation of contours which describes the boundaries of the CCA (Liu *et al.*, 2006). The ability to offer high resolution images and non-invasiveness makes the MRI an ideal tool for analyzing the carotid artery (Kramer and Anderson, 2007). MRI has the ability to detect the boundaries of the carotid artery from transverse images and can assist in plaque characterization (Yuan *et al.*, 2008). Moreover, MRI offers reduced measurement variability when compared to US images.

The accuracy of the carotid artery wall thickness (CAWT) measured via automated techniques should be high enough to meet the clinical standards. Some of the challenges in the automatic segmentation of the carotid artery include contrast variations, image artifacts, and presence of noise in MR images. Further, these images are usually characterized by their weak edges which allow a continuous flow of image information from one region to the other. The signal intensity of some of the tissues surrounding the outer wall boundary is similar to that of the wall. This problem of weak-edge-leakage has been reported by many authors (Saba *et al.*, 2014*a*; van't Klooster *et al.*, 2012; Yuan *et al.*, 1999). Furthermore, there are structures, such as the jugular vein (JV), in the area surrounding the carotid artery that produces additional edges. This makes it hard to segment the images into distinctive regions.

Figure 2.1 shows a general flow diagram for the carotid artery segmentation from MR images. One important pre-processing step is the removal of Rician noise from MR images and thereby increases the signal to noise ratio (SNR). The segmentation usually carried out in sequential steps in which the estimation of the inner lumen borders followed by outer wall borders. These borders finally evaluated against the manual

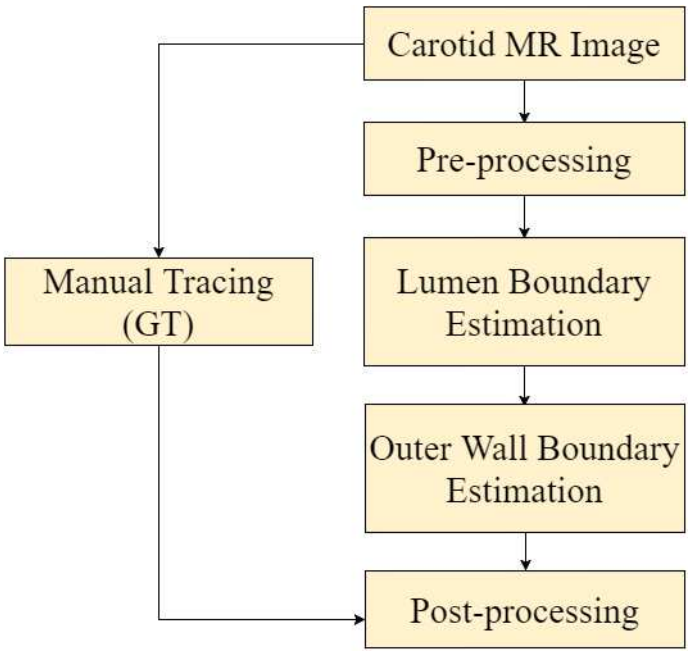

Figure 2.1: General flow diagram showing segmentation of the carotid MR images.

tracings by experts which are considered as ground truth (GT).

Many methods have been proposed in the literature for the segmentation of the carotid artery wall in MR images. This includes both automatic and semi-automatic techniques. Yuan *et al.* (1999) developed an automated edge detection algorithm to identify the inner and outer wall boundaries of the carotid artery in proton density weighted (PD-w) MR images. They have used a Snake model based algorithm to identify the contours for which the initial Snake points needs to be identified by the user manually. Ladak *et al.* (2001) presented a semi-automatic method based on discrete dynamic contour (DDC) for segmenting the carotid artery wall from black blood MR images (BBMRI). The DDC deforms to conform to the shape of the arterial wall. However, detection of the outer boundary was generally poor for moderate to thick plaques. The above two methods (Yuan *et al.*, 1999; Ladak *et al.*, 2001) have limitations if the carotid artery has high degree of stenosis and uneven lumen boundaries. Further, the algorithm is sensitive to various contrast situations.

MR imaging has the ability to offer high resolution cross sectional images of the

carotid artery which can be used for characterizing the atherosclerotic plaques. An automated contour detection technique (Adame *et al.*, 2004) was proposed for delineation of the contours of the carotid artery in short-axis BBMRI (both PD-w and T1-w). This approach combined model-based segmentation (ellipse fitting) with fuzzy clustering. Fuzzy clustering was used to separate three different classes of tissues corresponding to the lumen, plaque and the wall. This method achieved significant improvement over previously published techniques. The main difference is that it deals with in vivo MR images and has been validated on carotid arteries with different degrees of stenosis. However, the hypothesis of elliptic shape is an oversimplification when severe stenosis is present. Further, there was no attempt to measure the artery wall thickness.

Underhill *et al.* (2006) proposed a semi-automatic technique to measure the mean wall thickness (MWT) of the CCA from T1-w MR images using active shape model (ASM). A user identifies a point within the lumen of the CCA via graphical user interface from which the lumen boundary is roughly estimated using a region growing technique. Then, ASM is employed to delineate the exact lumen as well as the outer wall borders. In each step of the algorithm, the fitness is evaluated by combining local edge information and area. The mean distance between the inner and outer contours is calculated at each slice level. Then, MWT is determined by the mean of all the individual thickness measurements from each axial location. In their study, the MWT is found to be highly correlated with the IMT measured from B-mode US. This strongly indicates that it is possible to use carotid MRI as a tool for assessing systemic atherosclerotic disease. However, one drawback with ASM is that if the training set is small, the performance can be limited due to variations in the data.

Arias *et al.* (2012) presented a three-dimensional (3D) coupled surface graph cut algorithm for the segmentation of both the inner and outer vessel wall borders form carotid MR images. The lumen centerlines were determined using the user defined seed points. The method combined the search for both inner and outer vessel wall borders into a single graph cut and used two different cost functions. An initial affine

registration was performed on the data (PD-w BBMRI and PD-w Echo Planar MRI (EPIMRI)) using mutual information. The authors found that the EPIMRI images have better wall contrast, which generates better results in some images compared to the results obtained by BBMRI. A major disadvantage of this method is that the output very much depends on the initially segmented lumen shape. Registration errors of the EPIMRI images are another concern.

A semi-automatic segmentation method was developed by van't Klooster *et al.* (2012) using deformable three-dimensional (3D) tube models. This method used combination of two different types of images (3D MR angiography (MRA) and 2D MR images) which can possibly decrease the manual interaction and at the same time improving the segmentation performance. This was the first 3D model developed which was applicable to both isotropic and non-isotropic image data. A Time of Flight MRA image is used to identify the artery of interest. However, the availability of the 3D MRA data is limited and in the absence of 3D MRA, the user interaction become little more complex because the artery of interest has to be indicated in the vessel wall slices.

Ukwatta *et al.* (2013) proposed a robust 3D segmentation algorithm for delineating the carotid artery walls in T1-w BBMR images. This is a global optimization based approach which allows the simultaneous evolution of contours corresponding to the lumen and vessel walls. The algorithm achieves high accuracy and precision with fewer user interactions (choosing sampled voxels of the carotid wall, lumen, and background region on a single transverse slice). However, the authors reported some disagreements with the manual segmentations due to inadequate user interaction and quantization errors in the volume computation.

Saba *et al.* (2014*a*) developed a semi-automatic technique for CAWT measurement in PD-w MR images. Level set method (LSM) was employed to segment both the lumen and outer wall boundaries. The procedure of LSM segmentation was done on a slice-by-slice basis. A user needs to initialize the curve evolution by marking a point inside the lumen which will stop at the luminal boundary. The segmented lumen boundary grows

outward by two pixels for the initialization of outer wall boundary segmentation. Then the curve evolution takes place as in the previous step. However, due to poorer contrast between outer wall and surrounding tissues, this usually takes more number of iterations than for luminal boundary. Even though the method achieved high accuracy on the specified dataset, the authors reported some challenges which need to be addressed. These include the leaking problem in LSM due to blurred edges and heterogeneous intensity in the arterial wall. This may cause the LSM to get trapped at some other locations rather than at the real outer wall.

Arias-Lorza *et al.* (2016) presented an improved 3D graph-cut segmentation algorithm which was designed for multi-spectral carotid artery bifurcation MR images. This method was an extension of the previously published work (Arias *et al.*, 2012) with improved graph edge cost function. In this approach, the lumen centerline extraction had been automated. However, manual intervention is still required for the initialization to build the graph.

2.3 Segmentation from US Images

The US imaging techniques currently in practice for the diagnosis of the carotid artery are B-mode US and Doppler US. B-mode ultrasound imaging aids in the visualization and measurement of the carotid arterial morphology (Sanches *et al.*, 2011). The Doppler US imaging is another standard clinical tool for the assessment of hemodynamics of the carotid artery (Sarkar *et al.*, 2007). Color Doppler US provides information regarding blood flow in the lumen, which enables the clinician to detect flow reduction, flow turbulence and occlusion in arteries (Branas *et al.*, 1994). However, Doppler ultrasound have limitations in giving a clear picture of the carotid stenosis since the blood velocity is not constant (Mehra, 2010). Moreover, the Doppler spectrum is likely to get distorted (Doppler mismatch) by an acoustic impedance mismatch between the fluid and the vessel walls (Jones *et al.*, 1996). This mismatch is more prevalent in case of patients

with hypo tension or hypertension, tortuous vessels, presence of hypoechoic or calcified plaques and pre-occlusive lesions (Carroll, 1991). Since the B-mode US imaging capture the morphology of plaque build-up based on the sound reflection and not based on the blood velocity, it has a better chance of determining the severity of atherosclerosis. In this section, we discuss the carotid artery segmentation from B-mode US images and the measurement of arterial diameters (LD and IAD).

The LD and IAD of the CCA measured from B-mode US images can be considered as a surrogate marker for risk of CVDs. B-mode US allows for easy visualization and quantification of anatomical structures and the images can be acquired in real time, thus providing instantaneous visual guidance for many interventional procedures. Figure 2.2 illustrates the "Meijer Arc", the standardized approach for B-mode carotid US scanning (Stein *et al.*, 2008). An increase in the IAD or decrease in the LD has been correlated with the incident of stroke events (Polak, 2004). The CCA diameter has shown to be correlated to cardiac events (Eigenbrodt *et al.*, 2007), age (Eigenbrodt *et al.*, 2006), and other conventional vascular risk factors like gender, smoking history, hyperlipidemia, and hypertension (Polak *et al.*, 1996; Jensen-Urstad *et al.*, 1999). Further, the carotid IAD is independently associated with first-time incident ischemic stroke, left ventricular mass and IMT (Polak *et al.*, 2014). Moreover, the plaque formation in the carotid artery is an early indicator for coronary artery disease and myocardial infarction (MI) (Mughal *et al.*, 2011). The asymptomatic carotid artery stenosis can be quantified by measuring the changes in the LD/IAD over time, and can be used as a secondary validated measure to decide whether carotid endarterectomy/stenting is required or not (Fayad, 2007). The ability to provide reliable, accurate and highly reproducible measurements makes LD/IAD an attractive imaging biomarker.

A large number of follow-up studies have used high-resolution B-mode ultrasonography to investigate the determinants of atherosclerotic disease, because of its ability to identify atherosclerotic lesions at all stages of development (Constantinescu *et al.*, 2012). Usually, delineations of the CCA are performed manually by medical experts

Figure 2.2: Meijer Carotid Arc: illustrates the standardized approach for carotid ultrasound scanning which will give a set of reproducible images. Reprinted from (Stein *et al.*, 2008), with permission from Elsevier.

using calipers (Nicolaides *et al.*, 2011), but it was shown that this process is tedious, prone to errors, and has large observer variability (Saba *et al.*, 2012). Further, the real time imaging of the carotid artery is now possible due to the availability of better image reconstruction tools in US imaging (e.g. compound and harmonic imaging) (Nicolaides *et al.*, 2011; de Korte *et al.*, 2011). However, automated methods are required for the accurate and reliable delineation of the CCA from US images.

2.3.1 General Framework for Carotid Artery Segmentation

Accurate knowledge and understanding of the geometry of the carotid arteries is important in their segmentation. Several automated algorithms have been proposed for segmentation of the carotid lumen, but majority of them are focused on the segmentation and measurement of IMT. However, a few authors have pointed out the need for automated measurement of the carotid LD (Polak *et al.*, 2014; Jensen-Urstad *et al.*, 1999; Godia *et al.*, 2007). The lumen segmentation algorithms can be broadly classified into two different categories as: region-based (Sifakis and Golemati, 2014; Rocha *et al.*, 2014; Cinthio *et al.*, 2010) and boundary-based (Santos *et al.*, 2013; Golemati *et al.*, 2007; Loizou *et al.*, 2013; Molinari *et al.*, 2010*b*; Rocha *et al.*, 2011, 2012). The class of segmentation algorithms in image processing are based on two properties, similarity and discontinuity. The region-based model works by assuming same intensity or similarity throughout a specific region. Hence, it generally assumes same lumen intensity which follows from the constant blood density assumption (Prosi *et al.*, 2007). Since no gradient information is used in the process, the segmentation will be robust to cases having discontinuity in the boundaries of the carotid artery. Unlike region-based methods, boundary-based approaches generally follow parametric curves (traditional snakes) or geometric curves (level set) with a manual initialization. Moreover, since boundary-based approaches rely on intensity gradients (intensity discontinuity), they are often susceptible to false edges and discontinuities in the lumen borders. Figure 2.3 shows general flow diagram of region-based and boundary-based lumen segmentation.

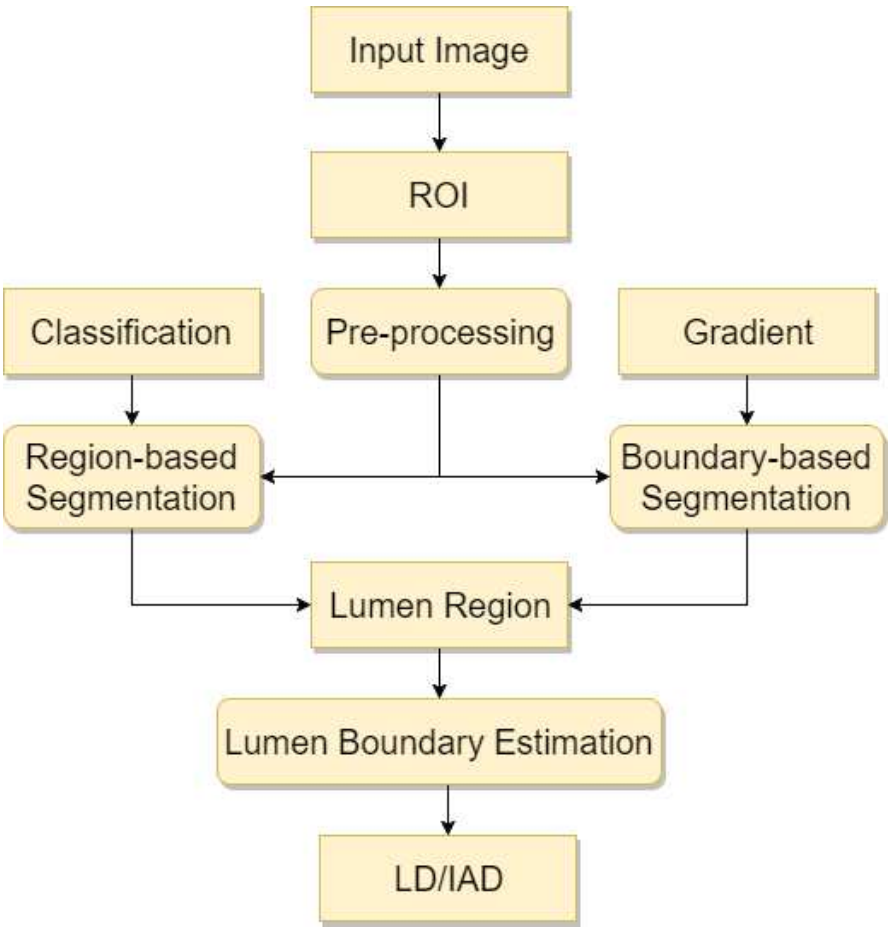

Figure 2.3: General flow diagram showing the region-based and boundary-based lumen segmentation in B-mode US images.

Each block in this flow diagram is explained below in detail.

ROI Selection

The first stage in the carotid artery segmentation is the recognition of the region of interest (ROI). Commonly, the region between the outer wall layers (near adventitia layer and the far adventitia layer) is taken as the ROI. This provides many advantages while tracing the LI interfaces. First of all, the CCA can be easily confounded with the JV because of their very similar echo-graphic appearance. Then, while considering the morphological aspect of the CCA, the artery can be of different shape and straight or curved. However, once we select the ROI, we have only limited area to search for the

LI interfaces. Speckle noise in ultrasound images often limits the performance of the classification/edge detection techniques. Since the lumen region can be considered as the dark region that is located between the two bright adventitia layers of the CCA, this might be the best approximation for the ROI.

Golemati *et al.* (2007) presented an algorithm that defined four specific points to describe the ROI. The morphological opening followed by a suitable thresholding generates a binary image. Then the four control points were defined based on the first and last non-zero pixels along the raw and column. Santos *et al.* (2013) reproduced the same idea proposed in Golemati *et al.* (2007) in their study for the ROI selection. However, this algorithm has limitations in the less bright images where a portion of the lumen region may get cut off in the process. Rocha *et al.* (2011) have chosen the ROI as the smallest rectangular box containing all pixels within a particular distance from the user defined lumen axis. This distance is estimated based on the lumen width of the largest carotid artery image found in the dataset. Hence, the method described in (Rocha *et al.*, 2011) is a semi-automatic method. In another automatic approach (Rocha *et al.*, 2012), classical Otsu's algorithm was used to compute two different thresholds, $T1$ and $T2$, and a binary image is generated which contains only the objects having intensity in between $T1$ and $T2$. After removing smaller objects using morphological opening, ROI is then defined as the smallest rectangle that encloses the remaining objects. They further refined this ROI and generated ROI-2, using an estimate of the lumen axis. Sifakis and Golemati (2014) used an approach that divides the distributions of the local mean and variance of vertical intensities using percentiles, and then used user-defined percentile-based thresholds to recognize the potential ROIs.

Pre-processing

Once we compute the ROI, the next step is to do some pre-processing such as contrast enhancement and noise removal. This stage helps in improving the quality of image in ways that increase the accuracy of segmentation. Some authors have performed a

Gaussian smoothing (Rocha *et al.,* 2014; Golemati *et al.*, 2007; Molinari *et al.*, 2010*b*) or speckle filtering (Santos *et al.*, 2013; Loizou *et al.*, 2013) of ROI. This is to reduce the noise in the image and thereby easing the process of LI interface delineation. In Santos *et al.* (2013), the image is processed with the application of an anisotropic diffusion filter for speckle removal prior to segmentation. Similarly in Loizou *et al.* (2013), the authors have used a linear scaling filter to remove multiplicative noise prior to the segmentation. A non-linear smoothing filter was conceived in Rocha *et al.* (2011) and applied to the ROI to reduce the noise before computing the edge map.

In Gaussian filters, the amount of smoothing is usually controlled by the standard deviation (σ), which must be large enough to reduce the noise. However, if it is too large, the CCA walls may get completely blurred. The carotid lumen images of CVD patients usually contain protruding hypoechogenic plaques. Further, the low contrast of the LI interfaces is another reason why we need to select an optimal value for σ. Morphological closing was performed as a pre-processing step in Golemati *et al.* (2007) to merge small ”channels” and ”openings” of the image. Here, the shape and size of the structuring element is selected such that it does not alter the anatomical information contained in the image.

In most of the studies, ROI selection has been done prior to the pre-processing stage. This is to increase the effectiveness of the pre-processing algorithm and to avoid any negative affect that may occur. For example, denosing algorithms can be greatly affected by the background information. Segmentation is the next step after pre-processing. The existing segmentation algorithms can be broadly classified into two: region-based and boundary-based. The segmentation techniques coming under these two categories are discussed below and their merits/demerits are compared in detail.

Region-based Segmentation

The region-based model works based on the distribution of image intensities and hence able to capture the lumen intensities under the constant blood density assumption (Prosi *et al.*, 2007). There exist only a few region-based methods in the literature which are summarized in Table 2.1 along with their limitations. These limitations are an indication of future research perspectives. A sub-pixel resolution method was suggested by Cinthio *et al.* (2010) for carotid LD measurement which utilizes relative threshold detection on the arterial walls. The gray-scale information was averaged laterally within a pre-defined ROI to produce an envelope profile. Then, the vessel wall edges were found out by applying a suitable threshold which was determined based on the maximum intensity points in the profile. The process is repeated again after increasing the image resolution to get the refined positions of the walls. Even though this method reduces the computational load by giving a more robust estimate for sub-optimal images, a major problem is regarding with the accuracy which results in underestimation of the LD. Further, the method assumes horizontal orientation for the carotid artery, and does not take care of tortuous or tilted arteries.

Sifakis and Golemati (2014) made an attempt to find the carotid lumen center point based on the distributions of the local mean and variance of intensities. This method used user-defined percentile-based thresholds to recognize the ROIs. Further, they assumed that the majority of the lumen center points will be located in a similar depth within the ultrasound image. This algorithm effectively localizes the carotid artery with relatively low computational cost. However, this method has several limitations. Relatively low performance was observed in certain cases which includes presence of carotid artery mimicking structures, poor far wall representation, an abruptly curved arterial shape and non-uniform luminal intensity. Moreover, there was no discussion about the quantification of LD or IAD.

Rocha *et al.* (2014) used a linear Bayes classifier to classify the longitudinal paths in the process of finding the carotid lumen axis. They have defined two classes; the

class of blood vessels and the class of other anatomical structures, assuming normal distributions for both the classes. The algorithm initially scans from the first to the last column of the ROI, looking for all the paths that produce local minima based on the pixel intensity. The Euclidean distance to the local minima is then used as a cost map and input to the dynamic programming (DP) algorithm. DP is used to determine the longitudinal paths which are possible estimates of the lumen axis. The authors claimed that the method is not misguided by the JV above the CCA or vessel-like structures below the CCA. However, this method did not consider the near wall due to poor visibility and hence difficult to adapt for the carotid LD estimation.

Table 2.1: Overview of region-based techniques proposed in the literature

#	Author (Year)	Approach	# Subjects	# Images	LD/IAD Measurment	Limitations
1	Cinthio *et al.* (2010)	Sub-pixel resolution method	3	30	LD: Yes IAD: No	i. Under estimation of LD ii. Does not take care of tortuous or tilted arteries
2	Sifakis and Golemati (2014)	Combination of anatomical knowledge and statistic	100	2149	No	Relatively low performance in following cases: i. Presence of carotid artery mimicking structure ii. Poor far wall visibility iii. An abruptly curved arterial shape iv. non-uniform luminal intensity
3	Rocha *et al.* (2014)	Gaussian filtering and dynamic programming	25	199	No	i. The near wall was not considered due to poor visibility ii. Fails in images with strong noise inside the CCA lumen region

Boundary-based Segmentation

The boundary-based approach for lumen segmentation originates from the idea that the edge-model can be adapted for tracking the carotid wall borders. These borders represent discontinuities in brightness or pixel intensity. One simple approach for these interface detection is to use an edge detection technique. However, the boundaries identified are often disconnected and one needs to find closed region boundaries for successful segmentation. Hence, some pre-processing techniques often apply prior to the segmentation in order to enhance the edges. Many methods were proposed in the literature for the detection of edges corresponding to the LI and MA interfaces. State of the art methods in the literature for boundary-based segmentation include Hough's transform (HT), active contours and deformable templates and level-set based methods. Table 2.2 gives an overview of boundary-based (edge-based) techniques proposed in the literature.

Hough's transform (HT) was used for the automated carotid lumen segmentation by Golemati *et al.* (2007). Their assumption of straight lines (in longitudinal images) and circles (in transverse images) for carotid lumen received much attention among the research community. The algorithm was tested on image sequences, rather than static images. This allowed the assessment of changes of arterial wall geometry during the cardiac cycle and subsequent changes in arterial diameters. Due to changes in the shape and orientation of the carotid arteries, during the acquisition protocol, it puts a challenge on the above assumptions in case of diseased carotid arteries. As a result, the arterial boundary departs from a simple geometrical shape. Therefore, the authors suggested the use of active contours in combination with the HT for diseased arteries.

Molinari *et al.* (2010*b*) used an integrated approach in order to extract the carotid artery layer which consists of geometric feature extraction, line fitting, and classification. The output of the algorithm was the tracings of the proximal and distal adventitia layers. The authors have tested their algorithm extensively on a database consisting of 200 randomly selected longitudinal B-mode ultrasound images of the CCA. How-

ever, the authors have spotted two particular conditions that caused imperfect adventitial tracings. These include ”multi layered” images and images having deeper plaques protruding into the artery lumen. Here the ”multi layered” image means nothing but images having a repeated pattern of lumen walls due to the presence of other similar structures such as JV. Under these conditions, the algorithm successfully traces line segments corresponding to the far CCA wall, near CCA wall, and near JV wall. However, the algorithm fails in the final identification of correct line pairs for LI borders.

A semi-automatic technique was proposed by Rocha *et al.* (2011) using random sample consensus (RANSAC) method for the segmentation of far and near adventitia boundaries of the CCA. At first, the edges inside the ROI were detected using a non-linear image filter, non-maximum suppression and hysteresis. The segmentation of the adventitia boundary was based on a RANSAC search of the best fit of a given contour model (which is evaluated according to a gain function). The authors have mentioned about mis-detections of the carotid adventitia in the presence of similar boundaries such as JV boundaries. Another drawback discussed is the influence of a thick plaque on the gain function. In this case, the plaque region pushes the lumen boundary away from the adventitia boundary resulting in an under estimation of the gain function. This causes an increase in the number of samples analyzed by the RANSAC algorithm and in turn increases the cost of computation.

A fuzzy classification-based approach was proposed by Rocha *et al.* (2012) for the automated segmentation of carotid arteries followed by computation of the lumen axis. Using fuzzy edge detection, all step and valley edges in the ROI were determined and classified by extracting various features of the carotid wall interfaces. By adopting a fuzzy classifier, the authors have avoided the use of low pass filtering which might eliminate important weak edges. The major advantage of this method is that both the near and far wall boundaries were detected which is a pre-requisite for the LD/IAD computation, but the authors did not attempt.

The segmentation of carotid lumen region has been carried out by Santos *et al.*

(2013) by utilizing the hypoechogenic characteristics of the lumen. The algorithm initially employ morphologic operators for the detection of the carotid artery. Then the lumen and bifurcation contours are segmented using the Chan-vese (CV) level set segmentation model. However, threshold-based region detection is seldom susceptible to false region estimation if the images are noisy due to low resolution or hyperechoic characteristics or shadows due to the presence of calcium in the near wall. Further, the morphological processing operations are sensitive to noise and hence are not very stable (Sigmund, 2007).

Loizou *et al.* (2013) introduced a Snake-based segmentation technique for the carotid bifurcation and diameter estimation. In addition to this, they successfully segmented the atherosclerotic plaques as well. However, the initialization of Snakes remains a challenge. This is because since the propagation force is frequently based on intensity gradients, it makes the Snake vulnerable to false edges. Moreover, the Snakes usually leak through the discontinuities in the wall borders where the gradient is too weak (Molinari *et al.*, 2012*c*).

Table 2.2: Overview of boundary-based techniques proposed in the literature

#	Author (Year)	Approach	# Subjects	# Images	LD/IAD Measurment	Limitations
1	Golemati *et al.* (2007)	Hough Transform	10	image sequence of length 70-80	LD: Yes IAD: No	Fails in cases: i.the arterial boundary has a random shape or curvature ii. Presence of speckle noise iii. Presence of thick plaque
2	Molinari *et al.* (2010*b*)	Integrated approach consisting of geometric feature extraction, line fitting and classification	130	200	No	i. Non-perfect tracing of boundaries in case of noisy lumen and overlap of the Jugular Vein (JV)
3	Rocha *et al.* (2011)	RANSAC and cubic splines	25	50	No	i. The amount of smoothing must be controlled ii. Misdetections of the carotid adventitia occur in presence of other similar structures
4	Rocha *et al.* (2012)	Fuzzy classification	25	50	No	i. Misdetections occur in presence of similar boundaries
5	Santos *et al.* (2013)	Chan-Vese level set segmentation model	-	11	No	i. Fails if carotid artery image is of low contrast and noisy ii. Tested on a small database
6	Loizou *et al.* (2013)	Snake based segmentation	20	20	LD: Yes IAD: No	i. Faces challenge of initialization of snakes ii. Only a small number of subjects included

Even though, more boundary-based approaches are reported than region-based in the literature, it can be concluded that the region-based strategy is giving more satisfactory results when comparing the overall performance. This can be justified by considering the dependency of boundary-based algorithms on edges or image gradients. One explanation is that boundary-based methods are more sensitive to changes in the gradient information at the wall borders during the cardiac cycle. The rapid changes in the velocity of blood flow in the artery causes subtle changes in the shape and size of the lumen (Chow *et al.*, 2008). Since the image acquisition takes place during the cardiac cycle, it is often sensitive to these changes when the image frame gets frozen. One way to compensate for this sensitivity is to consider the neighboring frames. The second explanation for higher error is associated with the multi-focal nature of atherosclerotic plaques. The random deposit of plaques along the carotid artery subsequently affects the intensity distribution and thickness of the diseased arterial wall. Further, boundary-based techniques are sensitive to sudden changes in the variations of the gray scale intensity distribution along the CCA, and will therefore yield less optimal results. This can be compensated by taking regional statistics embedded with boundary-based information.

2.3.2 Challenges during Segmentation

CCA segmentation is a challenging process, whereas developing a fully automated system is even harder in practice. One should take advantage of the knowledge in ultrasound image reconstruction in the segmentation process. The images may have scanned with different hardware settings (frequency, depth, gain, etc.) and different positioning of the probe. The challenges for segmentation vary with the quality of image data and the view due to the anisotropy of US image acquisition. The presence of different anatomic structures such as the JV and other muscles which are floating around in the ultrasound image may lead to erroneous capture of the carotid walls (Molinari *et al.*, 2010*a*, 2011).

There are several challenges for the automated carotid lumen segmentation from US images. These are primarily due to the variability in data sets. The shape and size of the carotid artery, presence of plaque and curvature in arteries make the segmentation process harder (Nicolaides *et al.*, 2011; de Korte *et al.*, 2011; Sanches *et al.*, 2011; Saba *et al.*, 2014*b*). Since there is variation in the image contrast due to variation in composition, stage and grade of the deposited plaque at the lumen-wall interface (Suri *et al.*, 2005), threshold-based systems often fail in segmenting the artery. Characteristic artifacts, such as attenuation, speckle noise, acoustic shadowing and signal dropout may complicate the segmentation task (Golemati *et al.*, 2007; Sanches *et al.*, 2011). Figure 2.4 illustrates the variation of the carotid artery images across different patients.

In an US image, attenuation is the reduction in amplitude of the ultrasound beam as a function of distance through the imaging medium. Accounting for the attenuation effects in ultrasound is important because reduced signal amplitude can affect the quality of the image produced (Bushong, 1999). Acoustic shadowing in an ultrasound image is characterized by a signal void behind structures that strongly absorb or reflect ultrasonic waves (Whittaker, 2007). This happens most frequently with solid structures, as sound conducts most rapidly in areas where molecules are closely packed, such as in bone or stones. The direct effect of acoustic shadowing or echo attenuations in the segmentation task is that some boundaries or boundary segments may be missing which may lead to edge leaking at the near and far LI interfaces.

Sensitivity to ultrasound vibrations at each depth of the body is different due to which the imaging suffer from signal loss from deeper in the tissue. Signal drop-out may occur frequently while imaging arteries with 65-70% stenosis, especially if the CCA is deposited with high amount of calcium (Slovut *et al.*, 2010). This makes it difficult to determine the boundaries of the true lumen. Further, the presence of multiplicative speckle noise in carotid ultrasound images tends to reduce the image resolution and contrast thereby degrading the image quality. US images are often considered as the hardest to segment among medical images due to their low SNR (Dahl *et al.*,

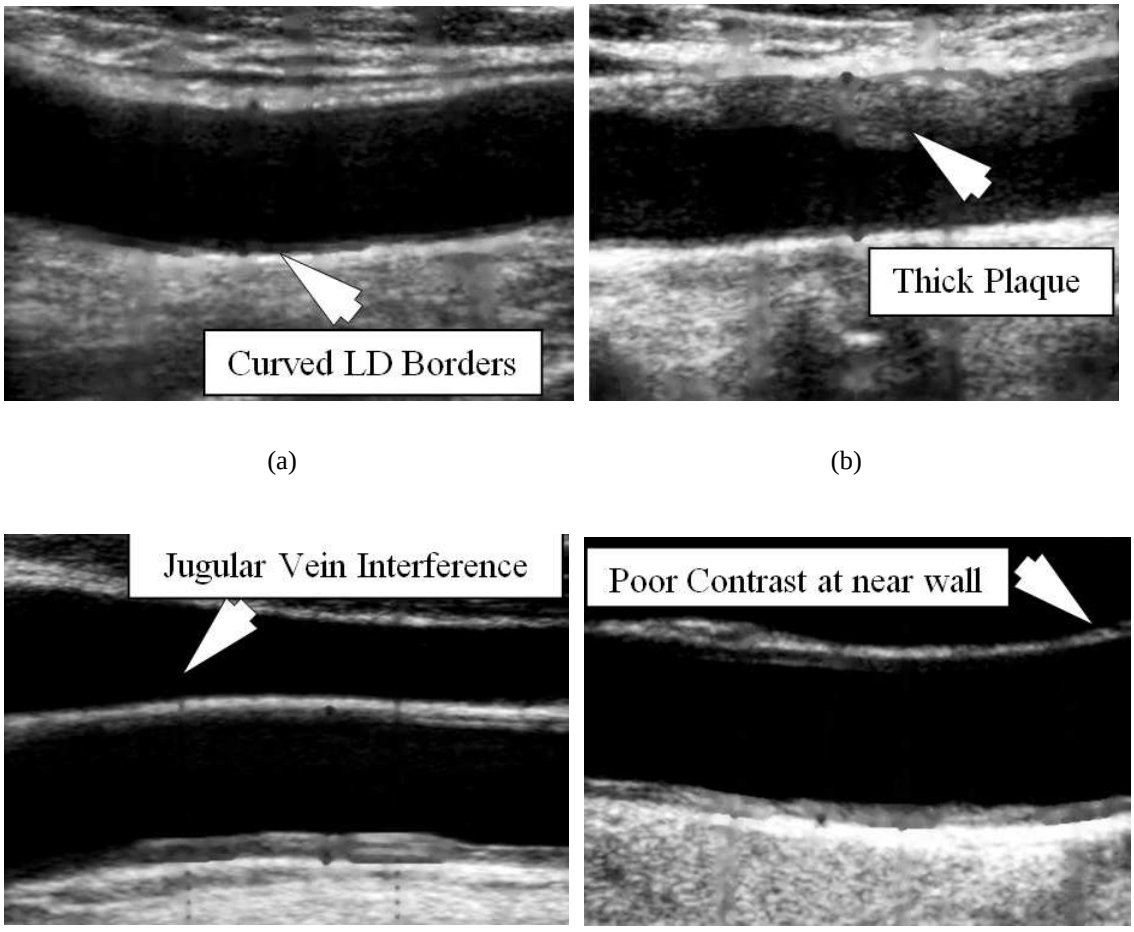

Figure 2.4: Illustrating the variation of carotid artery images across different patients. (a) Curved lumen diameter (LD) borders; (b) High plaque deposit and narrowing of carotid artery; (c) Low contrast image with jugular vein interference. (d) Image having poor contrast difference at near wall.

2011). There are many methods available for speckle noise reduction in the literature (Michailovich and Tannenbaum, 2006; Zhang *et al.*, 2015; Tay *et al.*, 2010).

There are certain characteristics that make an US image suitable for the automated delineation of the carotid artery borders. These include high spatial resolution, high dynamic range, low noise level, compound and harmonic imaging (Molinari *et al.*, 2012*e*). Specific image enhancement or denoising strategies may need to be adopted, if the image does not possess these characteristics. The compound and harmonic imaging facilities are available on most of the medium-level and high-level US OEM (Original Equipment Manufacturer) scanners, whereas they are not present in majority of the entry-level or cheaper equipments. This results in a poor quality image with low contrast at the near and far LI interfaces leading to inaccurate segmentation.

The important factor that complicates automatic detection of the CCA is the presence of JV structure which is often seen just above the CCA (see Figure 2.4). Since the echographic appearance of the CCA and JV are very much similar, the near wall of the CCA can easily be confounded with the far boundary of the JV. Deeper plaques protruding into the carotid artery lumen represents another cause of imperfect segmentation. The plaque substantially perturbs the average intensity level of the CCA lumen. Usually, in patients with severe stenosis ($> 80\%$), hypoechoic plaques appear at both the walls (Polak *et al.*, 1998). This not only causes non-uniform luminal intensity, but also results in an abruptly curved arterial shape (e.g. due to a relatively large plaque). Therefore, the final boundary segmentation may have many deficiencies. It can be observed that some of these challenges are inter-related. For example, in presence of increased speckle content in US image, the segmentation algorithm may not be able to distinguish between the carotid lumen and the hypoechoic plaque tissue. A major limitation of the algorithms developed so far is that they do not take care of tortuous or tilted arteries, i.e., the lateral averaging cause an underestimation of the true lumen diameter if the artery is not horizontally scanned. The segmentation method proposed in this thesis uses a spatial transformation approach to address this issue.

2.3.3 Validation Metrics

An automated carotid artery segmentation system can be evaluated in two ways. One is by simple visual inspection of fine details which is only possible by expert physicians. The second way is to analyze the system quantitatively using some metric and compare the automated measurement against the manual expert tracings, which are considered as GT. Further, it is mandatory for an automated medical system to compare and validate against manual tracings in order to be accepted in the clinical domain. Different evaluation metrics are used for evaluating the performance of carotid artery segmentation algorithms. The following are some of the popular performance metrics found in the literature.

i. Coefficient of Correlation (r)

The linear correlation coefficient (r) (Swinscow *et al.*, 2002) measures the strength and direction of a linear relationship between two variables (auto and manual measurements). This is sometimes referred to as the Pearson correlation coefficient. The mathematical formula for computing r is (Swinscow *et al.*, 2002):

$$r = \frac{n\sum xy - \sum x \sum y}{\sqrt{n\sum x^2 - (\sum x)^2}\sqrt{n\sum y^2 - (\sum y)^2}} \tag{2.1}$$

where n is the number of pairs of data, x and y are the variables of interest. The value of r is such that $-1 < r < +1$. The $+$ and $-$ signs are used for positive and negative linear correlations, respectively. The standard method used to measure the 'significance' of this correlation analyses is the p-value. Typically, values of either 0.01 or 0.05 are taken as cutoff.

ii. Coefficient of variation (CV)

The coefficient of variation (CV) can be calculated according to the formula (Liang *et al.*, 2000):

$$CV = \frac{S * 100}{x} \tag{2.2}$$

where

$$S = \frac{SD}{\sqrt{2}} \tag{2.3}$$

x is the pooled mean and SD is the standard deviation for the difference between automated and manual measurements of LD.

iii. Mean Absolute Distance (MAD)

Mean Absolute Distance (MAD) is used as a boundary distance-based metric. The averages of MAD can be computed using all vessels in the database images to obtain an overall estimate of boundary disagreement. The formula to compute MAD is given by (Liang *et al.*, 2000):

$$MAD_{M,T} = \frac{1}{K} \sum_{i=1}^{K} |d(m_i, a_i)| \tag{2.4}$$

where $d(m_i, a_i)$ is the distance between the boundary point m_i of the manual drawn contour and its corresponding boundary point on automated contour a_i and K is the number of points included in the two boundaries (manual and automated). In the case where the two boundaries do not have the same number of points, then one of them can be interpolated. However, if the boundaries include curved segments, then MAD will be overestimated.

iv. Precision of Merit (PoM)

Precision of Merit (PoM) is a key feature used to validate the automatically traced carotid diameter against the manually traced one. There are two different ways for computing the PoM. The overall systems performance was computed using the first method of precision-of-merit ($PoM1$) in percentage as (Ikeda *et al.*, 2015):

$$PoM1_{LD}(\%) = 100 - \left[\left(\frac{\left| \overline{LD}_{Auto} - \overline{LD}_{Manual} \right|}{\overline{LD}_{Manual}} \right) * 100 \right] \tag{2.5}$$

where

$$\overline{LD}_{Auto} = \frac{1}{N} \sum_{i=1}^{N} LD_{Auto_{\mathrm{i}}} \tag{2.6}$$

$$\overline{LD}_{Manual} = \frac{1}{N} \sum_{i=1}^{N} LD_{Manual_{\mathrm{i}}} \tag{2.7}$$

$LD_{Auto_{\mathrm{i}}}$ is the measured automated LD and $LD_{Manual_{\mathrm{i}}}$ is the measured manual LD of a particular image. N is the total number of images in the database.

Second method of precision of merit ($PoM2$) computation was using error difference between the automated and manual methods for each individual case. This is the PoM per image basis. This is mathematically expressed as (Suri *et al.*, 2000):

$$PoM2_{LD}(\%) = 100 - \left[\left(\frac{\sum_{i=1}^{N} \frac{\left| LD_{Auto_{\mathrm{i}}} - LD_{Manual_{\mathrm{i}}} \right|}{LD_{Manual_{\mathrm{i}}}}}{N} \right) * 100 \right] \tag{2.8}$$

More details regarding the computation of precision of merit are given in Appendix A.

v. Dice similarity (DSC) and Jaccard Index (JI)

Dice similarity and Jaccard index (Bharatha *et al.*, 2001; Jaccard, 1912) were computed to find the similarity between two regions. Assume region A represents the area

enveloped by the automated segmentation and region B represents the area enveloped using manual tracings or GT. Then, DSC is the ratio of area in common to both region A and region B to the average size of region A and region B. This can be expressed mathematically as (Bharatha *et al.*, 2001):

$$DSC = \left(\frac{A \cap B}{A + B}\right) * 200 \tag{2.9}$$

Although very similar to Dice, Jaccard index shows the ratio of area in common to both region A and B to the total size of region A and B available (Jaccard, 1912):

$$JI = \left(\frac{A \cap B}{(A + B) - (A \cap B)}\right) * 100 \tag{2.10}$$

Other than the above metrics, different plots and statistical tests can be used for validating the segmentation results. Receiver operating characteristic (ROC) analysis (Golemati *et al.*, 2007) assesses the specificity and sensitivity of the segmentation methods. The regression plots show the variability between auto and manual tracings which is seen by the deviation from the trend line. Generally, this is a line of best fit through the data of two variables, and the Pearson correlation coefficient (r) indicates how far away all these data points are to this line of best fit. The Bland-Altman plot used the Bland-Altman method that demonstrates the level of agreement between two methods when measuring the same variable (Bland and Altman, 1986). Cumulative frequency plots are used to show the error distributions between auto and manual, whereas box plots will illustrate the median as a measure of central tendency.

The statistical tests can be used to check the agreement between true and measured value of a variable. Often, the algorithm that has the best agreement with GT is considered to have the best performance. Due to the trade-off of agreement between bias and precision, the best performing algorithm (agrees best with GT) is not necessarily the best in terms of bias or precision. Use of statistical tests solves this problem. For example, ANOVA test for one-way analysis of variance check the difference be-

tween the means of auto and the manual measurements of a variable (say LD) (Howell, 2012), whereas, Chi-Square test (Altman, 1990) is used to analyze whether there exist a significant difference between the observed data (automated measurements) and the expected data (manual measurements or GT). There are other tests such as Student's T-test and Mann-Whitney test which were used to confirm the statistical significance of the obtained results (Hollander *et al.*, 2013; Jackson, 2015). Usually in all the above tests, p-values less than 0.05 will be considered statistically significant unless otherwise specified.

2.4 Summary

We have presented different techniques for the carotid lumen segmentation from MR and B-mode US images which are intended to measure the CAWT/LD/IAD. These techniques include LSM, graph cut, Hough's Transform, fuzzy classification, active contour or Snake based techniques, scale-space, geometrical approaches, local statistics and optimization based approaches. Section 2.2 reviewed the recent literature on the carotid lumen and outer wall segmentation from MR images, whereas the carotid artery segmentation techniques in US images are explored in Section 2.3. Further, a general framework for carotid artery segmentation is presented, and discussed various challenges during segmentation. Finally, a few important evaluation metrics are shortlisted from the literature which is used for assessing the performance of segmentation techniques. The global trend is now toward the complete automation of the segmentation and measurement process, which can assist the clinician. The use of computer-aided measurement techniques has the potential benefit of increased accuracy with less computational complexity and less subjectivity. It is expected that the performance of the methods can be further increased with the rapidly growing development of technology such as 3D carotid imaging and video segmentation. However, more validation studies will be required to establish the state-of-the-art on segmentation performance.

CHAPTER 3

MAGNETIC RESONANCE IMAGE DENOISING AND MEASUREMENT OF CAROTID ARTERY WALL THICKNESS

In this chapter, carotid artery wall segmentation from MR images is addressed. MR images are inherently corrupted with noise which hides important visual information and thereby affects the performance of the segmentation algorithms. Thus, a robust filter, named as NLML$_{DCT}$, is proposed to reduce the Rician noise present in MR images. This filter is based on the non-local maximum likelihood (NLML) technique using discrete cosine transform (DCT) as the similarity measure. The method is explained in detail in Section 3.1 along with the experimental results on both simulated and real images. Further, the performance of the proposed denoising method is compared against the conventional NLML technique.

In Section 3.2, a novel segmentation strategy is presented for carotid lumen and outer wall segmentation from T1-weighted MR images and quantified the carotid artery wall thickness (CAWT). The segmentation method utilized the famous Chan-Vese (CV) model which is followed by particle swarm optimization (PSO) to separate the inner and outer wall region of the carotid artery. Then, CAWT is measured as the average distance between the inner and outer wall borders. The results are thoroughly validated against the manual tracings by an experienced radiologist.

3.1 DCT Based NLML Filter for MR Image Denoising

MR images are generally corrupted with noise, which is mainly thermal in origin and is produced by the stochastic motion of free electrons. The noise variance is influenced by the imaging parameters, the number of averages, the field of view and the sampling interval (Parker and Gullberg, 1990). One straight forward approach to reduce the noise level in the acquired image is to average images after multiple acquisitions. Averaging will reduce the noise level by a factor of $\sqrt{N}$, where N is the number of acquisitions. Averaging, however, may not be feasible in clinical and small animal MR imaging where there is an increasing need for speed (Manjón *et al.*, 2008; Rajan *et al.*, 2011). Thus, post processing techniques to reduce the noise level in the acquired data are important. Also, time-sensitive acquisitions in contrast material-enhanced studies, functional studies, diffusion MRI (dMRI) or studies with limited imaging time, experiments cannot be repeated to do averaging (Rajan *et al.*, 2011).

In most of the early papers on MRI denoising, the conventional classical denoising techniques were applied with the assumption that the data in the magnitude MRI follows a Gaussian distribution. In these methods the biasing effects of Rician noise was not taken into account. This bias will increase with decreasing signal to noise ratio (SNR). This is demonstrated in Figure 3.1. Many methods were proposed later to denoise MR images. Most of these methods exploited the second moment of the Rice distribution to reduce the bias in the denoised images, i.e. the image is denoised with the methods based on the Gaussian assumption and to reduce the bias, $2\sigma_g^2$ (where σ_g^2 is the variance of noise) is subtracted from the squared denoised image. However, in Sijbers *et al.* (1998) it is demonstrated that the SNR and sample size can influence the process of estimating the true underlying pixel value using this approach. Methods based on maximum likelihood (ML) were proved to be better than the aforesaid methods. Superior performance of ML based methods over other state of the art methods were demonstrated in He and Greenshields (2009) and Rajan *et al.* (2011, 2012).

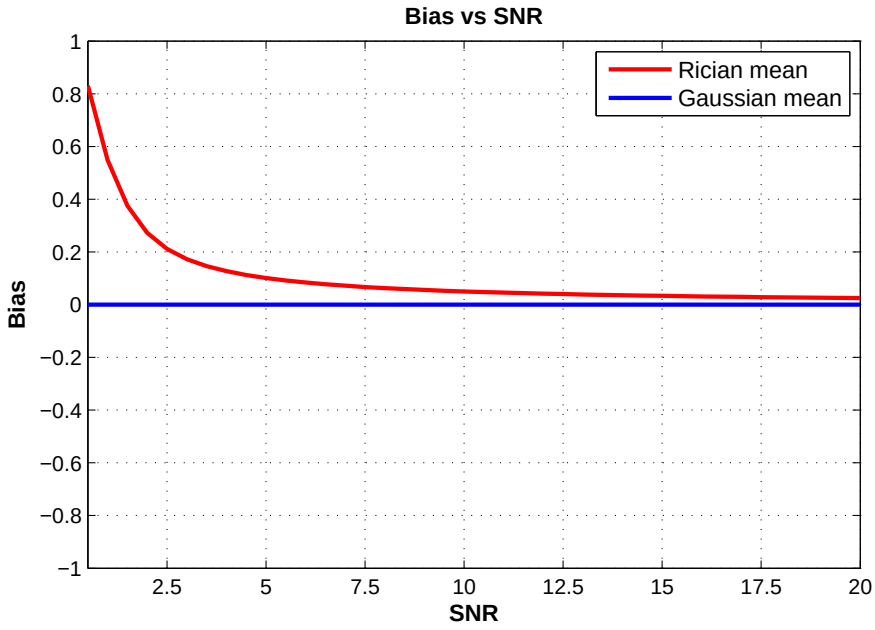

Figure 3.1: Rician Bias : This experiment was conducted with $\sigma_g = 1$ and varying a from 0.5 to 20.

Conventionally, the ML estimation methods for denoising MR images incorporate the Rice distribution in order to estimate the true, underlying pixel value from a local neighborhood. This is based on the constant intensity assumption with in the neighborhood. However, this assumption is not always valid especially around edges and fine structures, which may results in poor quality images. As a solution to this problem, many variations of ML based methods were proposed. Among them, the 2D NLML (NLML$_C$) approach (He and Greenshields, 2009) gained much attention of the research community. The NLML$_C$ differs in its sample selection strategy, i.e. samples are selected in a non-local way, rather than from a local neighborhood, based on the intensity similarity of the pixel neighborhoods. Euclidean distance is used as the similarity measure in the image space. However, it has been recently shown that computing the similarity measure is more robust in DCT sub-space compared to the Euclidean sub-space (this is because of the inherent properties of DCT such as low data correlation and high energy compaction)(Hu *et al.*, 2012). Motivated by this observation, the proposed method integrates DCT into NLML to produce an improved 2D MRI filtration process

which is termed as NLML$_{DCT}$. In the next section, we explain the data distribution in MRI and the signal estimation using the conventional NLML method.

3.1.1 Data Distribution and Signal Estimation in MRI

The raw complex MR data in the k-space are characterized by a Gaussian probability density function (PDF). After the inverse Fourier transform, the noise distribution in the real and imaginary components will still be Gaussian due to the linearity and the orthogonality of the Fourier transform. However, due to the subsequent transform to a magnitude image, the data will no longer be Gaussian but Rician distributed.

Let $\mathfrak{R}$ and $\mathfrak{I}$ represent the real and imaginary parts of the noisy complex MR data (corrupted by zero mean Gaussian, stationary noise with the standard deviation σ_g) with mean values $\mu_{\mathfrak{R}}$ and $\mu_{\mathfrak{I}}$, respectively. Then the reconstructed magnitude data M will be Rician distributed (Rice, 1944). The corresponding Rician PDF is given by:

$$p_{\mathrm{M}}(M|A,\sigma_g) = \frac{M}{\sigma_g^2} e^{-\frac{M^2+A^2}{2\sigma_g^2}} I_0\left(\frac{AM}{\sigma_g^2}\right)\epsilon(M) \tag{3.1}$$

where $M = \sqrt{\mathfrak{R}^2+\mathfrak{I}^2}$, $A = \sqrt{\mu_{\mathfrak{R}}^2+\mu_{\mathfrak{I}}^2}$, $I_0(.)$ is the 0^{th} order modified Bessel function of the first kind and $\epsilon(.)$ is the Heaviside step function. The shape of the Rician PDF depends on the signal to noise ratio (SNR), which is here defined as the ratio A/σ_g.

Given the observed data and a model of interest, the unknown parameters in the PDF can be estimated by maximizing the corresponding likelihood function. Let $M_1, M_2, ..., M_n$ be n statistically independent observations within a region of constant signal intensity A. Then, the joint PDF of the observations is:

$$p(\{M_i\}|A,\sigma_g) = \prod_{i=1}^{n} \frac{M_i}{\sigma_g^2} e^{-\frac{M_i^2+A^2}{2\sigma_g^2}} I_0\left(\frac{AM_i}{\sigma_g^2}\right). \tag{3.2}$$

The unknown parameter in Eq. (3.2) is the true underlying intensity A. However, if σ_g^2 is not known in advance, it can be estimated along with A by maximizing the likelihood

function $\mathcal{L}$ or equivalently $\ln \mathcal{L}$, with respect to A and σ_g^2 (Sijbers and den Dekker, 2004):

$$\{\widehat{A}_{ML}, \widehat{\sigma}^2_{ML}\} = \arg\{\max_{A,\sigma_g^2}(\ln \mathcal{L})\} \tag{3.3}$$

where

$$\ln \mathcal{L} = \sum_{i=1}^{n} \ln\left(\frac{M_i}{\sigma_g^2}\right) - \sum_{i=1}^{n} \frac{M_i^2 + A^2}{2\sigma_g^2} + \sum_{i=1}^{n} \ln I_0\left(\frac{AM_i}{\sigma_g^2}\right). \tag{3.4}$$

and $\widehat{A}_{ML}$ and $\widehat{\sigma}^2_{ML}$ are the estimated underlying true intensity and the noise variance respectively.

3.1.2 Signal Estimation using NLML Method

Non-local approaches generally take advantage of high degree of redundancy in images. In the recent past, these methods attracted the attention of the image processing community and several non-local methods have been introduced for image denoising. NLML method was motivated by non-local means (NLM) (Buades *et al.*, 2011). However, instead of computing the noise free signal as a weighted average of non local pixels, considering the Rician nature of noise, NLML estimates the true underlying signal using Eq. (3.3), where the samples are selected in a non local fashion. Conventionally, NL pixels are selected based on the intensity similarity of the pixel neighborhoods. If the neighborhoods of two pixels are similar, then their central pixels should have a similar meaning and thus similar gray values (Zimmer *et al.*, 2008). The similarity of the pixel neighborhoods can be computed by computing the intensity distance (Euclidean distance) between them (He and Greenshields, 2009):

$$d_{i,j} = \|N_i - N_j\| \tag{3.5}$$

where $d_{i,j}$ is the intensity distance between the neighborhoods N_i and N_j of the pixels i and j. For each pixel i, the intensity distance $d_{i,j}$ between i and all other non local

pixels j as defined by Eq. (3.5), in the search window are measured. After sorting the non local pixels in the increasing order of d, the first n pixels are then selected as $\{M_i\}$ for maximum likelihood (ML) estimation. This method is more effective in terms of preserving edges and fine structures than the local ML estimation. In the next section, we discuss an alternative approach to select the samples for ML estimation.

3.1.3 NLML$_{DCT}$ Filter for MR Image Denoising

The proposed work integrates DCT into NLML to produce an improved filter for MR image denoising. Instead of computing the similarity in the image space as in the conventional NLML, we find the appropriate pixels for ML estimation by computing the neighborhood similarity of pixels in the DCT subspace. Since only few low frequency coefficients are used for distance calculation, the number of computations can be significantly reduced. This reduces the influence of noise on distance calculation.

Let I be the noisy MR image. Initially, the DCT coefficients are computed for each pixel i in I using a neighborhood of size $w \times w$. For every pixel i in the image, the similar pixels j for ML estimation are computed based on the similarity of the DCT coefficients of the neighborhoods of i and j. Let the neighborhood of pixel i be denoted by N_i and the neighborhood of pixel j be denoted by N_j where $i, j \in I$. Assume $C(N_i)$ and $C(N_j)$ denote the coefficients in the DCT subspace corresponding to patches N_i and N_j respectively. The first τ low frequency coefficients of i and j from $C(N_i)$ and $C(N_j)$ are then selected in a zigzag order. The zigzag order is employed to group low frequency coefficients in top of vector and high frequency coefficients at the bottom. Now the distance $d^{\tau}_{i,j}$ between $C_\tau(N_i)$ and $C_\tau(N_j)$ are computed as:

$$d^{\tau}_{i,j} = \|C_\tau(N_j) - C_\tau(N_i)\| \tag{3.6}$$

where C_τ represents the first τ coefficients of C. For each pixel i, the intensity distance $d^{\tau}_{i,j}$ between i and all other non local pixels j as defined by Eq. (3.6), in the search win-

Table 3.1: NLML$_{DCT}$ Denoising Algorithm

Input: Noisy MR image, w, l, and τ
Output: Denoised MR image
Stage 1: DCT Coefficient Estimation 1. For each pixel i in the noisy image calculate DCT coefficients within a grid of size same as similarity window $w \times w$ 2. Select and store the first τ DCT coefficients in a zigzag order in C_i Stage 2: Optimized Denoised Image Estimation 1. For each pixel i in the Noisy Image 1.1. Compare C_i with all C_j in the search window $l \times l$ using Eq. (3.6) and store the results in $d^{\tau}_{i,j}$ 1.2. Select the first n non local pixels j with the minimum $d^{\tau}_{i,j}$ using k^{th} order statistic and let these pixels be M_i 2. Estimate the true underlying intensity of i, A_i using Eq. (3.3)

dow are measured. The non local pixels j are then arranged in the increasing order of $d^{\tau}_{i,j}$ and the first n pixels are selected as $\{M_i\}$ for maximum likelihood (ML) estimation. Further, the proposed work makes use of k^{th} order statistic (David and Nagaraja, 1970) to select the most similar n pixels. This will further reduce the computational burden compared to traditional sorting algorithms. The NLML$_{DCT}$ algorithm is summarized in Table 3.1 and the time complexity comparison of both NLML$_C$ and NLML$_{DCT}$ algorithms is given in Table 3.2.

3.1.4 Experimental Results

To evaluate and compare the proposed method (NLML$_{DCT}$) with the NLML$_C$, experiments were conducted on both synthetic and real MR images. For the experiments on the synthetic data, we used the standard MR image phantom of the brain obtained from the Brainweb database (Cocosco *et al.*, 1997). The phantom image was degraded with Rician noise for a wide range of noise levels and the denoising efficiency of both algorithms with different search window sizes and noise levels were evaluated based on the peak signal to noise ratio (PSNR) (Fisher, 1995) and the mean structural similarity

Table 3.2: Time Complexity Analysis of Denoising Algorithms

For an $N \times N$ image, assume: $l \times l$ - Search window size m - Similarity window size τ - Number of low frequency coefficients of used for finding similarity in DCT domain
For Conventional NLML (NLML$_C$):
Number of computations for calculation of Euclidean distances of a given pixel: m^2l^2 Hence, total number of computations for entire image: $N^2m^2l^2$
For DCT based NLML (NLML$_{DCT}$):
Number of computations for calculation of 2D-DCT coefficients for each pixel: $l^2 \log l$ Number of computations for calculation of Euclidean distances of a given pixel: $m^2\tau$ Hence, total number of computations for entire image: $N^2 \left(l^2 \log l + m^2\tau\right)$

index matrix (SSIM)(Wang *et al.*, 2004).

Figure 3.2 shows the visual quality comparison of the image denoised with the NLML$_C$ method and NLML$_{DCT}$ method. This experiment was conducted on the brain image after corrupting the image by noise with $\sigma_g = 15$. Both filters were executed with the following parameters: search window size = 21×21, neighborhood size = 3×3 and the the sample size k was chosen as 25 (as recommended in He. et.al (He and Greenshields, 2009)). In visual analysis, the expectations are (i) perceptually flat regions should be smooth as possible (ii) image edges and corners should be well preserved (iii) texture detail should not be lost and (iv) few or ideally no artifacts (He and Greenshields, 2009; Chen *et al.*, 2010; Rajan *et al.*, 2011). It can be observed from Figure 3.2 that the image denoised with the proposed method (NLML$_{DCT}$) is closer to the original one (based on the above mentioned criteria) than the images denoised with the other approaches. The difference is more clear from the images in Figure 3.3, which shows the zoom view of the denoised images of the region marked in red. It can be seen from Figure 3.3 that the blurring effect is less in the image denoised with NLML$_{DCT}$.

Figure 3.4 shows the quantitative analysis and the time complexity comparison of the images denoised with NLML$_C$ and NLML$_{DCT}$ for different search window sizes.

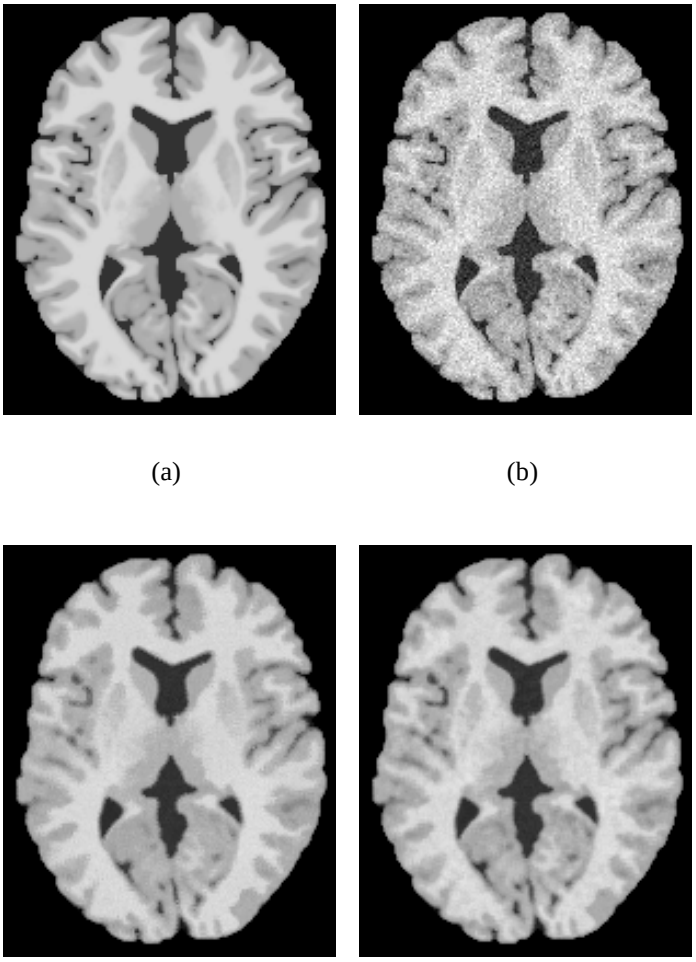

(a) (b)

(c) (d)

Figure 3.2: Visual quality comparison: (a) Ground Truth (GT) (b) GT corrupted with noise (with σ_g = 15) (c) noisy image denoised with NLML$_C$ (d) noisy image denoised with NLML$_{DCT}$.

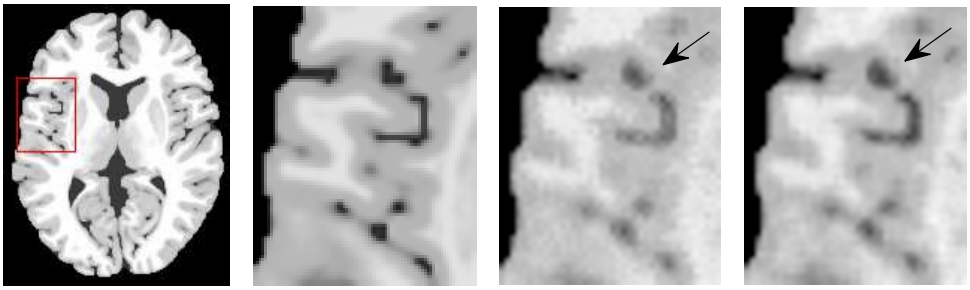

(a) (b) (c) (d)

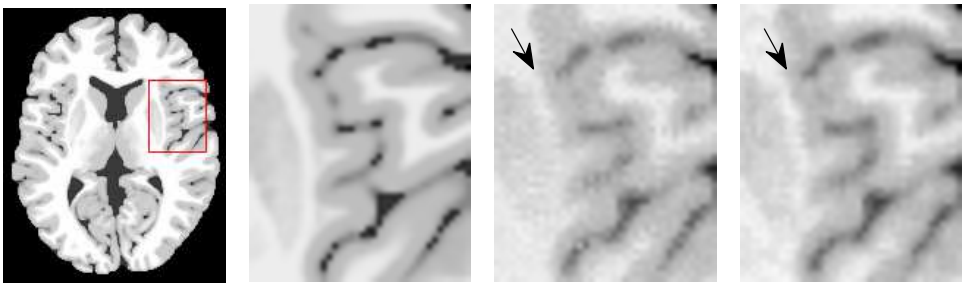

(e) (f) (g) (h)

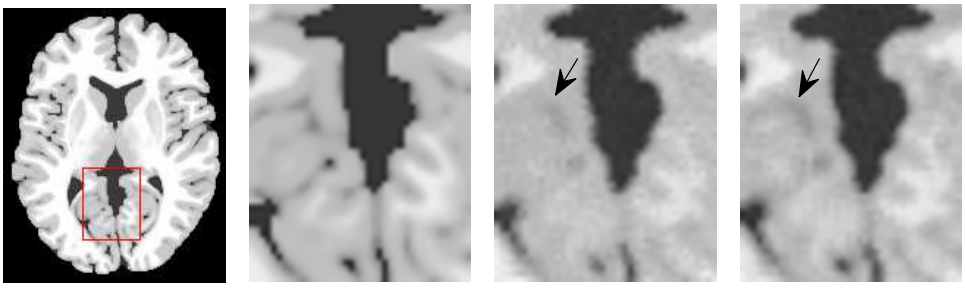

(i) (j) (k) (l)

Figure 3.3: Visual quality comparison : (First column) Ground Truth (Second column) enlarged view of the area marked in red color(Third column) enlarged view after denoised with NLML$_C$ (Fourth column) enlarged view after denoised with NLML$_{DCT}$.

In the quantitative analysis, the background was excluded; that is, only the area of the image inside the skull was considered. Figure 3.4(a) and Figure 3.4(b) shows the performance of both methods based on PSNR and mean SSIM for search window size varying from 11×11 to 101×101. As expected we can observe that the performance of both the methods improves when search window size increases and this is because the probability of finding a similar patch increases when the search space increases. However, one drawback of increasing search space is the corresponding increase in time complexity. This can be seen in Figure 3.4(c). The NLML$_{DCT}$ scores over NLML$_{C}$ here. Figure 3.4(d) and Figure 3.4(e) shows the quantitative analysis based on mean SSIM and PSNR for both methods for various noise levels varying from 10 to 40. At very low noise levels it can observed that for this experiment the PSNR for the conventional NLML is less than the noisy one. This is because of some slight blurring introduced in the image through denoising. Nevertheless, the NLML$_{DCT}$ performs better than NLML$_{C}$ in all the cases.

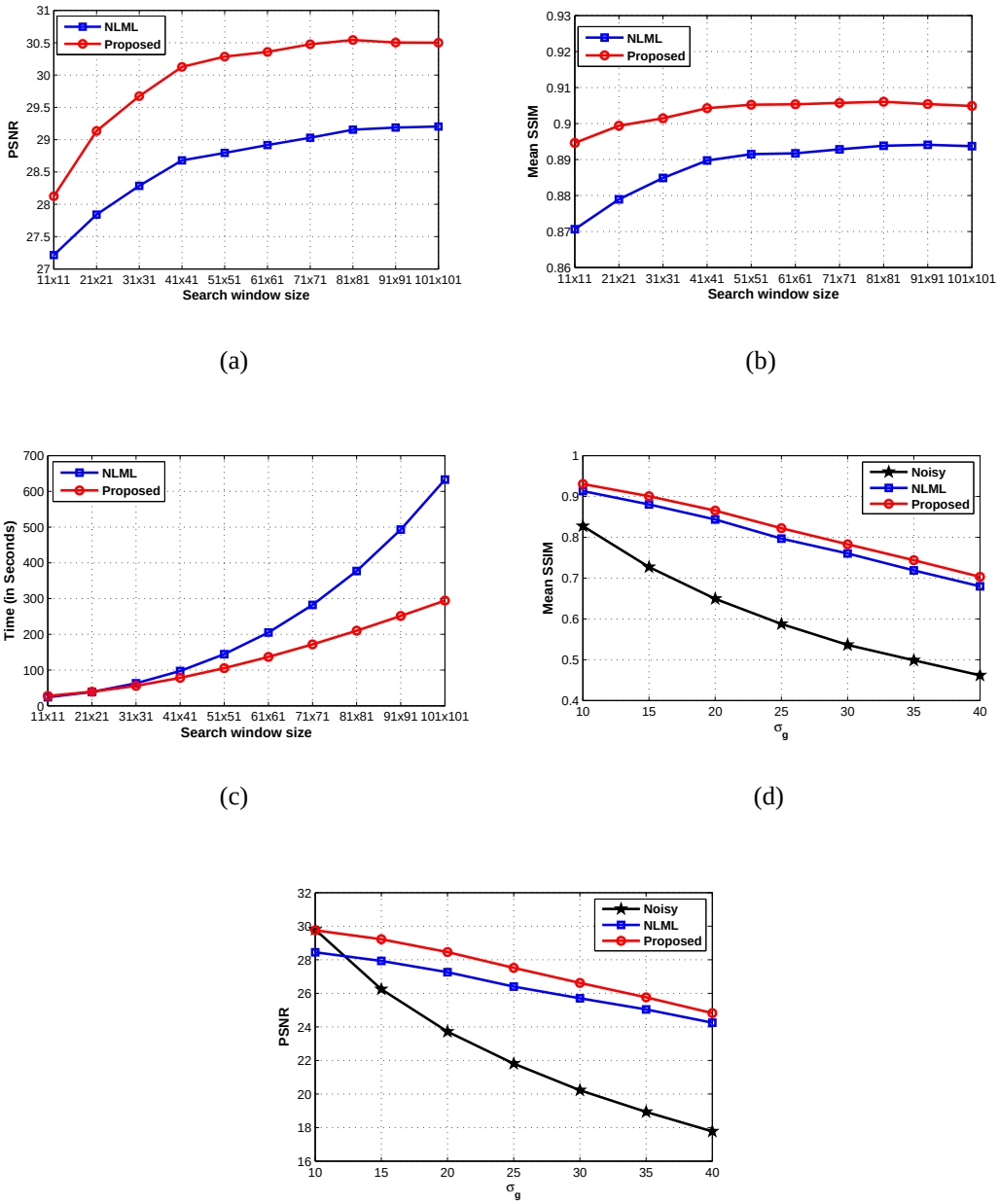

Figure 3.4: Quantitative analysis : (a) PSNR plot of NLML$_C$ and NLML$_{DCT}$ for various search window size (b) Mean SSIM plot of NLML$_C$ and NLML$_{DCT}$ for various search window size (c) Execution time comparison of NLML$_C$ and NLML$_{DCT}$ for various search window size (d) and (e) Mean SSIM and PSNR plot of NLML$_C$ and NLML$_{DCT}$ after varying σ_g from 10 to 40.

Table 3.3: Quantitative analysis on experimental Kiwi fruit image

	NLML_C	NLML_{DCT}	Percentage of Improvement
PSNR	27.53	30.4	10.5

For the evaluation of the methods on the real data sets, we conducted experiments on a carotid MR image and an MR image of a Kiwi fruit. Figure 3.5 shows the results of the experiment on noisy carotid image. It can be observed from the results that the image denoised with NLML_{DCT} preserves structures and fine details much better than NLML_C. In the experiments (with both NLML_C and NLML_{DCT}) we estimated both true underlying signal and noise simultaneously using Eq. (3.3). For both experiments we used a search window size of 11×11 and similarity window size 3×3.

Figure 3.6 shows the results of applying both denoising methods on an MR image of a kiwi fruit. Two sets of kiwi fruit images were reconstructed, one without averaging and the other by averaging 12 acquisitions. Averaging was done in the complex K-space. Averaging reduces the noise standard deviation by a factor of $\sqrt{N}$, where N is the number of averages. These images were acquired on a 9T MR scanner with a slice thickness of 0.4 mm. The denoising algorithms were then applied over the image reconstructed without averaging and the resultant denoised image was compared with the image reconstructed by averaging 12 acquisitions. It can be seen from the denoised images and the residuals that the image denoised with NLML_{DCT} is more close to the image reconstructed by averaging 12 acquisitions. Since the image acquired with 12 averages has a high SNR, for quantitative analysis, we computed the PSNR for denoised images with respect to the image acquired with 12 averages. The PSNR for the image denoised with NLML_C is 27.53 and the PSNR for the image denoised with NLML_{DCT} is 30.4. These results are summarized in Table 3.3. These experiment on the real data sets additionally indicates superior performance of the NLML_{DCT} method over NLML_C method.

However, one drawback with both conventional and the proposed method is in the

optimal selection of the number of samples for ML estimation. In the experiments mentioned in this section, the sample size k is selected as 25 (as recommended in He and Greenshields (2009)). Results can be further improved by selecting an optimal value for k for the ML estimation of the true underlying intensity for each and every pixels instead of fixing k as a constant based on some heuristics. Very recently in Rajan *et al.* (2014) an adaptive approach to select k (for NLML method) based on Kolmogorov-Smirnov (KS) test is proposed. Further research is required to see how this can be incorporated in the proposed DCT based approach.

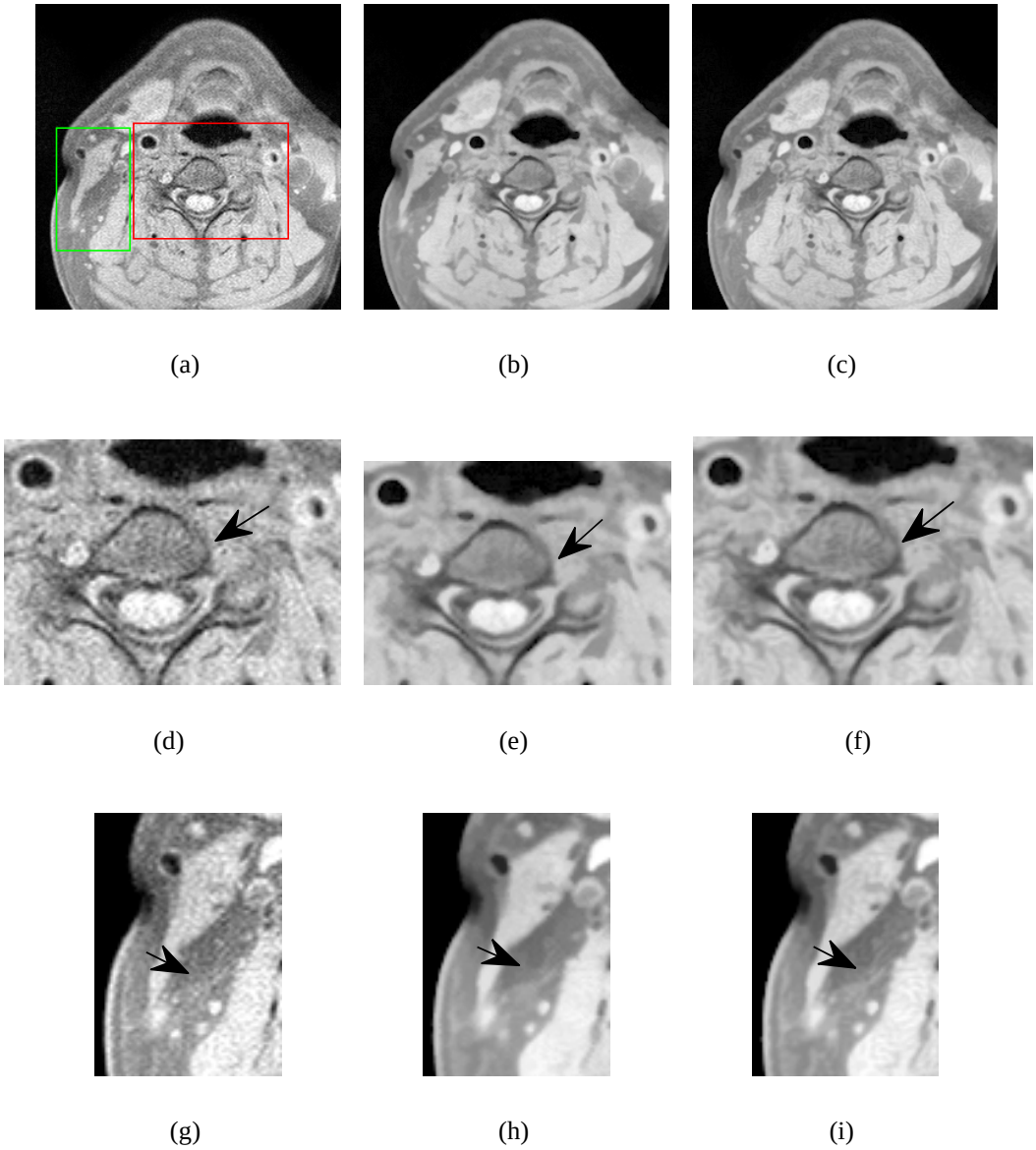

Figure 3.5: Experiments on real data : **(a)** Noisy carotid MR image **(b)** Denoised with NLML_C **(c)** Denoised with NLML_{DCT}, **(d)**enlarged view of the region marked in red in (a), **(e)** and **(f)** enlarged views of the corresponding region marked in red from (b) and (c), **(g)** enlarged view of the region marked in green in (a), **(h)** and **(i)** enlarged views of the corresponding region marked in green from (b) and (c).

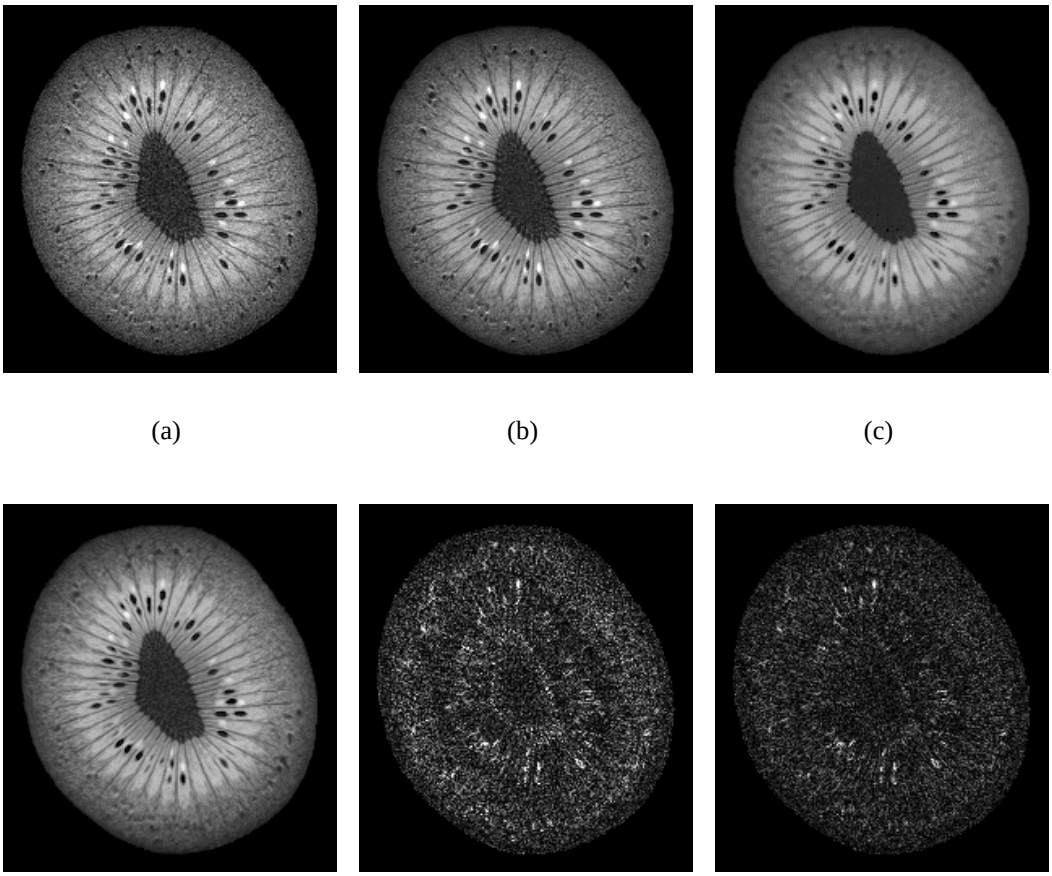

(a) (b) (c)

(d) (e) (f)

Figure 3.6: Experiments on MR image of a Kiwi fruit : **(a)** Original image reconstructed with 1 average **(b)** Original image reconstructed with 12 averages **(c)** image (a) denoised with NLML$_C$ method **(d)** image (a) denoised with NLML$_{DCT}$ method **(e)** and **(f)** residual images (with respect to (b)) of (c) and (d) (in the scale 0-150).

3.2 Carotid Artery Wall Segmentation from MRI

The quantification of carotid artery stenosis via imaging techniques guides the physicians to take a decision regarding surgical interventions. Measurement of the wall thickness from MR images is a promising approach in this regard. Since, manual tracing of the carotid vessel walls is time consuming and sensitive to observer variability, computer assisted automated methods have been under development. In this section, we present a novel segmentation strategy for carotid lumen and outer wall from T1-weighted (T1-w) MR images and quantification of CAWT.

The segmentation has been carried out in two stages which starts with a user assisted region of interest (ROI) selection from the denoised image. In the first stage, an active contour based global segmentation has been applied to classify the lumen region. The famous CV model (Chan and Vese, 2001) has been used at this stage. In the second stage, morphological gradient of the ROI has been computed. This is followed by PSO (Ghamisi *et al.*, 2012) based multi-level segmentation to separate the outer wall region. CAWT has been computed as the average distance between the co-ordinates of the lumen and outer wall borders. The overall block diagram of the segmentation process is given in Figure 3.7.

3.2.1 Global Region based Lumen Segmentation

Chan-Vese (CV) model is a powerful and flexible technique to segment images. This includes images that would be quite difficult to segment by applying certain threshold or gradient based methods. The CV model can be seen as an energy minimization problem, which is reformulated to a simple level set evolution problem. Unlike other active contour models, where the curve evolution is controlled using a stopping edge-function (based on the gradient of the image), the stopping term in CV model is based on the Mumford-Shah functional (Mumford and Shah, 1989). The important point to note here is that the CV model segmentation depends only on global properties such as intensities

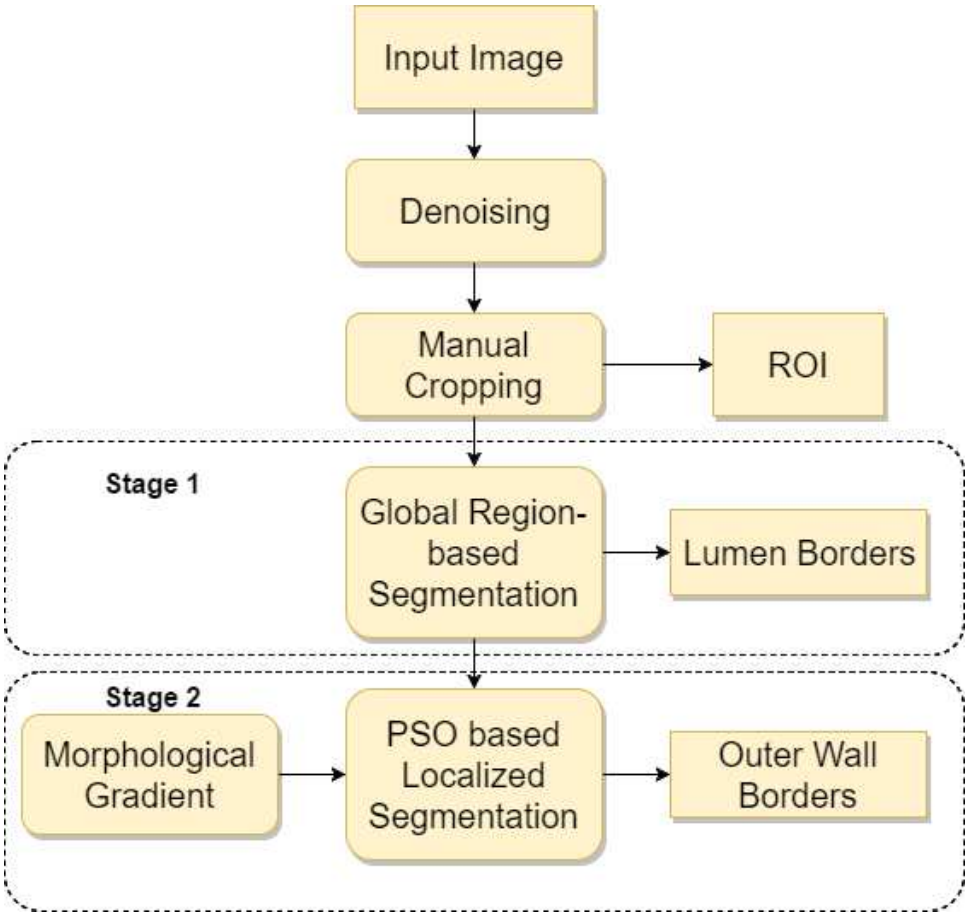

Figure 3.7: Flow diagram showing the segmentation of inner and outer walls of the carotid artery from MR images.

of different regions. Thus, the entire segmentation process becomes independent of local gradients thereby allowing accurate segmentation of regions with discontinuous boundaries. Further, this method does not suffer from a wrong initialization of a curve by the user.

CV Model

Let Ω be a bounded and open subset of $\mathbf{R}^2$, with $\delta\Omega$ as its boundary. Let u_0 be a given image, as a bounded function defined on $\overline{\Omega}$ and with real values. Usually, $\overline{\Omega}$ is a rectangle in the plane and u_0 takes values between 0 and 255. $C(s)$ is a piecewise $C[0,1]$ parameterized curve. The region inside C can be denoted as ω, and the region outside C as $\overline{\Omega}\backslash\omega$. Moreover, $c1$ will represent the mean pixel intensity inside C, and $c2$ will represent the mean intensity outside $C(i.e.\, c1 = c1(C), c2 = c2(C))$.

The CV algorithm tries to minimize the energy functional $F(c1, c2, C)$, defined by (Chan and Vese, 2001):

$$\begin{aligned} F(c1,c2,C) = \mu.Length(C) + \nu.Area(inside(C)) \\ +\lambda_1 \int\limits_{inside(C)} |u_0(x,y) - c_1|^2 dxdy \\ +\lambda_1 \int\limits_{outside(C)} |u_0(x,y) - c_1|^2 dxdy \end{aligned} \tag{3.7}$$

where $\mu \geq 0, \nu \geq 0, \lambda_1, \lambda_2 > 0$ are fixed parameters and can be set by the user. The preferred values are $\nu = 0, \lambda_1, \lambda_2 = 1$. Hence, the objective is to find those $c1, c2, C$ which can be the solution to the minimization problem (Chan and Vese, 2001): $\arg\min_{c1,c2,C} F(c1, c2, C)$.

Level set Formulation

The active contour model with $\nu = 0$ and $\lambda_1 = \lambda_2 = \lambda$ is a particular case of the minimal partition problem. It is possible to reformulate this problem using the level set method. In this case, we will not search for a solution in terms of C, instead, we redefine the problem where $C \subset \Omega$ is represented by the zero level set of some Lipschitz function $\Phi : \Omega \to \mathbf{R}$, s.t.(Chan and Vese, 2001):

$$\begin{cases} C = \partial\omega = \{(x, y) \in \Omega : \Phi(x, y) = 0\}, \\ inside(C) = \omega = \{(x, y) \in \Omega : \Phi(x, y) > 0\} \\ outside(C) = \Omega \backslash \overline{\omega} = \{(x, y) \in \Omega : \Phi(x, y) < 0\}. \end{cases}$$

3.2.2 Morphological Gradient

One non-linear approach to edge detection is by computing the morphological gradient (MG) which is computed as the difference between two images which are obtained by the dilation and erosion of the given image (Dougherty, 1992). Thus, every pixel in the resultant image represents the contrast intensity within the neighborhood. The difference between the maximum and minimum intensity will be small in slowly varying image regions; whereas in regions of fast changing gray values, the difference will be very high. Hence, an edge map can be obtained by applying suitable threshold on the morphological gradient image.

Let $f : E \to R$ be a monochrome image which maps points from a Euclidean space E into the real line R. Let $b(x)$ be a structuring element. Then the MG of f is given by (Dougherty, 1992):

$$G(f) = f \oplus b - f \ominus b \tag{3.8}$$

where $\oplus$ denote the dilation operator and $\ominus$ denote the erosion operator.

3.2.3 PSO based Localized Outer Wall Segmentation

Once we get the gradient image, the next step is to segment the image into distinctive classes by using a set of threshold values. However, the automatic selection of optimal threshold values is challenging. PSO is a fast machine learning technique and have the capability of finding threshold values which are stable (Eberhart *et al.*, 1995). The candidate solutions are generally called as particles which progress through the domain and stops when an optimum solution is found. During this travel, they interact and share information with neighboring particles. The particle success at each step will be evaluated using a well defined fitness function. In simple PSO, it is defined as the between-class variance of the image intensity distributions. The simplest and computationally most efficient method of obtaining a robust optimum $n-$level threshold is by maximizing the between class variance. This can be mathematically formulated as follows. Let there be L intensity levels in the range $\{0, 1, 2, L-1\}$, then the probability of occurrence of each intensity level $i(0 \leq i \leq L-1)$ can be defined as:

$$p_i = \frac{h_i}{N}, \sum_{i=1}^{N} p_i = 1 \tag{3.9}$$

where h_i represents the number of pixels with intensity level i and N rerpresents the total number of pixels in the image. Then, the total mean of the image can be computed as:

$$\mu_T = \sum_{i=1}^{L} i p_i \tag{3.10}$$

Now, the between class variance can be calculated as:

$$\sigma_B^2 = \sum_{j=1}^{n} w_j \left(\mu_j - \mu_T\right)^2 \tag{3.11}$$

where j represents a specific class in such a way that w_j and μ_j are the probability of occurrence and mean of class j, respectively. In other words, the problem of $n-$ level thresholding is reduced to an optimization problem to search for thresholds t_j that maximizes the objective function (Ghamisi *et al.*, 2012):

$$\varphi = \max_{1 <t_1 <\ldots <t_n <L} \sigma_B^2 (t_j) \tag{3.12}$$

The main advantage of using a localized segmentation for the outer wall separation is that, the edge leaking problem can be reduced to some extent. Secondly, we already have precise information regarding the inner lumen region. Hence, the outer wall region which is close to the lumen region can be taken out easily by means of connected component analysis, using 8-connectivity. This is another reason why we go for a two stage process, rather than segmenting both the lumen and outer wall region simultaneously. Figure 3.8 shows the segmentation results on a single image using the proposed method.

3.2.4 Experimental Results

Image Data

We have tested our algorithm on twenty five T1-w carotid MR images acquired from six patients (from SCTMST, Trivandrum). The carotid arteries were examined using a 1.5T Avanto (Seimens, USA) MR scanner. IEC approval was obtained to conduct this study. Both the horizontal and vertical resolution of the images was 0.417 mm/pixel. The segmentation system is evaluated by comparing the automated results against those computed manually. The manual delineation of the inner and outer wall borders was done by an experienced radiologist.

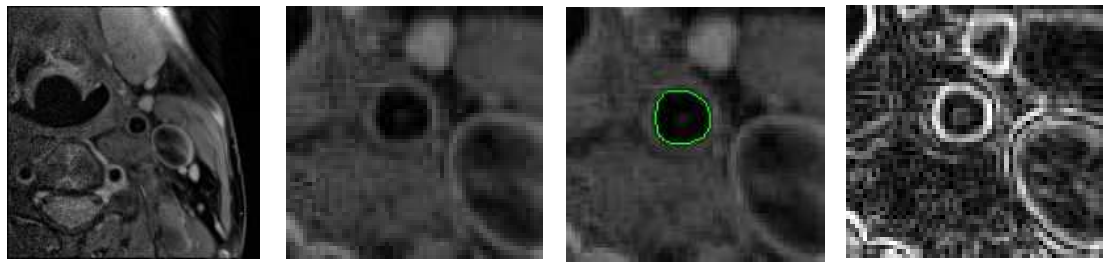

(a) (b) (c) (d)

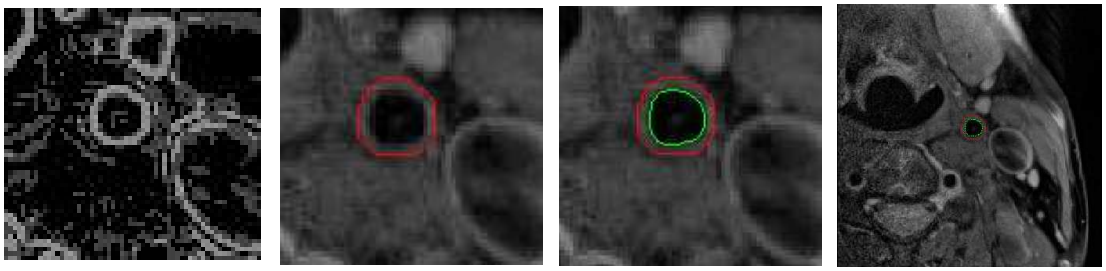

(e) (f) (g) (h)

Figure 3.8: Segmentation results using the proposed method: (a) Denoised MR image of the carotid artery b) Cropped ROI c) Automated lumen border (d) Morphological gradient (e) PSO output f) Automated Outer wall border (g) Overlays on ROI (h) Overlays on raw image.

Performance Evaluation

The following statistical measures have been used for the assessment of the segmentation system. Mean error (ME) and standard deviation (SD) is computed between the automated and manual CAWT. The overall system performance was computed using the first method of precision-of-merit (PoM_1) in percentage(Molinari *et al.*, 2012*c*) as:

$$PoM_1(\%) = 100 - \left[\left(\frac{|\overline{CAWT_{Auto}} - \overline{CAWT_{Manual}}|}{\overline{CAWT_{Manual}}}\right) * 100\right] \tag{3.13}$$

where

$$\overline{CAWT_{Auto}} = \frac{1}{N}\sum_{i=1}^{N} CAWT_{Auto_i} \tag{3.14}$$

$$\overline{CAWT_{Manual}} = \frac{1}{N}\sum_{i=1}^{N} CAWT_{Manual_i} \tag{3.15}$$

$CAWT_{Auto_i}$ is the measured automated carotid artery wall thickness and $CAWT_{Manual_i}$ is the measured manual carotid artery wall thickness of a particular image. N is the total number of images in the database. Dice similarity (DS) and Jaccard index (JI) are computed between the automated and manually segmented binary carotid regions. Further, Student's T-test is performed to prove the statistical significance of the obtained results.

Results and Analysis

Mean Auto CAWT measured for twenty five T1-w MR images was 1.24 ± 0.11 mm, while the manual CAWT was 1.21 ± 0.14 mm. We have got a mean PoM value of 97.1% against manual CAWT which implies sufficient system performance for the intended application. Table 3.4 give detailed performance statistics. Table 3.5 compares the automatic and manually identified binary carotid regions based on the Dice similarity and Jaccard index. If both the regions exactly overlap, Dice similarity or Jaccard index will be 1 or 100%. Here, both the readings are closer to 100 which shows their closeness.

Table 3.4: Performance of Auto CAWT against Manual CAWT

# images	Mean Auto CAWT (mm)	Mean Manual CAWT (mm)	Mean Error (mm)	PoM (%)
25	1.24 ± 0.11	1.21 ± 0.14	0.13 ± 0.08	97.1

Table 3.5: Dice similarity and Jaccard index

	Lumen	Lumen + outer wall
Dice similarity (%)	95	93
Jaccard index (%)	93	90

The statistical significance of the difference between the means of automated and manual CAWT variables is determined by T-test. Since the calculated p-value ($p = 0.2564$) is found to be higher ($p > 0.05$), it is concluded that there is no significant difference between the two means.

It can be observed that the proposed segmentation methodology is in line with previous researches which are slice-by slice methods. In these methods, the user have to perform initialization on every single slice. Further, the segmentation happens sequentially (i.e. segmentation of the inner wall followed by the outer wall). Moreover, previous researches have shown that the segmentation of the outer wall contour is more difficult than the inner lumen contour (Ukwatta *et al.*, 2013; Arias-Lorza *et al.*, 2016). This is because, the image contrast at the inner wall region is usually much better than at the outer wall region.

A comparison of the previous studies describing the carotid artery segmentation methods from MR images is given in Table 3.6. Note that, there are techniques which use images acquired using a different modality such as MR angiography (van't Klooster *et al.*, 2012) to assist the segmentation. Further, some of these studies used more than one MR acquisition protocol (Arias *et al.*, 2012; Arias-Lorza *et al.*, 2016) which need careful image registration before segmentation. All the 2D methods mentioned in the Table 3.6 (Yuan *et al.*, 1999; Adame *et al.*, 2004; Underhill *et al.*, 2006; Saba *et al.*, 2014*a*) need initialization by the user on every slice. The method by Underhill *et al.* (2006) used the IMT measured from B-mode US images for validation purpose. From

the Table 3.6, only three previous studies have measured the CAWT (van't Klooster *et al.*, 2012; Underhill *et al.*, 2006; Saba *et al.*, 2014*a*). Out of these, the method closest to our study is Saba *et al.* (2014*a*) which used a LSM on PD-w MR images. However, in Saba *et al.* (2014*a*), the authors mentioned many drawbacks of their technique including edge leaking problem in the LSM. The proposed technique succeeded in addressing some of these issues by using two different approaches for segmenting the inner lumen and outer wall boundaries of the carotid artery.

Even though we have achieved good accuracy in segmentation, there are certain limitations that need to be addressed. The initial cropping of the raw image to select the ROI must be done in such a way that the carotid artery region appears approximately at the center of the ROI, and must not include any other similar structure. This is because we are initializing the CV algorithm at the center of the ROI and later it will evolve to fit with the carotid lumen region. Further, if the image is too noisy, the CV algorithm may fail to produce accurate results. To address this, we have included a denoising stage in the pipeline prior to the segmentation. The denoising method proposed in Section 3.1 can be used in this regard. Moreover, the segmentation approach presented in this thesis can be extended to 3D MR images.

Table 3.6: Previous studies describing carotid artery segmentation methods

#	Author(Year)	Approach	Dim	Dataset	# images	Performance Criteria	Performance
1	Yuan *et al.* (1999)	Closed Contour Snake search	2D	PD-w MRI	5	Mean Difference (MT) (mm^2)	LA: 1.05±2.26 OWA: 1.36±3.46 WA: 0.31±4.03
2	Adame *et al.* (2004)	Model-based segmentation and Fuzzy Clustering	2D	Short-axis BBMRI	50	CC (MT)	LA: 0.92 OWA: 0.91
3	Underhill *et al.* (2006)	Statistical shape modelling	2D	T1-w-BBMRI	NA	CC (MRI vs. US)	0.95
4	van't Klooster *et al.* (2012)	3D deformable vessel model	Both	3D MRA and 2D MRI	55	CC (MT)	VWT: 0.69 VWV: 0.79
5	Arias *et al.* (2012)	3D coupled surface graph cut	3D	PD-w-BBMRI and EPIMRI	32	Area Overlap (MT) (mm^2)	EPMRI: 84% BBMRI: 85%
6	Ukwatta *et al.* (2013)	Global optimization based multi-region segmentation	3D	T1-w-BBMRI	38	RMSE (MT) (mm)	AB: 0.6±0.1 LIB: 0.5±0.2
7	Saba *et al.* (2014*a*)	Level set method	2D	PD-w MRI	102	CC (MT)	VWT: 0.83
8	Arias-Lorza *et al.* (2016)	3D coupled optimal surface graph-cut	3D	PD-w-BBMRI, PCMRI and EPIMRI	57	Dice Overlap (MT)	WA: 0.86±0.06 LA: 0.89±0.05

MT:Manual Tracing; LA:Luminal Area; OWA:Outer Wall Area; WA:Wall Area; RMSE:Root Mean Square Error
VWT:Vessel Wall Thickness; VWV:Vessel Wall Volume

3.3 Summary

In Section 3.1, we have proposed an improved NLML method based on DCT to denoise the MR images corrupted with Rician noise. In NLML_C method, the neighborhood intensity similarity for selecting similar pixels are generally measured using the Euclidean distance in the image space. In this work we have improved the NLML_C method by incorporating the DCT framework. The estimation of true underlying intensity based on the NLML_{DCT} method is more accurate than the NLML_C. Besides accuracy, the time complexity of the NLML_{DCT} technique is significantly less compared to the NLML_C method for higher values of search window size. Experiments have been carried out on both simulated and real data sets. In Section 3.2, we have presented an algorithm for the semi-automated segmentation of the carotid artery walls from T1-w MR images. The algorithm combines an active contour based global segmentation with PSO based localized segmentation to separate the inner and outer wall regions of the carotid artery. The automatically segmented borders were compared with an independent manual tracing to analyze the performance of the proposed method. This image-based automated system holds significant potential to use in a clinical environment. In future, this work can be extended to do tissue characterization in the segmented regions.

CHAPTER 4

MEASUREMENT OF ARTERIAL DIAMETERS FROM CAROTID ULTRASOUND IMAGES

This chapter starts with a brief discussion in regard to the issue of speckle in ultrasound images. Then in Section 4.2, we present a novel and fully automated algorithm for lumen diameter (LD) and inter-adventitial diameter (IAD) measurements in carotid arteries from B-mode ultrasound images. The proposed algorithm uses a region-based strategy, which is the key contribution of this study. In Section 4.3, we have further improved the performance of this algorithm with an iterative design which uses a spatial transformation to straighten the curved vessels. Comprehensive statistical data analysis was performed to ensure the superior performance of the region-based technique against the two manual expert tracings.

4.1 Speckle Noise in US Images

A granular noise called speckle exists in US images which is signal dependent. The major reason for the speckle is constructive or destructive interference of US waves which produce the light and dark pixels in the image (Michailovich and Tannenbaum, 2006). Speckle degrades the image quality and reduces the contrast which affects the texture-based analysis and segmentation. Further, it blurs the image details significantly (Bamber and Daft, 1986). This makes it really hard for an observer to distinguish between the fine details of the image during clinical diagnosis (Bamber and Daft, 1986). De-speckling techniques are generally trying to remove noise while preserving the fine details in the image. Thus, it is a trade-off between removing noise and preserving

edges. The signal dependent nature of the speckle must be taken into account while designing an efficient speckle reduction filter. The main challenge is to remove the noise component, while keeping integrity of the relevant image information.

A number of techniques are proposed in the literature to reduce the speckle in US images. This includes local statistic filters (Kuan *et al.*, 1985; Lee, 1980), wavelet based filters (Pizurica *et al.*, 2003; Achim *et al.*, 2001), NLM based filters (Coupé *et al.*, 2009; Sudeep *et al.*, 2016), total variation (TV) (Michailovich and Tannenbaum, 2006) and partial differential equation (PDE) based methods (You and Kaveh, 2000). Among them, NLM and PDE based methods gained much popularity. PDE-based de-speckling techniques rely on non-linear diffusion and follow an iterative procedure. By utilizing the coefficient of variation, it simultaneously performs noise reduction and contrast enhancement. Two different de-speckling filters were proposed recently which are based on fourth order and coupled PDE model (by coupling both second and fourth order PDEs) (Soorajkumar *et al.*, 2016*b*,*a*). These methods use the ENI (Edge Noise Interior) concept for controlled diffusion for different image regions. An NLM based approach for speckle reduction was introduced by Coupé *et al.* (2009) which is called as Optimal Bayesian NLM filter (OBNLM). This method exploits the data redundancy in the image and smooths the image very well. In this chapter, we have adopted the OBNLM method to reduce the speckle noise in US images.

4.2 Automated Carotid Lumen Segmentation System

Figure 4.1 shows the flow diagram of the automated carotid lumen segmentation system. We modeled the carotid artery segmentation system as a two stage process: A global system which can establish the ROI and a local system for the extraction of the LI interfaces. The first step in the segmentation is an automated cropping which helps in removing the text information from the image. After cropping, the image is fed to the global system which constitutes stage-1 of our algorithm. Scale-space based strategy is

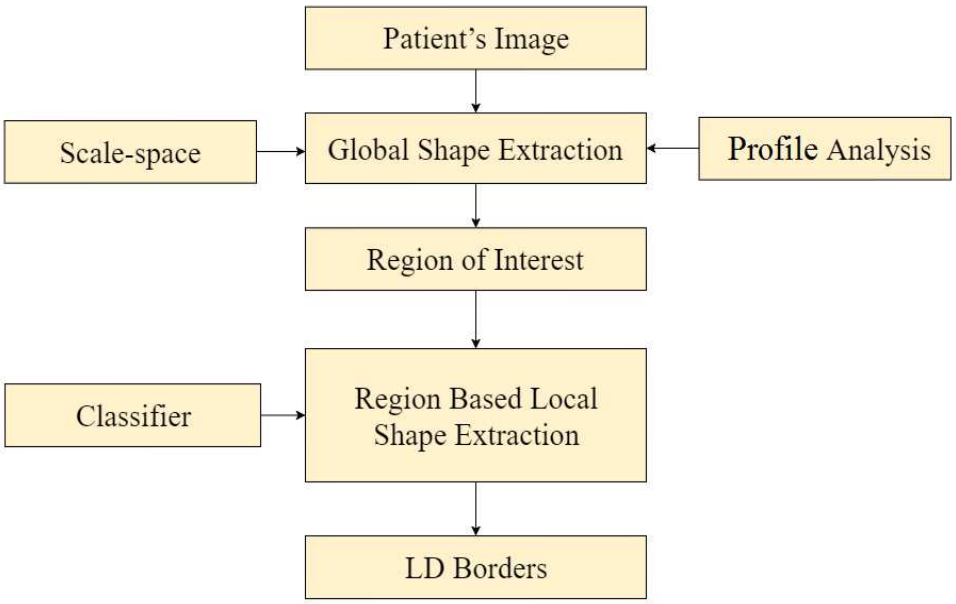

Figure 4.1: Flow diagram of the region based approach for lumen segmentation.

employed at this stage in order to capture the bright edges of the adventitia wall which defines the ROI. Here we used the assumption that the adventitia region is the brightest in an US image due to its high tissue density (Delsanto *et al.*, 2007; Molinari *et al.*, 2012*a*). The ROI covers the region between the near and far MA walls which encloses the lumen region in it. The pixel-classification within this ROI uses the assumption that the blood density to be constant over the lumen region and hence the intensity of pixels corresponding to this region must be constant (Filardi, 2013). This classifier based local processing allows us to extract the LI interfaces accurately. The LD is then measured as the mean distance between the near and far LI interfaces and the IAD is measured as the distance between the near and the far MA interfaces. Both LD and IAD are measured using polyline distance metric (PDM) (Suri *et al.*, 2000). More details regarding the measurement using the PDM method is given in appendix A.

4.2.1 Scale-Space based Global Segmentation

The motivation of the stage-I strategy comes from the fundamental reconstruction of the US image, where the distal (far) wall of the carotid artery has the brightest region (Molinari *et al.*, 2012*a*). This taps the information to build the global shape using the scale-space framework combined with vertical profile analysis. Scale-space based segmentation technique is employed in order to capture the bright edges of the adventitia wall. The adventitial edges were delineated in two steps. The second order derivative of a 5×5 Gaussian kernel (Babaud *et al.*, 1986; Molinari *et al.*, 2012*f*) is computed and convoluted with the cropped image to enhance the edges corresponding to the near and far adventitia walls. The optimal size of the Gaussian kernel is set empirically. The standard deviation of the Gaussian kernel (σ) must be chosen as the minimum MA wall thickness in pixels. Using the previous rationale, we set the value of σ to 12 pixels in our experiments (Molinari *et al.*, 2012*b*,*f*). Convolving an image with derivatives of the Gaussian kernel highlights features of the image with a size larger than the chosen scale σ (Cheng and Li, 2003).

We used vertical profile analysis of pixel columns to trace the adventitial borders. The proximal and distal adventitial borders are approximated as the bright dots (peaks) in the profile. These bright dots are well separated by the dark lumen region in between. In profile analysis, rather than analyzing each column of the image pixels independently, we used a sliding window of size $W \times H = 3 \times 5$ (in pixels) and estimated the mean intensity. This is to overcome any sudden spurious intensity appearing in the profile. This is vital, as it help in detecting the correct peaks from the profile under the scale-space paradigm. By moving the aforementioned sliding window from bottom to top and from left to right, we were able to find the pair of peaks corresponding to the MA borders. The peaks represent high intensity value points with a pool of very small intensity values in between. The ROI is then defined as the region covered by these two MA borders. The output of the global system is the ROI in which the local proximal and distal walls are searched for lumen delineation.

4.2.2 Region based Local Shape Extraction

The region-based model captures lumen intensities under the constant blood density assumption (Filardi, 2013). The ROI captured using the global system have three regions: (a) low intensity lumen region, (b) high intensity or brightest adventitia region and (c) medium intensity plaque region. Thus, we adapt K-mean classifier with three pre-defined classes which is suitable for soft tissue characteristics. On application of the K-mean classifier, we yield three regions from which the lumen region is selected and enveloped in binary form. The holes in the resultant binary lumen are filled via connected component analysis (Soille, 2013) with a pixel connectivity of 8 pixels. The proximal and distal lumen morphologic borders (LI interfaces) are then delineated and the LD is measured using the PDM method (Suri *et al.*, 2000). The segmentation results of the proposed region-based method is illustrated for a single image in Figure 4.2.

4.3 Improved System for LD Measurement in Curved Vessels

The automated lumen segmentation system presented in the previous section has limitations if the orientation of the carotid artery is not straight. Further, it is observed that the segmentation techniques developed so far in the literature are not fully able to handle the curvature associated with the carotid arteries. This motivated us to introduce an improved iterative spatial transformation based technique for segmentation of the carotid artery.

The global system discussed in the previous section is able to extract the ROI which can be used as a guidance zone for the refined local processing for estimating the lumen borders. The ROI containing the lumen axis is the input to the iterative procedure. Prior to the iterative utilization of the scale-space framework, the transformation concept is built which ensure that the curved vessels are straightened for refined and very accurate

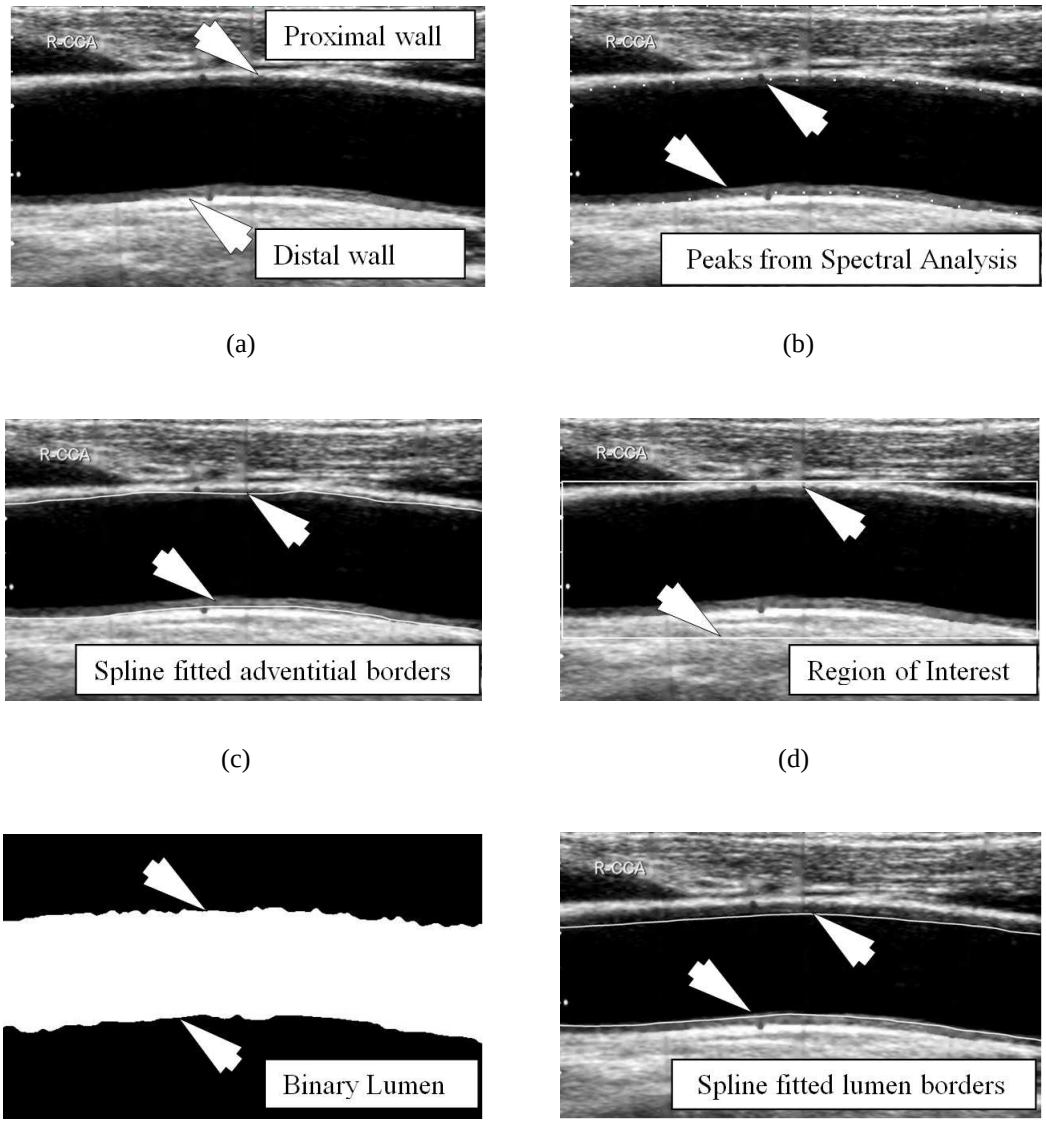

Figure 4.2: Segmentation results on a single image: (a) Cropped image (b) bright adventitial border points detected using vertical profile analysis (c) Spline fitted on these points to show the adventitial borders (d) the resulting ROI is marked with a rectangle extracted using global-shape extraction system (e) binary lumen obtained from the classifier in the ROI using local region-based system (f) final lumen borders after smoothing and spline fitting.

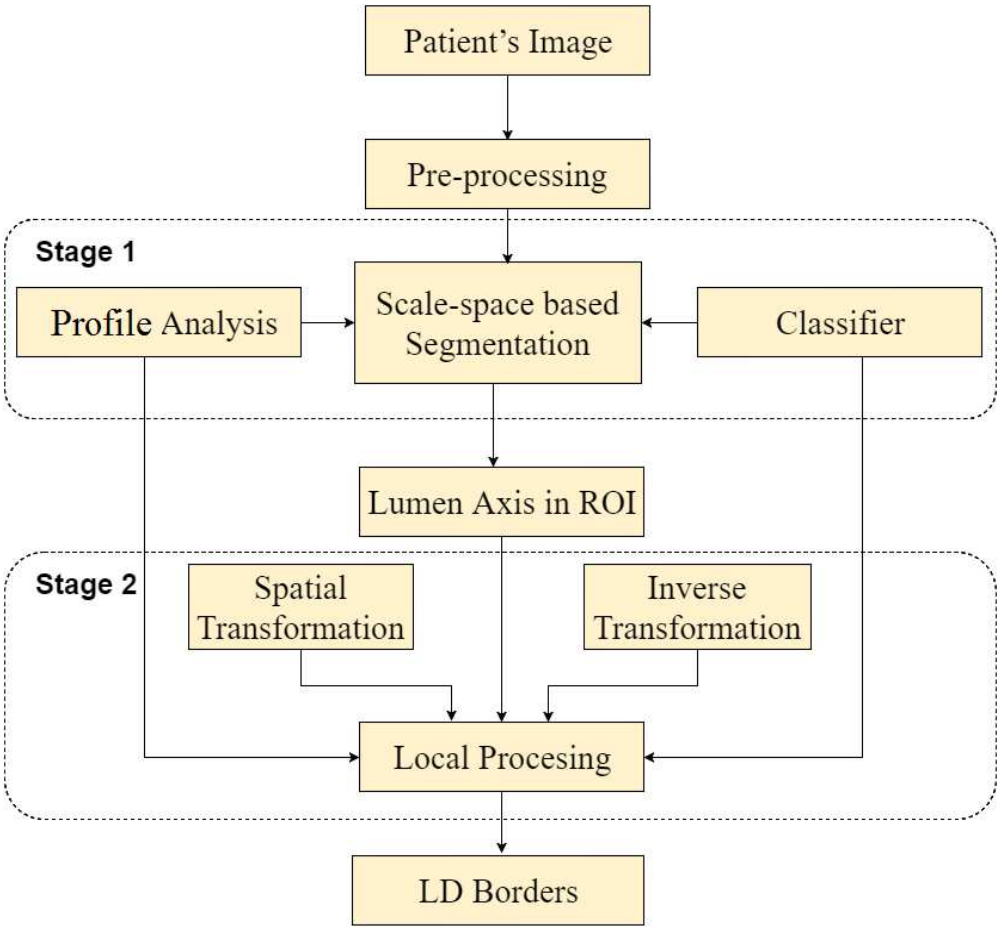

Figure 4.3: Flow diagram of the iterative lumen delineation system.

measurements for LD. Figure 4.3 shows the flow diagram of the improved automated system which works in an iterative manner.

The pre-processing step includes automated cropping and denoising of the input image. We have included an additional denoising step in order to reduce the effect of US speckle and thereby improving the accuracy of the system. Optimized Bayesian non-local means filter (OBNLM) (Coupé *et al.*, 2009) is used for this purpose. This edge preserved smoothing approach will also help in patching the bleeding of the lumen region into the media region at some places along the lumen border. This bleeding otherwise produce over-estimation when tracing the lumen borders using the classifier.

After pre-processing, the image is fed to the scale-space based segmentation system

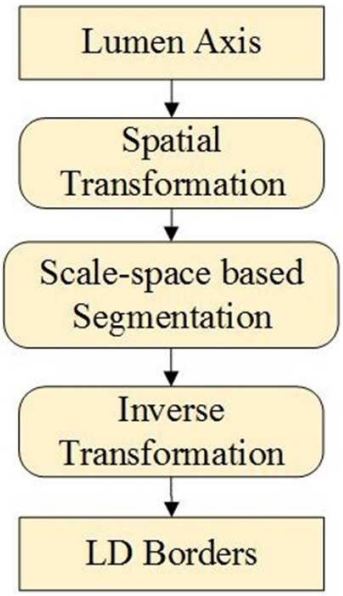

Figure 4.4: Flow diagram of the stage-2 of the automated lumen delineation system.

which constitutes stage-1 of our algorithm. Here we captures the bright edges of the adventitia wall which defines the ROI. K-means classifier is used to extract the lumen region from which the lumen axis is approximated as the mean of the near and far LI borders. The ROI containing the lumen axis is the input to the stage-2 (local processing). Figure 4.4 illustrates the flow of stage 2 in detail. The spatial image transformation makes the curved vessel straight by using the lumen axis. LI borders are then extracted again using the scale-space based approach and then inverse image transformation is applied to map these LI borders back on to the original image.

4.3.1 Spatial Transformation

The heart of the proposed system is a spatial image transformation. The whole idea of introducing the spatial transformation is to improve the performance and stability of the system. To address this issue, we followed an approach presented in Zahnd *et al.* (2014), where a spatial transformation is used to straighten the curved vessels for segmenting the contours of the intima-media complex in the carotid artery wall. Given

an approximation of the lumen axis, the aim of the transformation is to generate a sub-image in which the anatomical interfaces become nearly horizontal. The transformed image I_t is created by applying the spatial transformation T on the original I_W sub-image, such that:

$$I_t = T(I_w) \tag{4.1}$$

The transformation T consists of selecting L pixels above and below the lumen axis in I_W. The detailed algorithm is given in Table 4.1. This approach can overcome the limitations of existing methods that require the image interfaces to be horizontal at the time of acquisition.

Table 4.1: Algorithm for Spatial Transformation

Input: Image (I), (x, y): x and y coordinates of lumen axis
Output: Transformed image I_t
$H =$ Height of image I $W =$ Width of image I $L = H/2$ $y_s = yL$ $x_s = x$ $nW = W$ $nH = 2 * L + 1$ Initialize $I_t(nH, nW)$ to zeros For each raw $i : 1 \rightarrow nW$ of I_t $m = x_s(i)$ $n = y_s(i)$ For each column $j : 1 \rightarrow nH$ of I_t $I_t(j, i) = I(n, m)$ $n = n + 1$ End of for End of for

Figure 4.5 illustrates the algorithmic steps of the proposed technique on a single image having curvature. A visual comparison of the results of both the proposed iterative and the simple scale-space based techniques is given in Figure 4.6.

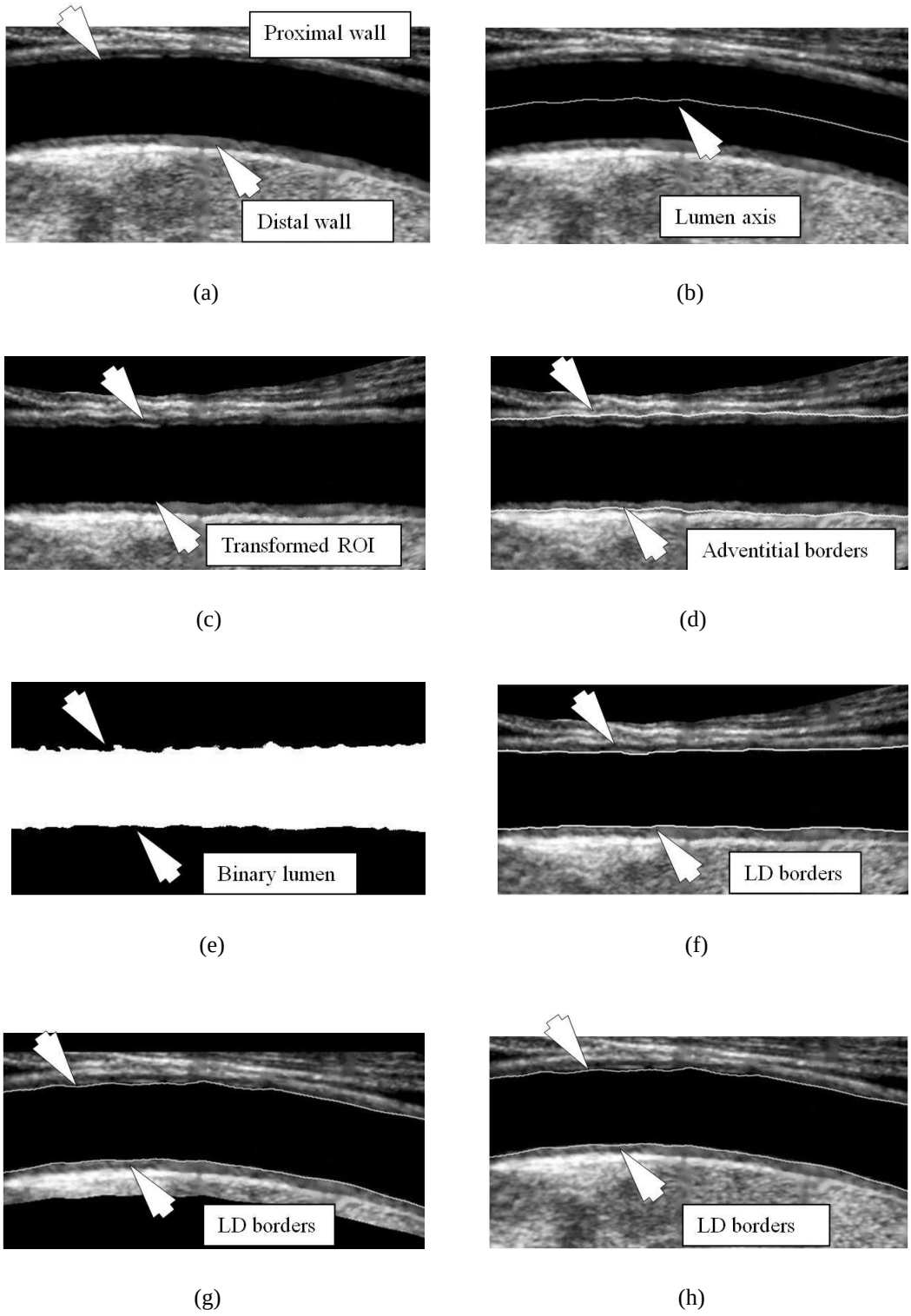

Figure 4.5: Illustrating the algorithmic steps on a single image having curvature. (a) Curved ROI, (b) Lumen axis on the ROI, (c) Transformed ROI, (d) Adventitial borders on the transformed ROI, (e) Binary lumen from classifier, (f) LD borders on the transformed ROI, (g) LD borders on the inverse transformed ROI, (h) LD borders on the original ROI.

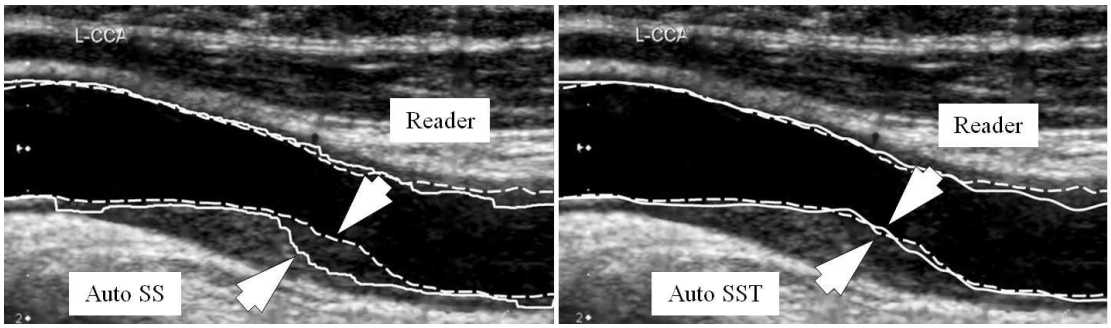

(a)

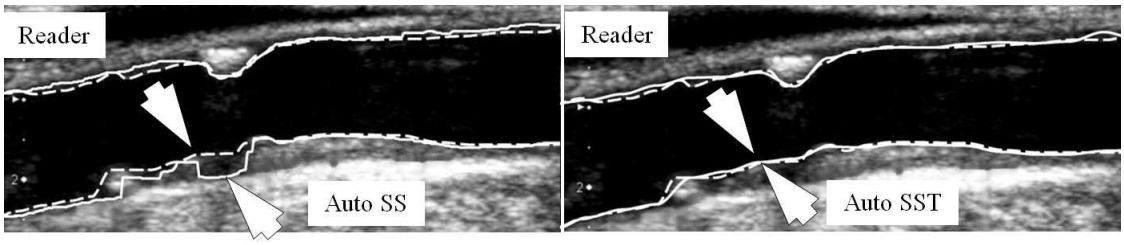

(b)

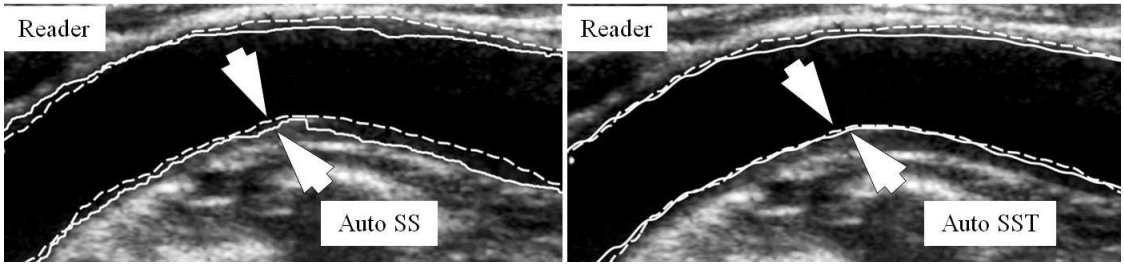

(c)

Figure 4.6: Carotid Auto LD borders compared against the manual tracings on the grayscale images of four patients for both simple scale-space and transformation based iterative methods. Carotid Auto LD borders are shown in solid white; while manual LD borders are shown in dashed white (Auto SS Automated Simple scale-space, Auto SST Automated scale-space with Transformation, Reader Manual Reader).

4.4 Experimental Results

4.4.1 Dataset

Two hundred and two patient's left and right CCA (404 Images) B-mode US images were retrospectively analyzed (ethics approval and IRB granted, Toho University, Japan). Informed consent was obtained from all individual participants included in the study. There were 155 males (76.7%) and 47 females (23.3%) with mean age 67 and 75 years, respectively. These patients had a mean HbA1c of 6.28 ± 1.1 (mg/dl), Glucose 108 ± 31 (mg/dL), LDL cholesterol 101.27 ± 31.6 (mg/dl), HDL cholesterol of 50.26 ± 14.8 (mg/dl) and total cholesterol of 175.04 ± 38 (mg/dl). The ultrasound scanner (Aplio XV, Aplio XG, Xario, Toshiba, Inc., Tokyo, Japan) used to examine the carotid arteries, was equipped with a 7.5-MHz linear array transducer. Same experienced sonographer (16 years of experience) had performed all the scans. The data were acquired in a time period ranging from July 2009 to August 2010. In this database, the vertical resolution was 0.05 0.01 mm/pixel.

The manual delineation of the lumen as well as adventitia borders was done by two experienced Neuroradiologists (one with 15 years of experience and second about 5 years of experience) using ImgTracer^{TM} (AtheroPoint^{TM}, USA), a user-friendly commercial software (Molinari *et al.*, 2012*c*). The two experts selected 15 to 25 edge points proximal to the bulb in orders to delineate the boundaries of the carotid artery. The number of points vary depending upon the length of the carotid artery. The observer had the ability to zoom the image in wall region for better visualization. The output of the ImgTracer^{TM} was ordered set of traced (x,y) coordinates.

4.4.2 Evaluation Methodology

Statistical analyses were performed using Medcalc software (Belgium). The overall system's performance was computed using the method of precision-of-merit (PoM)

(Molinari *et al.*, 2012*c*) in percentage. This is a key feature that evaluate the automatically traced diameters against the manual tracings. Regression plots are used to show the variability between the manual tracings which is seen by the deviation from the trend line. Bland-Altman (BA) plots and cumulative frequency plots are computed to illustrate the data and error distributions. Dice similarity (DSC) and Jaccard index (JI) (Bharatha *et al.*, 2001; Jaccard, 1912) were computed to find the similarity between the two regions. Further, different statistical tests are used for the evaluation of the automated system. Two sample Kolmogorov-Smirnov (KS) test (Hollander *et al.*, 2013) was used to verify that the samples follow the same distribution. Student's T-test was used for testing whether the (strong and highly significant) correlation can be regarded as equality or not (Box, 1987). In all the above tests, p-values less than 0.05 were considered statistically significant unless otherwise specified.

4.4.3 Results and Analysis

In this section, we compare the results of both the simple scale-space based system and the improved transformation based iterative system against the two manual expert tracings on all 404 images in the database. Here, the simple scale-space based technique means the same procedure excluding the spatial transformation based iterative steps. This comparison is to demonstrate the improvement that the spatial transformation step adds. We denote them using the following abbreviations: Auto SS: Automated Simple Scale-space, Auto SST: Automated Scale-space with Transformation. It can be observed that the Auto SST approach improves the performance of the lumen segmentation in curved vessels. However, both the methods mentioned above give the same IAD values, since the spatial transformation improves only the LD measurement.

Automated Carotid LD Measurements

Mean carotid Auto SS LD measured was 6.35 ± 0.97 mm, while mean carotid Auto SST LD measured was 6.31 ± 0.98 mm. Mean carotid LD for the two manual tracings

were 6.19±0.92 mm and 6.23±0.95 mm, respectively. The performance evaluation of the Auto LD values against the two manual tracings is summarized in Table 4.2. It can be seen that there is no significant difference between the auto measurements and the corresponding manual tracings.

Automated Carotid IAD Measurements

Mean carotid Auto IAD measured was 7.80±0.98 mm which is close to the mean carotid IAD for the two manual tracings, 7.76±0.99 mm and 7.89±1.00 mm, respectively. The performance evaluation of the Auto IAD values against the two manual tracings is given in Table 4.3.

Inter-observer variability

Inter-observer differences were estimated by calculating the correlation coefficient (CC) between the measurements on the same subject. The CC between carotid Auto SS LD and the two manual tracings were 0.91 ($p < 0.0001$) and 0.92 ($p < 0.0001$), respectively. Whereas, the CC between carotid Auto SST LD and the two manual tracings were 0.94 ($p < 0.0001$) and 0.95 ($p < 0.0001$), respectively. The scatter diagrams of Auto LD with respect to the two manual tracings are shown in Figure 4.7. These diagrams show the closeness of the automated measurements with the manual ones. The Bland-Altman plots shown in Figure 4.8 give a much clear picture of the data including outliers.

The CC between carotid Auto IAD and the two manual tracings were 0.93 ($p < 0.0001$) and 0.94 ($p < 0.0001$), respectively. The scatter diagrams of Auto IAD with respect to the two manual tracings are shown in Figure 4.9(a) and (b). The Bland-Altman plots of Auto IAD with respect to the two manual tracings are shown in Figure 4.9(c) and (d).

Cumulative Frequency of Signed and Unsigned Errors

The cumulative frequency is an important performance statistic which refers to the error in the automated system. Cumulative frequency of unsigned and signed Auto

Table 4.2: Auto LD Performance

Method	Manual Type	Near wall Error (mm)	Far wall Error (mm)	Mean Error (mm)	PoM (%)
Auto SS	Manual-1	0.30±0.23	0.28±0.17	0.31±0.29	95.8
	Manual-2	0.24±0.16	0.26±0.16	0.28±0.27	96.7
Auto SST	Manual-1	0.25±0.18	0.21±0.18	0.27±0.25	97.7
	Manual-2	0.22±0.15	0.16±0.11	0.25±0.24	98.7

Table 4.3: Auto IAD Performance

Method	Manual Type	Near wall Error (mm)	Far wall Error (mm)	Mean Error (mm)	PoM (%)
Auto SS	Manual-1	0.20±0.17	0.26±0.15	0.23±0.23	97.6
	Manual-2	0.23±0.18	0.23±0.18	0.24±0.24	98.1

LD errors against the manual tracings are computed for both SS and SST methods. The unsigned cumulative frequency shows the total number of measurements with less than a particular error value irrespective of the sign (positive or negative). It has been observed that above 90% of the LD measurements are within 1 mm error compared to the manual tracings. Similarly, the cumulative frequency errors for IAD is computed. It is notable that above 90% of the IAD measurements were done with less than 0.5 mm error with respect to the two manual tracings. Further, it is found that the maximum error value not exceeded 2 mm in any of the cases.

Dice similarity and Jaccard Index

Two similarity coefficients namely Dice similarity (DS) and Jaccard index (JI) have been computed between automatically and manually extracted binary lumen regions (LR). Similarly, these similarity coefficients have been computed for binary inter-adventitial regions (IAR). The results are given in Table 4.4 and Table 4.5. If both regions are equal, then the Dice similarity or Jaccard index will be 1 or 100%.

Table 4.4: Dice similarity and Jaccard index for LR

Method	Auto SS		Auto SST	
Manual Type	Manual-1	Manual-2	Manual-1	Manual-2
Dice Similarity (%)	91.0	92.3	93.9	94.2
Jaccard Index (%)	85.2	86.5	88.6	89.1

Table 4.5: Dice similarity and Jaccard index for IAR

Method	Auto SS	
Manual Type	Manual-1	Manual-2
Dice Similarity (%)	95.1	94.8
Jaccard Index (%)	91.0	90.6

Statistical Tests

Using two-sample KS test, the null hypothesis that the data samples are drawn from the same distribution is retained for Auto SS LD ($p = 0.8328, p = 0.9239$), Auto SST LD ($p = 0.9041, p = 0.9659$) and Auto IAD ($p = 0.9107, p = 0.9422$) in comparison to the corresponding manual tracings.

The null hypothesis for the paired t-test is that the mean difference between paired observations is zero. However, based on the result for Auto SS LD ($p < 0.0001, p < 0.0001$) and Auto SST LD ($p < 0.0001, p < 0.0001$) in comparison to the manual LD tracings, the null hypothesis cannot be retained. As a consequence, the relation between carotid Auto LD and the two manual tracings cannot be regarded as equality (see Table 4.6). Similarly, the result of paired t-test for Auto IAD ($p = 0.0093, p < 0.0001$) shows that the same argument is valid in comparison to the corresponding manual tracings (see Table 4.7).

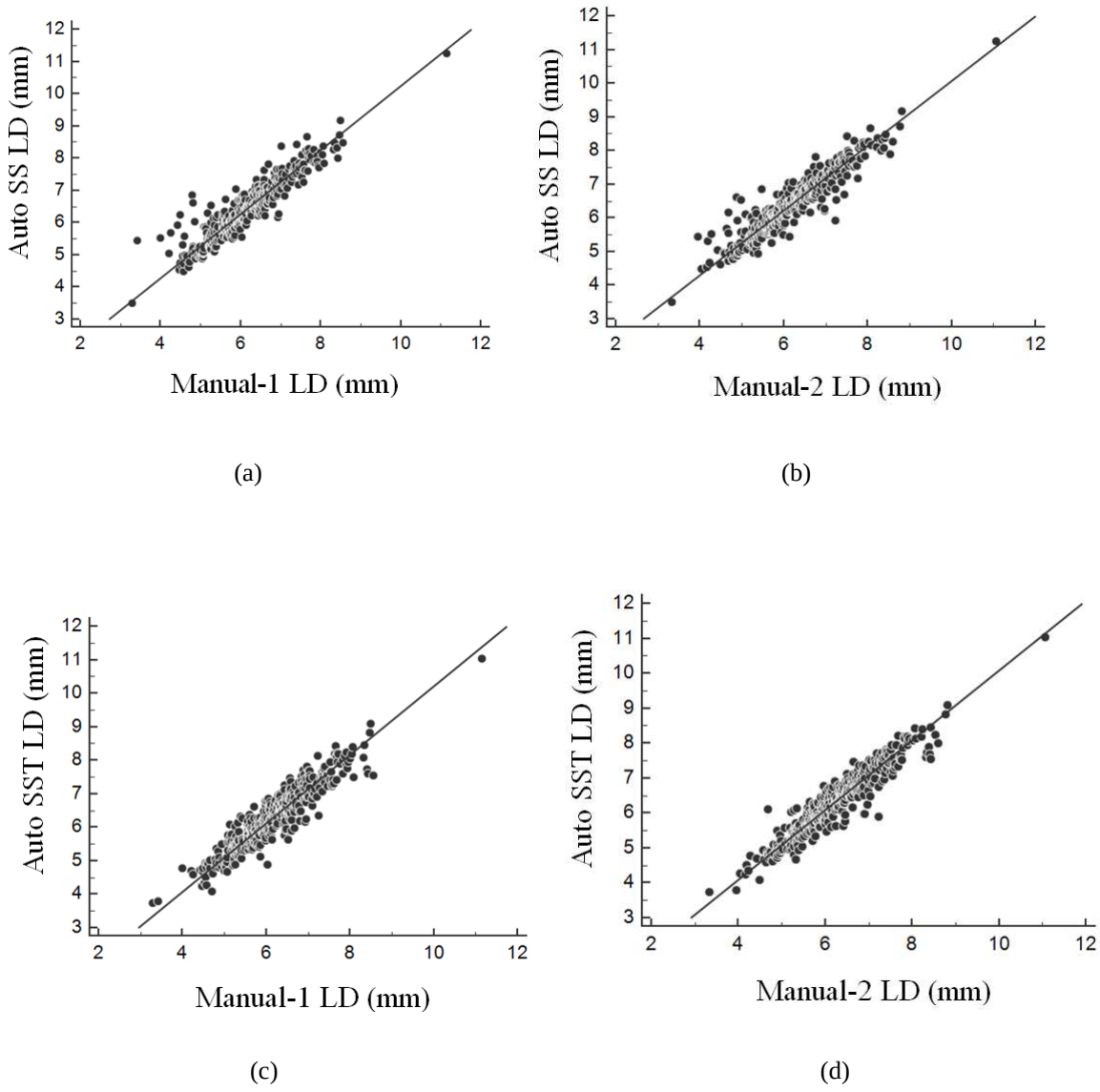

Figure 4.7: Scatter diagrams showing the correlation between (a) carotid Auto SS LD and manual-1 LD, (b) carotid Auto SS LD and manual-2 LD, (c) carotid Auto SST LD and manual-1 LD, (d) carotid Auto SST LD and manual-2 LD.

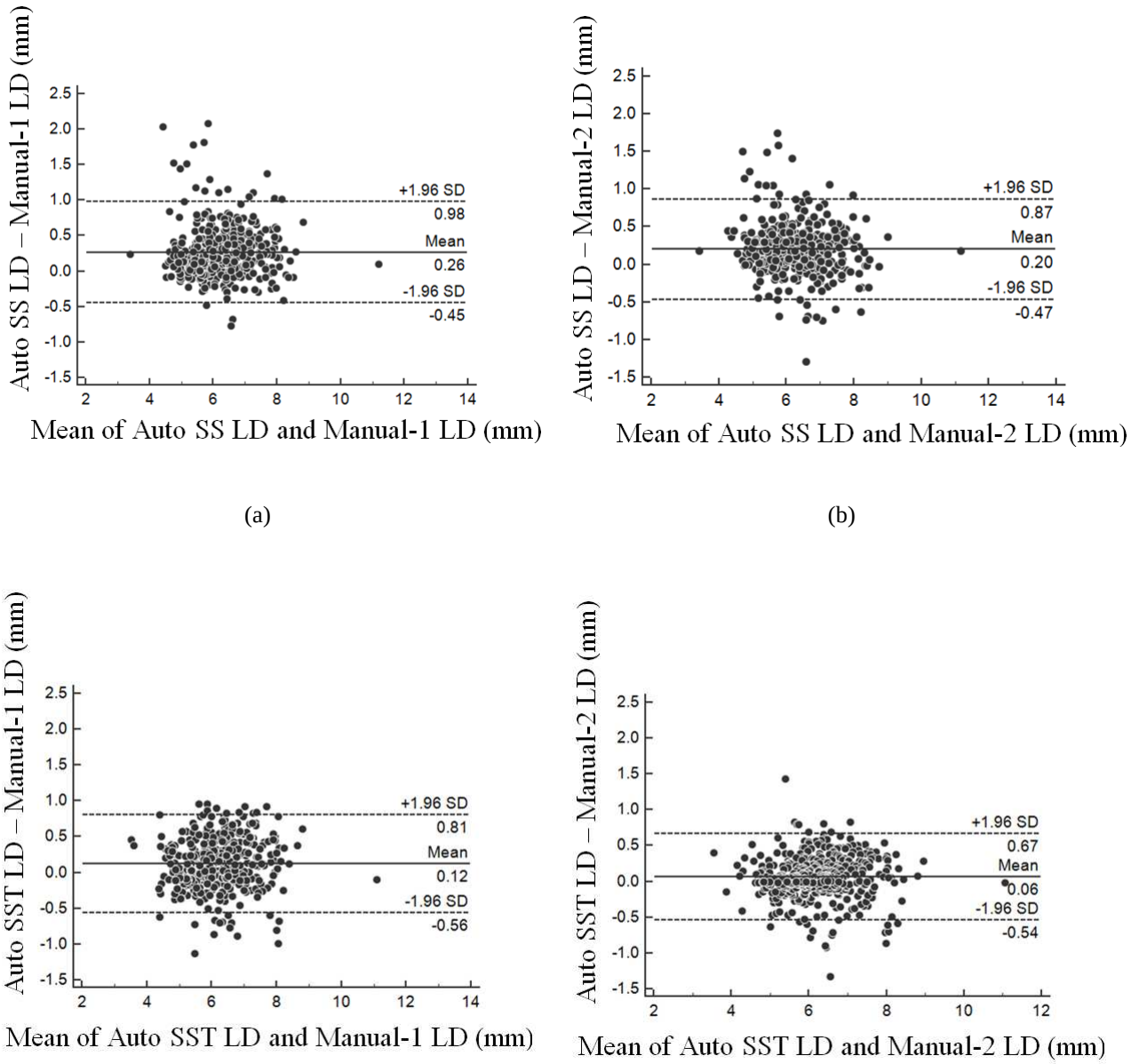

Figure 4.8: Bland-Altman plots between (a) carotid Auto SS LD and manual-1 LD, (b) carotid Auto SS LD and manual-2 LD, (c) carotid Auto SST LD and manual-1 LD, (d) carotid Auto SST LD and manual-2 LD.

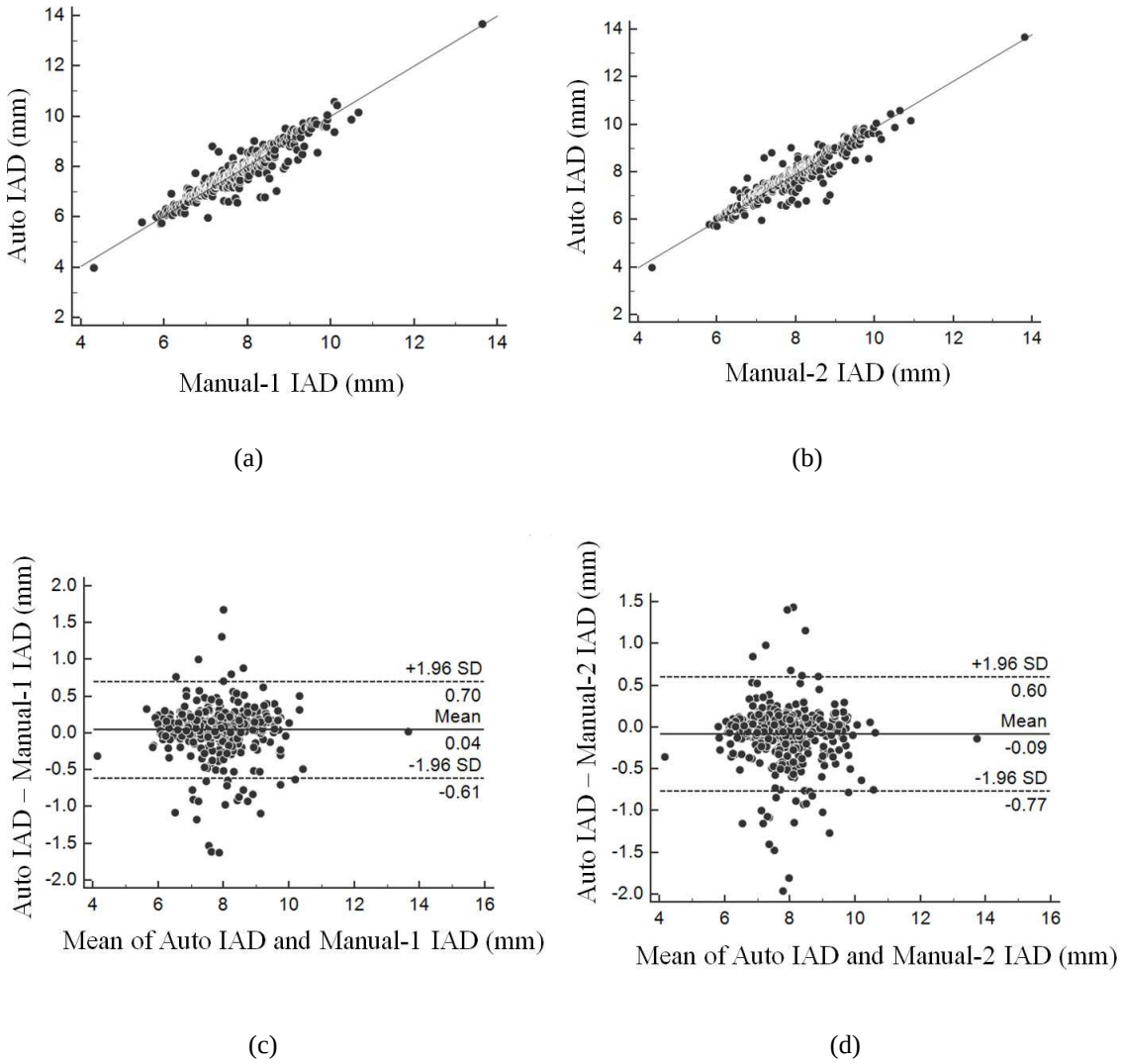

Figure 4.9: Scatter diagrams showing the correlation between (a) carotid Auto SS IAD and manual-1 IAD, (b) carotid Auto SS IAD and manual-2 IAD. Bland-Altman plots between (c) carotid Auto SS IAD and manual-1 IAD, (d) carotid Auto SS IAD and manual-2 IAD.

Table 4.6: T - test for Auto LD vs. Manual tracings

	Auto SS LD vs. Manual-1 LD	Auto SS LD vs. Manual-2 LD	Auto SST LD vs. Manual-1 LD	Auto SST LD vs. Manual-2 LD
Mean difference	-0.2640	-0.2000	-0.1450	-0.08439
Standard error	0.01803	0.01684	0.02041	0.01712
95% CI	-0.2994 to -0.2285	-0.2331 to -0.1669	-0.1851 to -0.1048	-0.1180 to -0.05074
Test statistic, t	-14.640	-11.878	-7.101	-4.931
Degrees of freedom	403	403	403	403
Two-tailed probability, p	$p < 0.0001$	$p < 0.0001$	$p < 0.0001$	$p < 0.0001$

Table 4.7: T - test for Auto IAD vs. Manual tracings

	Auto IAD vs. Manual-1 IAD	Auto IAD vs. Manual-2 IAD
Mean difference	-0.0432	0.0851
Standard error	0.0165	0.0173
95% CI	-0.0756 to -0.0107	0.0510 to 0.1192
Test statistic, t	-2.615	4.914
Degrees of freedom	403	403
Two-tailed probability, p	$p = 0.0093$	$p < 0.0001$

4.5 Discussion

The proposed automated system gives accurate segmentation results for both the near and far LI and MA borders, irrespective of the variation in lumen diameters which are normal, moderately low and medium low representing varying plaque thicknesses. The main advantage of our method is that, it prevents interference of vessel-like structures such as JV and other muscles whose interfering intensities can affect the automated process. Further, we use a non-local mean based denoising to provide robustness to our system. The iterative improved system has a special provision to handle the curved vessels which uses a spatial transformation. Another secondary advantage of our system is that no matter how irregular the plaque is or how bright (hyperechonic) or less bright (hypoechoic) the plaque is, it circumvents these challenges to estimate the LD and IAD automatically. Unlike other existing techniques, the proposed system has only one pa-

rameter σ which was set to 12 pixels (approximate size of minimum MA wall thickness in pixels). This needs to change only if there is a significant variation in the resolution of the image dataset. Hence, the proposed system can be easily adapted to a real time clinical environment. We believe that it can support LD and IAD measurements in clinical practice and can be adapted for stroke monitoring.

To the best of our knowledge, this study is the first fully automated measurement method for LD and IAD, even though similar works have been reported in the literature. However, a direct comparison to previously published results is not easy since different authors may have evaluated their algorithm on different image databases using different performance metrics. Though our system is able to show promising results and has been well validated against the manual tracings, we believe that there is a scope for improving the automated system. The multi resolution technique can be adapted to improve the automated system. More validation needs to be done on other ethnic groups from different countries. Another future scope is to acquire temporal images from each patient to look at the cardiac cycle variations affecting the diameter estimations.

Our lumen region segmentation model is based on the assumption that the blood density is constant. It is very unlikely that this assumption can be disqualified. But there can be cases in which there is no blood in the arterial region during the image acquisition. This can be due to several reasons such (i) as blockage of the artery causing no blood in the other side of the stenosis or (ii) non-uniform pumping of the blood from the heart to brain. In cases like these, there can be multiple gray scale contrasts. Such challenges can be considered by modeling it as a multi-class problem.

4.6 Summary

In Section 4.1, we have presented a fully automated system for the measurement of carotid arterial diameters from B-mode US images. Stage one was a global processing system based on the scale-space framework combined with vertical profile analysis

for extraction of the ROI. The second stage of the algorithm was the local-processing that extracts the lumen interfaces. The algorithm has been modeled as a region-based strategy in a multi-class framework. In Section 4.2, we have presented an improved version of the region-based algorithm where we used an iterative scale-space based strategy which is embedded with spatial transformation. The spatial transformation was designed during the local processing to delineate the lumen borders while handling the curved vessels which are otherwise difficult to compute using conventional methods. We validated our system against the two expert readers and demonstrated high correlations, precision of merit and reliability. Even though, the current results are very promising, more multi-center evaluations need to be performed for adaption in clinical settings.

CHAPTER 5

CLINICAL SIGNIFICANCE AND IMPLICATIONS OF CAROTID ARTERIAL DIAMETERS

This chapter presents the clinical significance and implications of carotid LD and IAD. We believe that the LD and the IAD together might represent a biomarker of stroke risk. The carotid stenosis can be quantified by measuring the LD from B-mode US. Further, the association of LD and IAD with other cardiovascular biomarkers can be utilized to predict the stroke risk. In Section 5.1, we explain the clinical significance of LD and IAD. Then in Section 5.2, we analyze the relationship between automatically measured LD and IAD and an important stroke risk factor named plaque score (PS). In Section 5.3, we compute the stenosis severity index (SSI) of patients in the database based on their automated carotid LD values to predict the stroke risk.

5.1 Clinical Significance of LD and IAD

Non-invasive assessment of the carotid arterial wall thickness using high-resolution US is often used in clinical trials as a surrogate marker of cardiovascular diseases. However, the advantage of using carotid LD/IAD as an imaging biomarker is its ability to provide reliable, accurate and highly reproducible measurements. In patients with significantly high volume of plaque which causes luminal narrowing, LD will be smaller. Hence, LD is inversely related to the stenosis severity. As a result, as LD decreases, it seems reasonable to believe that there may be a resultant increase in the risk of ischemic stroke. Both the European Carotid Surgery Trial (ECST) (Warlow, 1991) and the North American Symptomatic Carotid Endarterectomy Trial (NASCET) (Collaborators *et al.*, 1991)

indicate that the degree of stenosis can be expressed as a percentage reduction in vessel diameter. This is a major point considering the fact that it can be used in determining whether a patient is likely to benefit from endarterectomy or not. As discussed by Fox (1993), stenosis severity is calculated using the ratio of narrowed diameter at stenosis area to normal diameter of the carotid artery. If LD_{narrow} is the measured lumen diameter of the arterial zone with maximum stenosis and LD_{normal} is the measured normal lumen diameter of the artery, then, the stenosis severity index (SSI) in percentage can be formulated as (Fox, 1993):

$$SSI = \left(1 - \frac{LD_{narrow}}{LD_{normal}}\right) * 100 \tag{5.1}$$

The plaque growth inside the lumen leads to a compensatory arterial remodeling. This arterial remodeling is bidirectional in nature depending on the changes in the shear stress. While the positive remodeling results in an expansion of the arteries, negative remodeling may lead to an arterial narrowing (Ward *et al.*, 2000). An increase in the wall shear stress or decrease in the lumen area can lead to dilation of the arterial wall for the normalization of the shear stress (Lafont *et al.*, 1995). The severity of lumen narrowing of atherosclerotic arteries depends on the extent of the accumulation of plaque along the arterial wall. During the initial stages of atherosclerosis, compensatory enlargement of the artery is predominant. This results in an increase in the LD. However, when plaque occupies 30-40% of the vessel area, this adaptive mechanism fails. Further, the inflammatory changes and fibrosis may lead to constriction of the arterial wall, leading to augmentation of the lumen narrowing (Losordo *et al.*, 1994; Pasterkamp *et al.*, 1995). Meanwhile, the plaque growth causes the adventitia region to bulge up according to the Glagov phenomenon (Glagov *et al.*, 1987), which causes the IAD to increase. Because of this positive remodeling, the relationship between LD and IAD is important to consider and together may be useful imaging biomarkers for stroke risk stratification.

Understanding the correlation between LD/IAD and traditional cardiovascular risk factors is important in predicting the risk of stroke. A study by Polak *et al.* (2014)

found that there exist a positive correlation between the carotid IAD and the incident stroke. This study further suggested IAD as a stronger predictor of ischemic stroke in comparison to IMT. In the next section, we analyze the relationship between the carotid LD and IAD and the plaque score (PS). It has been observed that the IAD is more strongly correlated to PS compared to LD.

5.2 Relationship of Carotid Arterial Diameters and Plaque Score

Plaque score (PS) has been used for quantitative analysis of atherosclerotic plaques (Takiuchi *et al.*, 2004). It is associated with future stroke risk and the presence of coronary artery disease (CAD) (Ikeda *et al.*, 2012). PS is computed by adding the maximal thickness in millimeters of plaques in segments taken from internal carotid artery, bulbs and common carotid artery on each side of the neck. The progression of atherosclerotic plaques leads to a compensatory arterial remodeling which can affect the arterial diameters (Vicenzini *et al.*, 2007; Maiellaro and Taylor, 2007; Staub *et al.*, 2010). We thus hypothesized that since the plaque development causes the artery to remodel; there should be a link between the arterial diameters (LD and IAD) and plaque score (PS). We have tested our hypothesis on the same Japanese database mentioned in Section 4.3.1 which contains 404 images acquired from 202 patients.

5.2.1 Correlation between LD/IAD and Plaque Score

A mild positive correlation is found between carotid Auto SST LD and PS, 0.19 ($p < 0.007$). The correlation between the two manual LD tracings and PS were of 0.12 ($p < 0.0767$) and 0.17 ($p < 0.0125$), respectively. A moderate positive correlation was observed between Auto IAD and PS, 0.25 ($p < 0.0006$). The corresponding correlations with the two manual tracings were 0.28 ($p < 0.0001$) and 0.29 ($p < 0.0001$),

respectively. Thus, Auto IAD is more strongly correlated to PS compared to LD. The scatter diagrams of LD and IAD with respect to the PS are shown in Figure 5.1(a) and Figure 5.1(b).

Bland-Altman plots of LD and IAD with PS are shown in Figure 5.1(c) and Figure 5.1(d). It can be seen that the bias is more in the negative difference direction. The analysis is repeated after removing the outliers above and below the 1.96 SD mark as seen from Figure 5.1(c) and Figure 5.1(d). It has been observed that on excluding around 10 outliers, the corresponding CC between (i) LD and PS was 0.25 ($p < 0.0001$); (ii) IAD and PS was 0.38 ($p < 0.0001$), respectively. These results validate our hypothesis.

We have demonstrated a moderate positive relationship between IAD and PS on the entire database and a strong positive relationship between IAD and PS after eliminating 10 outliers (2%). This leads us to believe that IAD may be a significant independent predictor of stroke risk. Further, LD/IAD measurements are left and right sided compared to IMT which is one sided. IMT only provides lipid information in the far wall, unlike LD/IAD which gives indirect reference to lipid walls both sides and also the stenosis information which shows the severity of the atherosclerotic disease (Suri *et al.*, 2010).

The rationale behind the ability of IAD to be stronger compared to LD can be explained using the Glagov phenomenon (Glagov *et al.*, 1987). Here, in spite of the presence of plaque build-up, the LD is maintained; on the contrary, the IAD shows a reflectance of an increase in the wall thickness (Polak *et al.*, 1996). This means that in spite of the increase in lesion mass, arteries remodel to maintain the constant blood flow. This remodeling over a large range of changes in wall mass can cause an increase in the IAD keeping the LD unaltered (Korshunov *et al.*, 2007). Our results demonstrate that IAD is more strongly related to PS compared to LD, which is along the lines of previous studies. Thus, IAD may be a preferable imaging marker of atherosclerosis compared to LD.

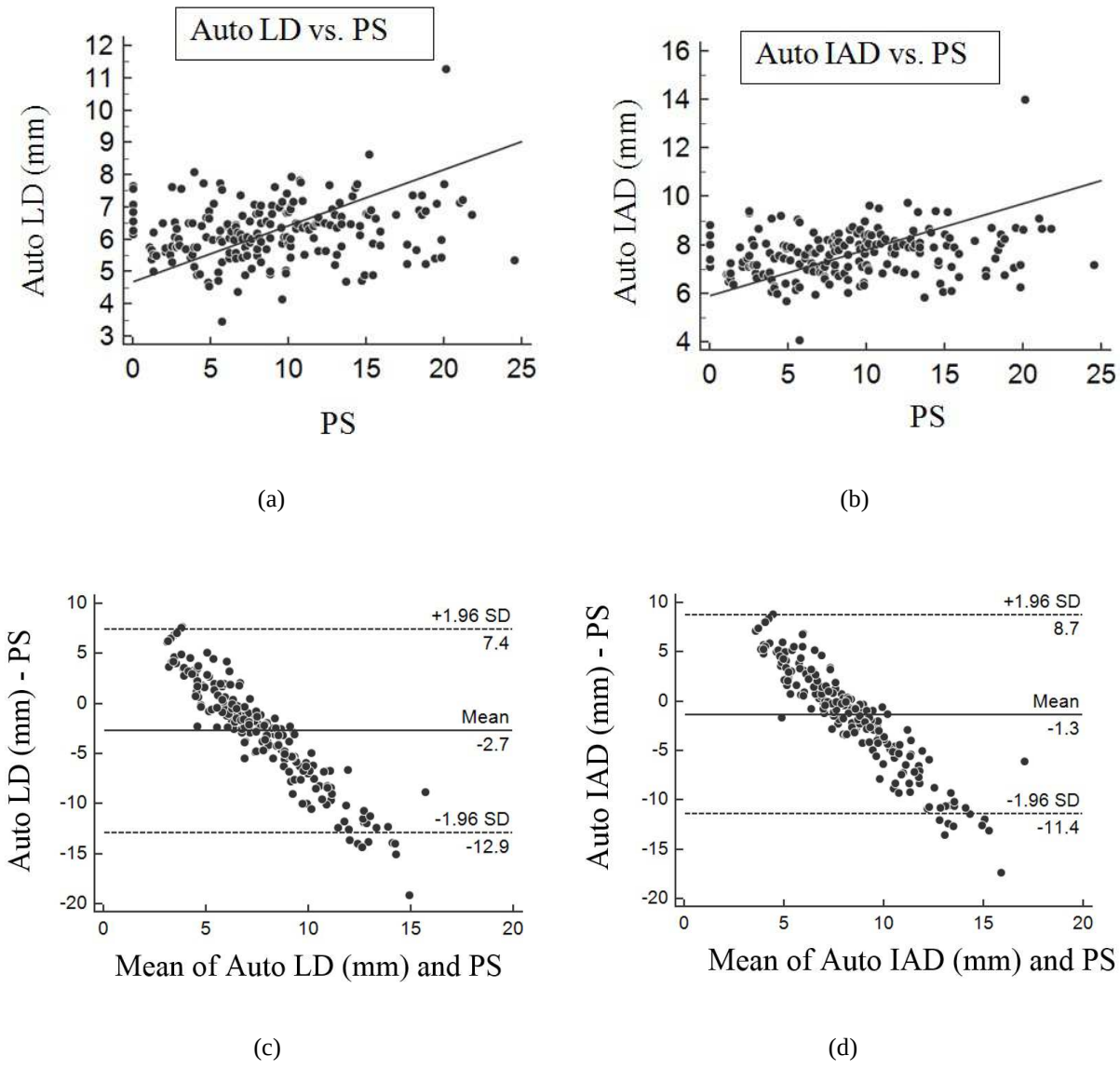

Figure 5.1: (a) Scatter diagram showing the positive correlation between Auto LD and PS (b) Auto IAD and PS; (c) Bland-Altman plot of PS with Auto LD (d) PS with Auto IAD.

5.3 Computation of Stenosis Severity Index

Carotid artery stenosis is an important risk factor of stroke. The ECST and the NASCET have demonstrated that the risk of stroke is reduced by surgery in patients with high grade stenosis (70-99%). In this section, the stenosis severity index (SSI) has been computed for all 404 images in the database using Eq. 5.1 (Fox, 1993) and analyzed the relationship with the respective average or mean carotid LD values. For the purposes of this analysis, we measured the narrowing of the CCA LD and the normal carotid LD. LD_{narrow} is the measured LD at the stenotic zone (arterial zone where the LD is minimum due to plaque deposit) and LD_{normal} is the measured normal LD in the non-stenotic zone (arterial zone which is free from stenosis).

It has been observed that the benefit of surgery in asymptomatic patients is controversial. Some studies indicate that surgery reduces the risk of stroke only in patients with $> 60\%$ stenosis and some others have shown benefits for patients with $> 40\%$ stenosis. Hence, in our analysis, images with $SSI > 40\%$ are categorized as high risk. The detailed analysis results are given in Table 5.1. It can be seen that 9 images in the database are identified as high risk, whereas 47 images are identified as medium risk. Remaining is considered as low risk. Figure 5.2 shows a representative image of a patient with high stroke risk (SSI = 55% and minimum LD = 2.6 mm) in which non-uniform distribution of the plaque causes luminal narrowing.

Figure 5.3 (a) illustrates the cumulative frequency plot of the SSI. This shows the distribution of images in our database based on the SSI. It can be seen that more than 85% images give a low SSI value. Figure 5.3 (b) shows the negative correlation between mean carotid Auto LD and the SSI ($CC = -0.31, p < 0.0001$). The patients with a higher mean carotid LD have a lower SSI value. This is because that a higher mean carotid LD value generally indicates lesser plaques deposited on the carotid artery walls. Thus the difference between the LD_{narrow} and LD_{normal} will be minimum.

Table 5.1: Risk analysis based on SSI

Risk Category	Condition	# images	% images
High Risk	SSI $> 40\%$	9	2.3
Medium Risk	$40\% <$ SSI $> 20\%$	47	11.6
Low Risk	SSI $< 20\%$	348	86.1

5.4 Summary

The clinical significance of carotid LD and IAD is discussed in Section 5.1. We believe that the LD and the IAD together might represent a biomarker of stroke risk. In Section 5.2, we have analyzed the relationship of carotid LD/IAD and PS. We have obtained a moderate positive correlation and IAD is found to be more strongly correlated to PS than LD. In Section 5.3, the SSI of images in the database has been computed and correlated with the corresponding mean carotid LD values. All images has been categorized into high, medium and low risk classes based on SSI values.

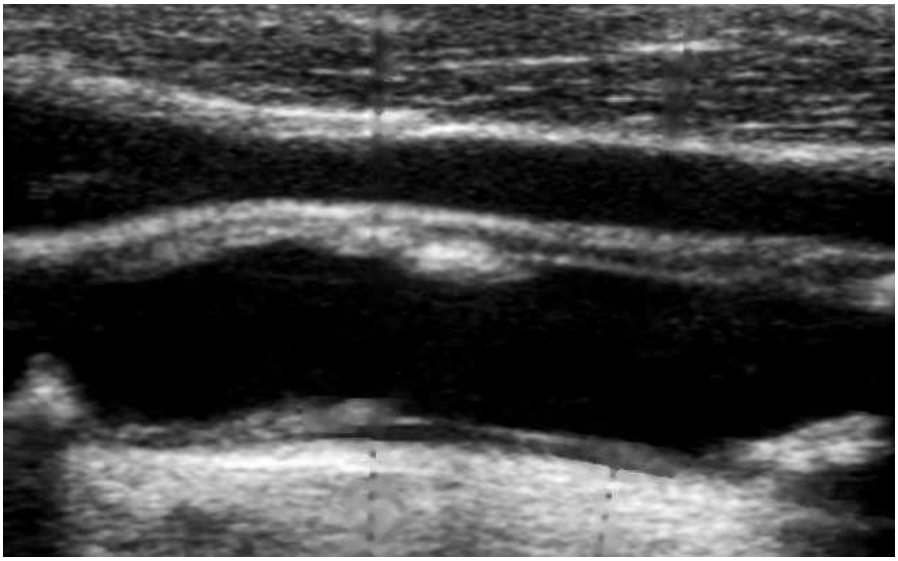

Figure 5.2: Representative image of a patient with high stroke risk (SSI = 55%).

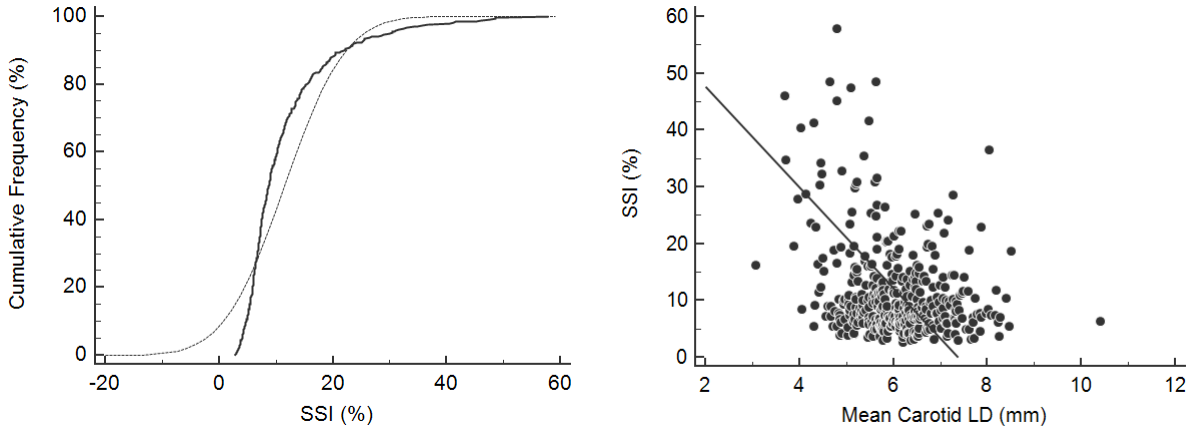

(a) (b)

Figure 5.3: (a) Cumulative frequency plot of SSI, (b) Scatter diagram showing the negative correlation between Mean carotid Auto LD and SSI.

CHAPTER 6

CONCLUSIONS AND FUTURE WORK

6.1 Conclusions

Stroke is one of the most important causes of death in the world and the leading cause of serious, long-term disability. The rupture of atherosclerotic plaques in the carotid artery is the major reason for ischemic strokes. Thus, there is an urgent need for better techniques for diagnosing patients at risk of stroke, and deliver guidelines for the choice of treatment. The changes occurring in the carotid artery can be safely monitored via non-invasive imaging modalities such as MR and US imaging. However, since the manual measurement process is tedious and error prone, automated software systems need to be developed which can measure the wall thickness and diameters of the carotid artery. The development of such automated systems was the primary objective of this research.

We have proposed novel segmentation and measurement techniques in this thesis for both MR and US images of the CCA. As a pre-processing step, a robust denoising filter (NLML$_{DCT}$) has been proposed to reduce the Rician noise in MR images by integrating the DCT into the conventional NLML method. Whereas, one of the widely accepted method named 'OBNLM' is adopted in our work to reduce the speckle noise in US images. The wall thickness of the CCA has been measured from T1-weighted MR images using a two stage process. The segmentation method utilized the famous Chan-Vese (CV) model for the carotid lumen segmentation. This is followed by a PSO based localized segmentation to separate the outer wall region of the carotid artery. This combination of global and localized segmentation strategy helped us to reduce the edge leaking problem to some extent. Finally, the wall thickness has been measured as the

average distance between the co-ordinates of the lumen and outer wall borders. We have got a mean PoM value of 97.1% against the manual expert tracings which implies sufficiant system performance for the intended application.

Due to better reliability, the diameters of the CCA have been measured from B-mode US images via a region-based approach. For this measurement, we have delineated the LI and MA borders of the CCA in two steps. This included a global system which can recognize the ROI and a local system for the extraction of the LI interfaces. Scale-space based strategy is employed at the first stage in order to capture the bright edges of the adventitia wall which defines the ROI. Then by means of vertical profile analysis of the resultant image, the MA borders are delineated. We adapted K-mean classifier with three pre-defined classes for segmenting the lumen region. This classifier based local processing allowed us to extract the LI interfaces accurately. LD and IAD are then measured from the co-ordinates of the LI and MA interfaces, respectively.

We have improved the performance of the above automated system using an iterative spatial transformation based technique for handling the curvature associated with the carotid arteries. Given an approximation of the lumen axis (obtained from the initial application of the scale-space based segmentation method), the aim of the transformation was to generate a sub-image in which the anatomical interfaces become nearly horizontal. The scale-space based segmentation technique is then reapplied on the straight vessels to retrieve the lumen region and LD borders in the transformed framework. The inverse transformation is applied to obtain the LD borders back on to the original image. This approach can address the limitations of the existing methods that require the image interfaces to be horizontal at the time of acquisition and ensures accurate measurements for LD. Comprehensive statistical data analysis was performed to ensure the superior performance of the proposed techniques against the two manual expert tracings. We have got high PoM (98.7% and 98.1%) and CC values (0.95 and 0.94) for both LD and IAD. Further, the clinical significance and implications of the arterial diameters were discussed.

6.2 Future Work

We believe that the proposed image-based measurement system holds significant potential as a tool for stroke and cardiovascular risk stratification. However, more validation needs to be done on other ethnic groups from different countries for its adaption in clinical settings. Significant technical and clinical progress can still be made in the field of carotid artery segmentation. The major challenge in the future will be more towards the development of completely automated integrated systems. One future scope is to acquire temporal images from each patient to look at the cardiac cycle variations affecting the diameter estimations.

Need for an integrated system: Integrated systems are desirable for the clinical experts in order to evaluate the risk of stroke in a precise and efficient way both in asymptomatic and symptomatic subjects (Papadopoulos *et al.*, 2013). Here, integrated system means a system (software application) which is able to segment the carotid artery, measure the LD/IAD/wall thickness, and stratify the atherosclerotic plaque. Such a system should be able to exploit the morphological features of the artery wall. A standard integrated system should have the following stages: normalization and denoising/despeckling, segmentation, feature extraction and selection, and classification (Loizou and Pantziaris, 2015).

Carotid artery segmentation in GPU framework: One of the important issues regarding the modern segmentation algorithms is the computational cost. This results from different factors such as size of the image, number of sampling points and multi-resolution algorithms. For example, if the degree of curvature of an image is more, we need more number of samples to represent the boundary than in case of straight lines. Further, some algorithms use complex iterative steps to achieve high accuracy for the measurement. This in turn requires more processing power than conventional simple approaches which are straight forward. To avoid this limitation, a well-known parallel computing architecture, GPU (graphics processing unit), can be utilized which provides excellent

computing performance gain (up to 54 times faster than the parallel CPU implementation). Different GPUs have different architectures and are equipped with different number of processing cores. Moreover, the technology used to develop these GPU's may vary based on the degree of versatility to be executed in different platforms.

Arterial wall changes during the cardiac cycle: The study of dynamic properties of the wall of carotid artery is becoming more common, since the mechanical and structural properties of the arterial wall may change before the occurrence of clinical symptoms of cardiovascular disease (Selzer *et al.*, 2001). Arterial stiffness indices can be estimated by measuring arterial diameter changes during cardiac cycle using ultrasonography (Gamble *et al.*, 1994). Arterial stiffness may indicate early vascular changes and increased arterial stiffness is often considered as a predictor of carotid atherosclerotic disease. Since the shape of the carotid arterial wall changes during the cardiac cycle, useful information may be obtained from the study of the dynamic arterial geometry (Polak *et al.*, 2012).

Role of carotid bulb lumen in quantification of stenosis: One of the disadvantages of the NASCET method is that it underestimates the size of the plaque in the carotid bulb. It is equally important to measure the minimal residual lumen (at the point of tightest stenosis in the bulb) and the corresponding bulb diameters (Shaalan *et al.*, 2008). Moreover, it has been observed that atherosclerotic diseases occur at sites with complex hemodynamics, such as artery bifurcations, junctions, and regions of high curvature such as the bulb (Nguyen *et al.*, 2008). These elements, along with the complex geometry of a residual lumen in a stenotic carotid bulb, are well understood in theory; however a systematic process to quantify these elements, with verification of their significance, has not yet occurred in a large clinical trial.

APPENDIX A

Polyline Distance Metric and Precision of Merit

Section A.1 presents the mathematical derivation for Polyline Distance Method (PDM) used for the measurement of Auto LD and Auto IAD (Meiburger *et al.*, 2011; Molinari *et al.*, 2012*d*). Section A.2 presents the derivation for Precision of Merit (PoM) (Molinari *et al.*, 2012*f*).

A.1 Polyline Distance Metric

Polyline Distance Metric (PDM) is used to measure the LD as well as IAD. It measure the changes of the contours of the far wall LI interface and near wall LI interface. The first contour used is the far wall LI interface and is denoted by B_1. A point on the first contour B_1 is chosen as the reference point (x_0, y_0). Next, the nearest point at the second contour (near wall LI interface), $B2$ was found using the Euclidean distance. This is the 1^{st} point (x_1, y_1) to be evaluated. Then the 2^{nd} point (x_2, y_2) is established as the point next to the 1^{st} point on the second contour. The two points actually form a line segment, l. Next $d(v, l)$ was obtained which is the distance between the reference point, $v(x_0, y_0)$ and the line segment formed by the 1^{st} point and the 2^{nd} point.

The distance between the 1^{st} point to the reference point is called d_1 whereas the 2^{nd} point to the reference point is called d_2. Another term used in the process towards finding $d(v, s)$ is λ which is the distance of the reference point, v towards the line segment, s. The perpendicular distance between the line segment and the reference point, v, is given by $d^{\perp}$. The formulas to calculate λ and $d^{\perp}$ are given below:

$$\lambda = \frac{(y_2 - y_1)(y_0 - y_1) + (x_2 - x_1)(x_0 - x_1)}{(x_2 - x_1)^2 + (y_2 - y_1)^2} \tag{A.1}$$

$$d^{\perp} = \frac{(y_2 - y_1)(y_0 - y_1) + (x_2 - x_1)(x_0 - x_1)}{\sqrt{(x_2 - x_1)^2 + (y_2 - y_1)^2}} \tag{A.2}$$

Therefore, $d(v, s)$ is obtained using the following equation:

$$d(v, s) = \begin{cases} min(d_1, d_2), & \lambda < 0 \quad \text{or} \quad \lambda > 1 \\ \left|d^{\perp}\right|, & 0 \leq \lambda \leq 1 \end{cases} \tag{A.3}$$

The process to obtain $d(v, s)$ is repeated for the rest of the points of the contour B_1 and is given by:

$$d(B_1, B_2) = \sum_{i=1}^{n} d(v_i, S_{B2}) \tag{A.4}$$

where n, is the number of points in contour, B_1 and S_{B2} is the segment on contour B_2. Secondly, the algorithm above is repeated, where B_2 now becomes the reference contour and B_1 becomes the segment contour S_{B1}. The reverse can be represented by $d(B_2, B_1)$. Lastly combining both $d(B_1, B_2)$ and $d(B_2, B_1)$ will yield the equation below which is the polyline distance metric (Meiburger *et al.*, 2011):

$$D_s(B_1 : B_2) = \frac{d(B_1, B2) + d(B_2, B1)}{(\#\text{vertices} \in B_1 + \#\text{vertices} \in B_2)} \tag{A.5}$$

The word PDM is used which is more convenient expression for Eq. (A.5).

A.2 Precision of Merit

Given $Auto_{LI-NEAR}$ and $Auto_{LI-FAR}$ which are the interfaces computed using the automated method, we compute $Auto\,LD$ using the polyline distance method (Eq. (A.5)) and is given as:

$$Auto\,LD = PDM(Auto_{LI-NEAR}, Auto_{LI-FAR}) \tag{A.6}$$

Similarly, using the definition of PDM, we can compute the LD measurements using manual tracings using Eq. (A.5) and is given as:

$$Observer\ LD = PDM(Observer_{LI-NEAR}, Observer_{LI-FAR}) \tag{A.7}$$

Let $Auto\ LD_i$ be the lumen diameter value automatically computed by the proposed system on the i^{th} image of the database of N patients. If a database of N images is considered, then the overall mean $Auto\ LD$ estimate can be defined as:

$$\overline{AutoLD} = \frac{1}{N}\sum_{i=1}^{N} Auto\ LD_i \tag{A.8}$$

Correspondingly, if $Observer\ LD_i$ is the LD value computed from the radiologist's traced manual measurements, then the mean $Observer\ LD$ is given as:

$$\overline{ObserverLD} = \frac{1}{N}\sum_{i=1}^{N} Observer\ LD_i \tag{A.9}$$

The overall system's performance can be computed using the precision-of-merit (PoM) in percentage as (Molinari *et al.*, 2012*f*):

$$PoM_{LD}\ (\%) = 100 - \left| \frac{\overline{Observer\ LD} - \overline{Auto\ LD}}{\overline{Observer\ LD}} \right| * 100 \tag{A.10}$$

The same procedure is adopted for computing the PoM for IAD measurements and is given as:

$$PoM_{IAD}\ (\%) = 100 - \left| \frac{\overline{Observer\ IAD} - \overline{Auto\ IAD}}{\overline{Observer\ IAD}} \right| * 100 \tag{A.11}$$

REFERENCES

AbuRahma, A. F., **J. T. Wulu**, and **B. Crotty** (2002). "Carotid plaque ultrasonic heterogeneity and severity of stenosis". *Stroke*, **33**(7), 1772–1775.

Achenbach, S., **D. Ropers**, **M. Regenfus**, **K. Pohle**, **T. Giesler**, **W. Moshage**, and **W. G. Daniel** (2001). "Non-invasive coronary angiography by magnetic resonance imaging, electron-beam computed tomography, and multislice computed tomography". *The American journal of cardiology*, **88**(2), 70–73.

Achim, A., **A. Bezerianos**, and **P. Tsakalides** (2001). "Novel bayesian multiscale method for speckle removal in medical ultrasound images". *IEEE transactions on medical imaging*, **20**(8), 772–783.

Adame, I., **R. Van Der Geest**, **B. Wasserman**, **M. Mohamed**, **J. Reiber**, and **B. Lelieveldt** (2004). "Automatic segmentation and plaque characterization in atherosclerotic carotid artery MR images". *Magnetic Resonance Materials in Physics, Biology and Medicine*, **16**(5), 227–234.

Altman, D. G., *"Practical statistics for medical research"*. CRC press, 1990.

Arias, A., **J. Petersen**, **A. van Engelen**, **H. Tang**, **M. Selwaness**, **J. C. Witteman**, **A. van der Lugt**, **W. Niessen**, and **M. de Bruijne**, "Carotid artery wall segmentation by coupled surface graph cuts". *In International MICCAI Workshop on Medical Computer Vision*. Springer, 2012.

Arias-Lorza, A. M., **J. Petersen**, **A. van Engelen**, **M. Selwaness**, **A. van der Lugt**, **W. J. Niessen**, and **M. de Bruijne** (2016). "Carotid artery wall segmentation in multispectral MRI by coupled optimal surface graph cuts". *IEEE transactions on medical imaging*, **35**(3), 901–911.

Babaud, J., **A. P. Witkin**, **M. Baudin**, and **R. O. Duda** (1986). "Uniqueness of the gaussian kernel for scale-space filtering". *IEEE Transactions on pattern analysis and machine intelligence*, **8**(1), 26–33.

Bamber, J. and **C. Daft** (1986). "Adaptive filtering for reduction of speckle in ultrasonic pulse-echo images". *Ultrasonics*, **24**(1), 41–44.

Bharatha, A., **M. Hirose**, **N. Hata**, **S. K. Warfield**, **M. Ferrant**, **K. H. Zou**, **E. Suarez-Santana**, **J. Ruiz-Alzola**, **A. DAmico**, **R. A. Cormack**, *et al.* (2001). "Evaluation of three-dimensional finite element-based deformable registration of pre-and intraoperative prostate imaging". *Medical physics*, **28**(12), 2551–2560.

Bland, J. M. and **D. Altman** (1986). "Statistical methods for assessing agreement between two methods of clinical measurement". *The lancet*, **327**(8476), 307–310.

Blum, A. and **M. Nahir** (2013). "Future non-invasive imaging to detect vascular plaque instability and subclinical non-obstructive atherosclerosis". *Journal of Geriatric Cardiology*, **10**(2), 178–185.

Bots, M. L., **A. W. Hoes**, **P. J. Koudstaal**, **A. Hofman**, and **D. E. Grobbee** (1997). "Common carotid intima-media thickness and risk of stroke and myocardial infarction the rotterdam study". *Circulation*, **96**(5), 1432–1437.

Box, J. F. (1987). "Guinness, gosset, fisher, and small samples". *Statistical Science*, **2**(1), 45–52.

Branas, C. C., **M. S. Weingarten**, **M. Czeredarczuk**, and **P. F. Schafer** (1994). "Examination of carotid arteries with quantitative color doppler flow imaging". *Journal of ultrasound in medicine*, **13**(2), 121–127.

Buades, A., **B. Coll**, and **J.-M. Morel** (2011). "Non-local means denoising". *Image Processing On Line*, **1**, 208–212.

Bushong, S. C., *"Diagnostic Ultrasound: Essentials of Medical Imaging Series"*. McGraw-Hill/Appleton & Lange, 1999.

Carovac, A., **F. Smajlovic**, and **D. Junuzovic** (2011). ”Application of ultrasound in medicine”. *Acta Informatica Medica*, **19**(3), 168–171.

Carr, S., **A. Farb**, **W. H. Pearce**, **R. Virmani**, and **J. S. Yao** (1996). ”Atherosclerotic plaque rupture in symptomatic carotid artery stenosis”. *Journal of vascular surgery*, **23**(5), 755–766.

Carroll, B. (1991). ”Carotid sonography”. *Radiology*, **178**(2), 303–313.

Carvalho, D. D., **Z. Akkus**, **S. C. van den Oord**, **A. F. Schinkel**, **A. F. van der Steen**, **W. J. Niessen**, **J. G. Bosch**, and **S. Klein** (2015). ”Lumen segmentation and motion estimation in b-mode and contrast-enhanced ultrasound images of the carotid artery in patients with atherosclerotic plaque”. *IEEE transactions on medical imaging*, **34**(4), 983–993.

Chan, T. F. and **L. A. Vese** (2001). ”Active contours without edges”. *IEEE Transactions on image processing*, **10**(2), 266–277.

Chen, Q., **Q. Sun**, and **D. Xia** (2010). ”Homogenity similarity based image denoising”. *Pattern Recognition*, **43**(12), 4089–4100.

Cheng, H. and **J. Li** (2003). ”Fuzzy homogeneity and scale-space approach to color image segmentation”. *Pattern Recognition*, **36**(7), 1545–1562.

Chow, T. Y., **J. S. Cheung**, **Y. Wu**, **H. Guo**, **K. C. Chan**, **E. S. Hui**, and **E. X. Wu** (2008). ”Measurement of common carotid artery lumen dynamics during the cardiac cycle using magnetic resonance truefisp cine imaging”. *Journal of Magnetic Resonance Imaging*, **28**(6), 1527–1532.

Cinthio, M., **T. Jansson**, **A. Eriksson**, **Å. R. Ahlgren**, **H. W. Persson**, and **K. Lindström** (2010). ”Evaluation of an algorithm for arterial lumen diameter measurements by means of ultrasound”. *Medical & biological engineering & computing*, **48**(11), 1133–1140.

Cocosco, C. A., **V. Kollokian**, **R.-S. Kwan**, and **A. C. Evans** (1997). ”Brainweb: Online interface to a 3D MRI simulated brain database”; http://www.bic.mni.mcgill.ca/brainweb/ . *NeuroImage*, **5**(4), S425.

Collaborators, N. A. S. C. E. T. *et al.* (1991). ”Beneficial effect of carotid endarterectomy in symptomatic patients with high-grade carotid stenosis”. *New England Journal of Medicine*, **1991**(325), 445–453.

Constantinescu, D., **L. CALMAC**, **M. MARINESCU**, and **M. DOROBANTU** (2012). ”Imaging atherosclerosis by carotid intima-media thickness in vivo: how to, where and in whom?”. *Maedica A Journal of Clinical Medicine*, **7**(2), 153–162.

Coupé, P., **P. Hellier**, **C. Kervrann**, and **C. Barillot** (2009). ”Nonlocal means-based speckle filtering for ultrasound images”. *IEEE transactions on image processing*, **18**(10), 2221–2229.

Dahl, J. J., **D. Hyun**, **M. Lediju**, and **G. E. Trahey** (2011). ”Lesion detectability in diagnostic ultrasound with short-lag spatial coherence imaging”. *Ultrasonic imaging*, **33**(2), 119–133.

David, H. A. and **H. N. Nagaraja**, *Order statistics*. Wiley Online Library, 1970.

de Korte, C. L., **H. H. Hansen**, and **A. F. van der Steen** (2011). ”Vascular ultrasound for atherosclerosis imaging”. *Interface Focus*, **1**(4), 565–575.

Delsanto, S., **F. Molinari**, **P. Giustetto**, **W. Liboni**, **S. Badalamenti**, and **J. S. Suri** (2007). ”Characterization of a completely user-independent algorithm for carotid artery segmentation in 2-d ultrasound images”. *IEEE Transactions on Instrumentation and Measurement*, **56**(4), 1265–1274.

Dougherty, E. R. (1992). ”An introduction to morphological image processing”. *Tutorial texts in optical engineering*.

Eberhart, R. C., **J. Kennedy**, *et al.*, "A new optimizer using particle swarm theory". *In Proceedings of the sixth international symposium on micro machine and human science*, volume 1. New York, NY, 1995.

Eigenbrodt, M. L., **Z. Bursac**, **K. M. Rose**, **D. J. Couper**, **R. E. Tracy**, **G. W. Evans**, **F. L. Brancati**, and **J. L. Mehta** (2006). "Common carotid arterial interadventitial distance (diameter) as an indicator of the damaging effects of age and atherosclerosis, a cross-sectional study of the atherosclerosis risk in community cohort limited access data (ariclad), 1987–89". *Cardiovascular ultrasound*, **4**(1), 1–10.

Eigenbrodt, M. L., **R. Sukhija**, **K. M. Rose**, **R. E. Tracy**, **D. J. Couper**, **G. W. Evans**, **Z. Bursac**, and **J. L. Mehta** (2007). "Common carotid artery wall thickness and external diameter as predictors of prevalent and incident cardiac events in a large population study". *Cardiovascular ultrasound*, **5**(1), 1–11.

Fayad, P. (2007). "Endarterectomy and stenting for asymptomatic carotid stenosis". *Stroke*, **38**(2), 707–714.

Filardi, V. (2013). "Carotid artery stenosis near a bifurcation investigated by fluid dynamic analyses". *The neuroradiology journal*, **26**(4), 439–453.

Fisher, Y. (ed.), *"Fractal Image Compression: Theory and Application"*. Springer Verlag, 1995.

Fox, A. (1993). "How to measure carotid stenosis". *Radiology*, **186**(2), 316–318.

Gamble, G., **J. Zorn**, **G. Sanders**, **S. MacMahon**, and **N. Sharpe** (1994). "Estimation of arterial stiffness, compliance, and distensibility from m-mode ultrasound measurements of the common carotid artery". *Stroke*, **25**(1), 11–16.

Ghamisi, P., **M. S. Couceiro**, **J. A. Benediktsson**, and **N. M. Ferreira** (2012). "An efficient method for segmentation of images based on fractional calculus and natural selection". *Expert Systems with Applications*, **39**(16), 12407–12417.

Gillard, J., **M. Graves**, **T. Hatsukami**, and **C. Yuan**, *"Carotid disease: the role of imaging in diagnosis and management"*. Cambridge University Press, 2006.

Glagov, S., **E. Weisenberg**, **C. K. Zarins**, **R. Stankunavicius**, and **G. J. Kolettis** (1987). "Compensatory enlargement of human atherosclerotic coronary arteries". *New England Journal of Medicine*, **316**(22), 1371–1375.

Godia, E. C., **R. Madhok**, **J. Pittman**, **S. Trocio**, **R. Ramas**, **D. Cabral**, **R. L. Sacco**, and **T. Rundek** (2007). "Carotid artery distensibility a reliability study". *Journal of Ultrasound in Medicine*, **26**(9), 1157–1165.

Golemati, S., **J. Stoitsis**, **E. G. Sifakis**, **T. Balkizas**, and **K. S. Nikita** (2007). "Using the hough transform to segment ultrasound images of longitudinal and transverse sections of the carotid artery". *Ultrasound in medicine & biology*, **33**(12), 1918–1932.

Grønholdt, M.-L. M., **B. G. Nordestgaard**, **T. V. Schroeder**, **S. Vorstrup**, and **H. Sillesen** (2001). "Ultrasonic echolucent carotid plaques predict future strokes". *Circulation*, **104**(1), 68–73.

He, L. and **I. R. Greenshields** (2009). "A nonlocal maximum likelihood estimation method for rician noise reduction in MR images". *IEEE Transactions on Medical Imaging*, **28**(2), 165–172.

Hollander, M., **M. Bots**, **A. I. Del Sol**, **P. J. Koudstaal**, **J. Witteman**, **D. Grobbee**, **A. Hofman**, and **M. Breteler** (2002). "Carotid plaques increase the risk of stroke and subtypes of cerebral infarction in asymptomatic elderly the rotterdam study". *Circulation*, **105**(24), 2872–2877.

Hollander, M., **D. A. Wolfe**, and **E. Chicken**, *"Nonparametric statistical methods"*. John Wiley & Sons, 2013.

Howell, D. C., *"Statistical methods for psychology"*. Cengage Learning, 2012.

Hruska, D. P. and **M. L. Oelze** (2009). "Improved parameter estimates based on the homodyned K distribution". *IEEE transactions on ultrasonics, ferroelectrics, and frequency control*, **56**(11), 2471–2481.

Hu, J., **Y. Pu**, **X. Wu**, **Y. Zhang**, and **J. Zhou** (2012). "Improved DCT-based non local means filter for mr images denoising". *Computational and Mathematical Methods in Medicine*, **2012**, 1–14.

Ibáñez, B., **A. Pinero**, **M. Orejas**, and **J. J. Badimón** (2007). "Novel imaging techniques for quantifying overall atherosclerotic burden: Non-coronary arterial disease (ii)". *Revista Española de Cardiología (English Edition)*, **60**(3), 299–309.

IHA (2015). "Why south asians". `http://indianheartassociation.org/why-indians-why-south-asians/overview/`. Reviewed April 2015.

Ikeda, N., **A. Gupta**, **N. Dey**, **S. Bose**, **S. Shafique**, **T. Arak**, **E. C. Godia**, **L. Saba**, **J. R. Laird**, **A. Nicolaides**, *et al.* (2015). "Improved correlation between carotid and coronary atherosclerosis syntax score using automated ultrasound carotid bulb plaque imt measurement". *Ultrasound in medicine & biology*, **41**(5), 1247–1262.

Ikeda, N., **N. Kogame**, **R. Iijima**, **M. Nakamura**, and **K. Sugi** (2012). "Carotid artery intima-media thickness and plaque score can predict the syntax score". *European heart journal*, **33**(1), 113–119.

Jaccard, P. (1912). "The distribution of the flora in the alpine zone". *New phytologist*, **11**(2), 37–50.

Jackson, S. L., *"Research methods and statistics: A critical thinking approach"*. Cengage Learning, 2015.

Jensen-Urstad, K., **M. Jensen-Urstad**, and **J. Johansson** (1999). "Carotid artery diameter correlates with risk factors for cardiovascular disease in a population of 55-year-old subjects". *Stroke*, **30**(8), 1572–1576.

Jones, S., **H. Leclerc**, **G. P. Chatzimavroudis**, **Y. Kim**, **N. Scott**, and **A. P. Yoganathan** (1996). "The influence of acoustic impedance mismatch on poststenotic pulsed-doppler ultrasound measurements in a coronary artery model". *Ultrasound in medicine & biology*, **22**(5), 623–634.

Kablak-Ziembicka, A., **W. Tracz**, **T. Przewlocki**, **P. Pieniazek**, **A. Sokolowski**, and **M. Konieczynska** (2004). "Association of increased carotid intima-media thickness with the extent of coronary artery disease". *Heart*, **90**(11), 1286–1290.

Korshunov, V. A., **S. M. Schwartz**, and **B. C. Berk** (2007). "Vascular remodeling hemodynamic and biochemical mechanisms underlying glagovs phenomenon". *Arteriosclerosis, thrombosis, and vascular biology*, **27**(8), 1722–1728.

Kramer, C. M. and **J. D. Anderson** (2007). "MRI of atherosclerosis: diagnosis and monitoring therapy". *Expert review of cardiovascular therapy*, **5**(1), 69–80.

Kuan, D. T., **A. A. Sawchuk**, **T. C. Strand**, and **P. Chavel** (1985). "Adaptive noise smoothing filter for images with signal-dependent noise". *IEEE transactions on pattern analysis and machine intelligence*, **7**(2), 165–177.

Ladak, H. M., **J. B. Thomas**, **J. R. Mitchell**, **B. K. Rutt**, and **D. A. Steinman** (2001). "A semi-automatic technique for measurement of arterial wall from black blood MRI". *Medical Physics*, **28**(6), 1098–1107.

Lafont, A., **L. A. Guzman**, **P. L. Whitlow**, **M. Goormastic**, **J. F. Cornhill**, and **G. M. Chisolm** (1995). "Restenosis after experimental angioplasty intimal, medial, and adventitial changes associated with constrictive remodeling". *Circulation research*, **76**(6), 996–1002.

Lamont, D., **L. Parker**, **M. White**, **N. Unwin**, **S. M. Bennett**, **M. Cohen**, **D. Richardson**, **H. O. Dickinson**, **A. Adamson**, **K. Alberti**, *et al.* (2000). "Risk of cardiovascular disease measured by carotid intima-media thickness at age 49-51: lifecourse study". *British Medical Journal*, **320**(7230), 273–278.

Lee, J.-S. (1980). ”Digital image enhancement and noise filtering by use of local statistics”. *IEEE transactions on pattern analysis and machine intelligence*, **2**(2), 165–168.

Liang, Q., **I. Wendelhag**, **J. Wikstrand**, and **T. Gustavsson** (2000). ”A multiscale dynamic programming procedure for boundary detection in ultrasonic artery images”. *IEEE transactions on medical imaging*, **19**(2), 127–142.

Liu, F., **D. Xu**, **M. S. Ferguson**, **B. Chu**, **T. Saam**, **N. Takaya**, **T. S. Hatsukami**, **C. Yuan**, and **W. S. Kerwin** (2006). ”Automated in vivo segmentation of carotid plaque mri with morphology-enhanced probability maps”. *Magnetic Resonance in Medicine*, **55**(3), 659–668.

Lizzi, F. L. and **D. J. Coleman** (2004). ”History of ophthalmic ultrasound”. *Journal of ultrasound in medicine*, **23**(10), 1255–1266.

Loizou, C. P., **T. Kasparis**, **C. Spyrou**, and **M. Pantziaris**, ”Integrated system for the complete segmentation of the common carotid artery bifurcation in ultrasound images”. *In IFIP International Conference on Artificial Intelligence Applications and Innovations*. Springer, 2013.

Loizou, C. P. and **M. Pantziaris** (2015). ”An integrated system for the complete segmentation of the common carotid artery bifurcation in ultrasound images”. *Journal of Biomedical Engineering and Informatics*, **1**(1), 1–11.

Losordo, D. W., **K. Rosenfield**, **J. Kaufman**, **A. Pieczek**, and **J. M. Isner** (1994). ”Focal compensatory enlargement of human arteries in response to progressive atherosclerosis. in vivo documentation using intravascular ultrasound”. *Circulation*, **89**(6), 2570–2577.

Maiellaro, K. and **W. R. Taylor** (2007). ”The role of the adventitia in vascular inflammation”. *Cardiovascular research*, **75**(4), 640–648.

Manjón, J. V., **J. Carbonell-Caballero**, **J. J. Lull**, **G. García-Martí**, **L. Martí-Bonmatí**, and **M. Robles** (2008). "MRI denoising using non local means". *Medical Image Analysis*, **12**(4).

Mehra, S. (2010). "Role of duplex doppler sonography in arterial stenoses". *Journal Indian Academy of Clinical Medicine*, **11**(4), 294–299.

Meiburger, K. M., **F. Molinari**, **U. R. Acharya**, **L. Saba**, **P. Rodrigues**, **W. Liboni**, **A. Nicolaides**, and **J. S. Suri** (2011). "Automated carotid artery intima layer regional segmentation". *Physics in medicine and biology*, **56**(13), 40–73.

Michailovich, O. V. and **A. Tannenbaum** (2006). "Despeckling of medical ultrasound images". *IEEE Transactions on Ultrasonics, Ferroelectrics, and Frequency Control*, **53**(1), 64–78.

Milkowski, A., **Y. Li**, **D. Becker**, and **S. O. Ishrak** (2009). "Speckle reduction imaging". *Technical White Paper–General Electric Health Care (Ultrasound). Last accessed on July*, **9**, 26.

Molinari, F., **G. Krishnamurthi**, **U. R. Acharya**, **S. V. Sree**, **G. Zeng**, **L. Saba**, **A. Nicolaides**, and **J. S. Suri** (2012*a*). "Hypothesis validation of far-wall brightness in carotid-artery ultrasound for feature-based imt measurement using a combination of level-set segmentation and registration". *IEEE Transactions on Instrumentation and Measurement*, **61**(4), 1054–1063.

Molinari, F., **K. M. Meiburger**, **L. Saba**, **U. R. Acharya**, **M. Ledda**, **A. Nicolaides**, and **J. S. Suri** (2012*b*). "Constrained snake vs. conventional snake for carotid ultrasound automated imt measurements on multi-center data sets". *Ultrasonics*, **52**(7), 949–961.

Molinari, F., **K. M. Meiburger**, **L. Saba**, **G. Zeng**, **U. R. Acharya**, **M. Ledda**, **A. Nicolaides**, and **J. S. Suri** (2012*c*). "Fully automated dual-snake formulation for carotid intima-media thickness measurement a new approach". *Journal of Ultrasound in Medicine*, **31**(7), 1123–1136.

Molinari, F., **K. M. Meiburger**, **G. Zeng**, **A. Nicolaides**, and **J. S. Suri**, "Caudles-ef: carotid automated ultrasound double line extraction system using edge flow". *In Ultrasound Imaging*. Springer, 2012*d*, 129–162.

Molinari, F., **K. M. Meiburger**, **G. Zeng**, **L. Saba**, **U. R. Acharya**, **L. Famiglietti**, **N. Georgiou**, **A. Nicolaides**, **R. S. Mamidi**, **H. Kuper**, *et al.* (2012*e*). "Automated carotid imt measurement and its validation in low contrast ultrasound database of 885 patient indian population epidemiological study: results of atheroedge software". *International angiology: a journal of the International Union of Angiology*, **31**(1), 42–53.

Molinari, F., **C. S. Pattichis**, **G. Zeng**, **L. Saba**, **U. R. Acharya**, **R. Sanfilippo**, **A. Nicolaides**, and **J. S. Suri** (2012*f*). "Completely automated multiresolution edge snappera new technique for an accurate carotid ultrasound imt measurement: clinical validation and benchmarking on a multi-institutional database". *IEEE Transactions on Image Processing*, **21**(3), 1211–1222.

Molinari, F., **G. Zeng**, and **J. S. Suri** (2010*a*). "A state of the art review on intima–media thickness (imt) measurement and wall segmentation techniques for carotid ultrasound". *Computer methods and programs in biomedicine*, **100**(3), 201–221.

Molinari, F., **G. Zeng**, and **J. S. Suri** (2010*b*). "An integrated approach to computer-based automated tracing and its validation for 200 common carotid arterial wall ultrasound images a new technique". *Journal of Ultrasound in Medicine*, **29**(3), 399–418.

Molinari, F., **G. Zeng**, and **J. S. Suri** (2011). "Inter-greedy technique for fusion of different segmentation strategies leading to high-performance carotid imt measurement in ultrasound images". *Journal of medical systems*, **35**(5), 905–919.

Mughal, M. M., **M. K. Khan**, **J. K. DeMarco**, **A. Majid**, **F. Shamoun**, and **G. S. Abela** (2011). "Symptomatic and asymptomatic carotid artery plaque". *Expert review of cardiovascular therapy*, **9**(10), 1315–1330.

Mumford, D. and **J. Shah** (1989). "Optimal approximations by piecewise smooth functions and associated variational problems". *Communications on pure and applied mathematics*, **42**(5), 577–685.

Naghavi, M., **P. Libby**, **E. Falk**, **S. W. Casscells**, **S. Litovsky**, **J. Rumberger**, **J. J. Badimon**, **C. Stefanadis**, **P. Moreno**, **G. Pasterkamp**, *et al.* (2003). "From vulnerable plaque to vulnerable patient a call for new definitions and risk assessment strategies: part i". *Circulation*, **108**(14), 1664–1672.

Nambi, V., **L. Chambless**, **A. R. Folsom**, **M. He**, **Y. Hu**, **T. Mosley**, **K. Volcik**, **E. Boerwinkle**, and **C. M. Ballantyne** (2010). "Carotid intima-media thickness and presence or absence of plaque improves prediction of coronary heart disease risk: the aric (atherosclerosis risk in communities) study". *Journal of the American College of Cardiology*, **55**(15), 1600–1607.

Nguyen, K. T., **C. D. Clark**, **T. J. Chancellor**, and **D. V. Papavassiliou** (2008). "Carotid geometry effects on blood flow and on risk for vascular disease". *Journal of biomechanics*, **41**(1), 11–19.

Nicolaides, A., **K. W. Beach**, **E. Kyriacou**, and **C. S. Pattichis**, *"Ultrasound and carotid bifurcation atherosclerosis"*. Springer Science & Business Media, 2011.

Orel, S. G. and **M. D. Schnall** (2001). "MR imaging of the breast for the detection, diagnosis, and staging of breast cancer 1". *Radiology*, **220**(1), 13–30.

Organization, W. H. and **UNAIDS**, *"Prevention of cardiovascular disease"*. World Health Organization, 2007.

Papadopoulos, H., **A. S. Andreou**, **L. Iliadis**, and **I. Maglogiannis**, *"Artificial Intelligence Applications and Innovations: 9th IFIP WG 12.5 International Conference, AIAI 2013, Paphos, Cyprus, September 30–October 2, 2013, Proceedings"*, volume 412. Springer, 2013.

Parker, D. L. and **G. T. Gullberg** (1990). ”Signal-to-noise eficiency in magnetic resonance imaging”. *Medical Physics*, **17**(2), 250–257.

Pasterkamp, G., **P. J. Wensing**, **M. J. Post**, **B. Hillen**, **W. P. Mali**, and **C. Borst** (1995). ”Paradoxical arterial wall shrinkage may contribute to luminal narrowing of human atherosclerotic femoral arteries”. *Circulation*, **91**(5), 1444–1449.

Patil, P. and **B. Dasgupta** (2012). ”Role of diagnostic ultrasound in the assessment of musculoskeletal diseases”. *Therapeutic advances in musculoskeletal disease*, **4**(5), 341–355.

Pizurica, A., **W. Philips**, **I. Lemahieu**, and **M. Acheroy** (2003). ”A versatile wavelet domain noise filtration technique for medical imaging”. *IEEE transactions on medical imaging*, **22**(3), 323–331.

Polak, J. F., *”Peripheral vascular sonography”*. Lippincott Williams & Wilkins, 2004.

Polak, J. F., **R. A. Kronmal**, **G. S. Tell**, **D. H. O’Leary**, **P. J. Savage**, **J. M. Gardin**, **G. H. Rutan**, **N. O. Borhani**, *et al.* (1996). ”Compensatory increase in common carotid artery diameter relation to blood pressure and artery intima-media thickness in older adults”. *Stroke*, **27**(11), 2012–2015.

Polak, J. F., **A. Meisner**, **M. J. Pencina**, **P. A. Wolf**, and **R. B. D’agostino** (2012). ”Variations in common carotid artery intima-media thickness during the cardiac cycle: implications for cardiovascular risk assessment”. *Journal of the American Society of Echocardiography*, **25**(9), 1023–1028.

Polak, J. F., **R. L. Sacco**, **W. S. Post**, **D. Vaidya**, **M. K. Arnan**, and **D. H. OLeary** (2014). ”Incident stroke is associated with common carotid artery diameter and not common carotid artery intima-media thickness”. *Stroke*, **45**(5), 1442–1446.

Polak, J. F., **L. Shemanski**, **D. H. O’Leary**, **D. Lefkowitz**, **T. R. Price**, **P. J. Savage**, **W. E. Brant**, and **C. Reid** (1998). ”Hypoechoic plaque at us of the carotid artery: an in-

dependent risk factor for incident stroke in adults aged 65 years or older. cardiovascular health study". *Radiology*, **208**(3), 649–654.

Prosi, M., **K. Perktold**, and **H. Schima** (2007). "Effect of continuous arterial blood flow in patients with rotary cardiac assist device on the washout of a stenosis wake in the carotid bifurcation: a computer simulation study". *Journal of biomechanics*, **40**(10), 2236–2243.

Rajan, J., **A. J. den Dekker**, and **J. Sijbers** (2014). "A new non-local maximum likelihood estimation method for rician noise reduction in magnetic resonance images using the kolmogorov-smirnov test". *Signal Processing*, **103**, 16–23.

Rajan, J., **B. Jeurissen**, **M. Verhoye**, **J. Van Audekerke**, and **J. Sijbers** (2011). "Maximum likelihood estimation-based denoising of magnetic resonance images using restricted local neighborhoods". *Physics in Medicine and Biology*, **56**(16).

Rajan, J., **J. Veraart**, **J. Van Audekerke**, **M. Verhoye**, and **J. Sijbers** (2012). "Non-local maximum likelihood estimation method for denoising multiple-coil magnetic resonance images". *Magnetic Resonance Imaging*, **30**(10), 1512–1518.

Rayleigh, L. (1945). "The theory of sound. vol. 2. 1896". *Reprinted, Dover, New York*.

Rice, S. O. (1944). "Mathematical analysis of random noise". *Bell System Technical Journal*, **23**(3).

Rocha, R., **A. Campilho**, **J. Silva**, **E. Azevedo**, and **R. Santos** (2011). "Segmentation of ultrasound images of the carotid using ransac and cubic splines". *Computer methods and programs in biomedicine*, **101**(1), 94–106.

Rocha, R., **J. Silva**, and **A. Campilho** (2012). "Automatic segmentation of carotid b-mode images using fuzzy classification". *Medical & biological engineering & computing*, **50**(5), 533–545.

Rocha, R., **J. Silva**, and **A. Campilho** (2014). "Automatic detection of the carotid lumen axis in b-mode ultrasound images". *Computer methods and programs in biomedicine*, **115**(3), 110–118.

Saba, L., **H. Gao**, **E. Raz**, **S. V. Sree**, **L. Mannelli**, **N. Tallapally**, **F. Molinari**, **P. P. Bassareo**, **U. R. Acharya**, **H. Poppert**, *et al.* (2014*a*). "Semiautomated analysis of carotid artery wall thickness in MRI". *Journal of Magnetic Resonance Imaging*, **39**(6), 1457–1467.

Saba, L., **R. Montisci**, **F. Molinari**, **N. Tallapally**, **G. Zeng**, **G. Mallarini**, and **J. S. Suri** (2012). "Comparison between manual and automated analysis for the quantification of carotid wall by using sonography. a validation study with ct". *European journal of radiology*, **81**(5), 911–918.

Saba, L., **J. M. Sanches**, **L. M. Pedro**, and **J. S. Suri**, *"Multi-modality atherosclerosis imaging and diagnosis"*. Springer, 2014*b*.

Sanches, J. M., **A. F. Laine**, and **J. S. Suri**, *"Ultrasound imaging: advances and applications"*. Springer Science & Business Media, 2011.

Santos, A. M., **J. M. R. Tavares**, **L. Sousa**, **R. Santos**, **P. Castro**, and **E. Azevedo**, "Automatic segmentation of the lumen of the carotid artery in ultrasound b-mode images". *In SPIE Medical Imaging*. Computer-Aided Diagnosis, International Society for Optics and Photonics, 86703I, 2013.

Sarkar, S., **S. Ghosh**, **S. K. Ghosh**, and **A. Collier** (2007). "Role of transcranial doppler ultrasonography in stroke". *Postgraduate medical journal*, **83**(985), 683–689.

Selzer, R. H., **W. J. Mack**, **P. L. Lee**, **H. Kwong-Fu**, and **H. N. Hodis** (2001). "Improved common carotid elasticity and intima-media thickness measurements from computer analysis of sequential ultrasound frames". *Atherosclerosis*, **154**(1), 185–193.

Shaalan, W. E., **C. M. Wahlgren**, **T. Desai**, **G. Piano**, **C. Skelly**, and **H. S. Bassiouny** (2008). "Reappraisal of velocity criteria for carotid bulb/internal carotid artery steno-

sis utilizing high-resolution b-mode ultrasound validated with computed tomography angiography". *Journal of vascular surgery*, **48**(1), 104–112.

Shankar, P. M. (2000). "A general statistical model for ultrasonic backscattering from tissues". *IEEE transactions on ultrasonics, ferroelectrics, and frequency control*, **47**(3), 727–736.

Sidhu, P. S. (2000). "Ultrasound of the carotid and vertebral arteries". *British medical bulletin*, **56**(2), 346–366.

Sifakis, E. G. and **S. Golemati** (2014). "Robust carotid artery recognition in longitudinal b-mode ultrasound images". *IEEE Transactions on Image Processing*, **23**(9), 3762–3772.

Sigmund, O. (2007). "Morphology-based black and white filters for topology optimization". *Structural and Multidisciplinary Optimization*, **33**(4-5), 401–424.

Sijbers, J. and **A. J. den Dekker** (2004). "Maximum likelihood estimation of signal amplitude and noise variance from MR data". *Magnetic Resonance in Medicine*, **51**(3), 586–594.

Sijbers, J., **A. J. den Dekker**, **P. Scheunders**, and **D. Van Dyck** (1998). "Maximum likelihood estimation of Rician distribution parameters". *IEEE Transactions on Medical Imaging*, **17**(3), 357–361.

Slovut, D. P., **J. M. Romero**, **K. M. Hannon**, **J. Dick**, and **M. R. Jaff** (2010). "Detection of common carotid artery stenosis using duplex ultrasonography: a validation study with computed tomographic angiography". *Journal of vascular surgery*, **51**(1), 65–70.

Soille, P., *"Morphological image analysis: principles and applications"*. Springer Science & Business Media, 2013.

Soorajkumar, R., **P. Krishnakumar**, **D. Girish**, and **J. Rajan** (2016*a*). ”Coupled pde for ultrasound despeckling using eni classification”. *Procedia Computer Science*, **89**, 658–665.

Soorajkumar, R., **P. K. Kumar**, **D. Girish**, and **J. Rajan**, ”Fourth order pde based ultrasound despeckling using eni classification”. *In Signal Processing and Communications (SPCOM), 2016 International Conference on*. IEEE, 2016*b*.

Staff, B. (2014). ”Blausen gallery 2014”. *Wikiversity Journal of Medicine*, **1**.

Staub, D., **M. B. Patel**, **A. Tibrewala**, **D. Ludden**, **M. Johnson**, **P. Espinosa**, **B. Coll**, **K. A. Jaeger**, and **S. B. Feinstein** (2010). ”Vasa vasorum and plaque neovascularization on contrast-enhanced carotid ultrasound imaging correlates with cardiovascular disease and past cardiovascular events”. *Stroke*, **41**(1), 41–47.

Stein, J. H., **C. E. Korcarz**, **R. T. Hurst**, **E. Lonn**, **C. B. Kendall**, **E. R. Mohler**, **S. S. Najjar**, **C. M. Rembold**, and **W. S. Post** (2008). ”Use of carotid ultrasound to identify subclinical vascular disease and evaluate cardiovascular disease risk: a consensus statement from the american society of echocardiography carotid intima-media thickness task force endorsed by the society for vascular medicine”. *Journal of the American Society of Echocardiography*, **21**(2), 93–111.

Sudeep, P., **P. Palanisamy**, **J. Rajan**, **H. Baradaran**, **L. Saba**, **A. Gupta**, and **J. S. Suri** (2016). ”Speckle reduction in medical ultrasound images using an unbiased non-local means method”. *Biomedical Signal Processing and Control*, **28**, 1–8.

Suri, J., **C. Kathuria**, and **F. Molinari**, *”Atherosclerosis disease management”*. Springer Science & Business Media, 2010.

Suri, J. S., **R. M. Haralick**, and **F. H. Sheehan** (2000). ”Greedy algorithm for error correction in automatically produced boundaries from low contrast ventriculograms”. *Pattern Analysis & Applications*, **3**(1), 39–60.

Suri, J. S., **C. Yuan**, and **D. L. Wilson**, *"Plaque imaging: pixel to molecular level"*, volume 113. IOS Press, 2005.

Swinscow, T. D. V., **M. J. Campbell**, *et al.*, *"Statistics at square one"*. Bmj London, 2002.

Takiuchi, S., **K. Kamide**, **Y. Miwa**, **M. Tomiyama**, **M. Yoshii**, **T. Matayoshi**, **T. Horio**, and **Y. Kawano** (2004). "Diagnostic value of carotid intima–media thickness and plaque score for predicting target organ damage in patients with essential hypertension". *Journal of human hypertension*, **18**(1), 17–23.

Tao, Z., **H. D. Tagare**, and **J. D. Beaty** (2006). "Evaluation of four probability distribution models for speckle in clinical cardiac ultrasound images". *IEEE transactions on medical imaging*, **25**(11), 1483–1491.

Tay, P. C., **C. D. Garson**, **S. T. Acton**, and **J. A. Hossack** (2010). "Ultrasound despeckling for contrast enhancement". *IEEE Transactions on Image Processing*, **19**(7), 1847–1860.

Treeby, B. E., **J. Jaros**, **A. P. Rendell**, and **B. Cox** (2012). "Modeling nonlinear ultrasound propagation in heterogeneous media with power law absorption using a k-space pseudospectral method". *The Journal of the Acoustical Society of America*, **131**(6), 4324–4336.

Ukwatta, E., **J. Yuan**, **M. Rajchl**, **W. Qiu**, **D. Tessier**, and **A. Fenster** (2013). "3-D carotid multi-region MRI segmentation by globally optimal evolution of coupled surfaces". *IEEE transactions on medical imaging*, **32**(4), 770–785.

Underhill, H. R., **W. S. Kerwin**, **T. S. Hatsukami**, and **C. Yuan** (2006). "Automated measurement of mean wall thickness in the common carotid artery by mri: A comparison to intima-media thickness by b-mode ultrasound". *Journal of Magnetic Resonance Imaging*, **24**(2), 379–387.

van't Klooster, R., **P. J. de Koning**, **R. A. Dehnavi**, **J. T. Tamsma**, **A. de Roos**, **J. H. Reiber**, and **R. J. van der Geest** (2012). "Automatic lumen and outer wall segmentation of the carotid artery using deformable three-dimensional models in MR angiography and vessel wall images". *Journal of Magnetic Resonance Imaging*, **35**(1), 156–165.

Vicenzini, E., **M. F. Giannoni**, **F. Puccinelli**, **M. C. Ricciardi**, **M. Altieri**, **V. Di Piero**, **B. Gossetti**, **F. B. Valentini**, and **G. L. Lenzi** (2007). "Detection of carotid adventitial vasa vasorum and plaque vascularization with ultrasound cadence contrast pulse sequencing technique and echo-contrast agent". *Stroke*, **38**(10), 2841–2843.

Wang, Z., **A. Bovik**, **H. R. Sheik**, and **E. P. Simoncelli** (2004). "Image quality assessment: from error visibility to structural similarity". *IEEE Transactions on Image Pocessing*, **13**(4).

Ward, M. R., **G. Pasterkamp**, **A. C. Yeung**, and **C. Borst** (2000). "Arterial remodeling mechanisms and clinical implications". *Circulation*, **102**(10), 1186–1191.

Warlow, C. (1991). "Mrc european carotid surgery trial: interim results for symptomatic patients with severe (70-99%) or with mild (0-29%) carotid stenosis". *The Lancet*, **337**(8752), 1235–1243.

Wasserman, B. A., **R. J. Wityk**, **H. H. Trout**, and **R. Virmani** (2005). "Low-grade carotid stenosis looking beyond the lumen with mri". *Stroke*, **36**(11), 2504–2513.

Weismann, C., **C. Mayr**, **H. Egger**, and **A. Auer** (2011). "Breast sonography–2d, 3d, 4d ultrasound or elastography?". *Breast Care*, **6**(2), 98–103.

Whittaker, J. L., *"Ultrasound imaging for rehabilitation of the lumbopelvic region: a clinical approach"*. Elsevier Health Sciences, 2007.

WHO (2016). "WHO fact sheet". `http://www.who.int/mediacentre/factsheets/fs317/en/`. Reviewed June 2016.

Woollard, K. J. and **F. Geissmann** (2010). ”Monocytes in atherosclerosis: subsets and functions”. *Nature Reviews Cardiology*, **7**(2), 77–86.

You, Y.-L. and **M. Kaveh** (2000). ”Fourth-order partial differential equations for noise removal”. *IEEE Transactions on Image Processing*, **9**(10), 1723–1730.

Yuan, C., **E. Lin**, **J. Millard**, and **J.-N. Hwang** (1999). ”Closed contour edge detection of blood vessel lumen and outer wall boundaries in black-blood mr images”. *Magnetic Resonance Imaging*, **17**(2), 257–266.

Yuan, C., **M. Oikawa**, **Z. Miller**, and **T. Hatsukami** (2008). ”MRI of carotid atherosclerosis”. *Journal of nuclear cardiology*, **15**(2), 266–275.

Zahnd, G., **M. Orkisz**, **A. Sérusclat**, **P. Moulin**, and **D. Vray** (2014). ”Simultaneous extraction of carotid artery intima-media interfaces in ultrasound images: assessment of wall thickness temporal variation during the cardiac cycle”. *International journal of computer assisted radiology and surgery*, **9**(4), 645–658.

Zhang, J., **G. Lin**, **L. Wu**, **C. Wang**, and **Y. Cheng** (2015). ”Wavelet and fast bilateral filter based de-speckling method for medical ultrasound images”. *Biomedical Signal Processing and Control*, **18**, 1–10.

Zimmer, S., **S. Didas**, and **J. Weickert**, ”A rotationally invariant block matching strategy improving image denoising with non-local means”. *In International Workshop on Local and Non-Local Approximation in Image Processing*. Switzerland, 2008.

PUBLICATIONS BASED ON THIS THESIS

Journal Papers

1. **P. Krishna Kumar**, P. Darshan, Sheethal Kumar, Rahul Ravindra, Jeny Rajan, Luca Saba, Jasjit S. Suri, Magnetic resonance image denoising using nonlocal maximum likelihood paradigm in DCTframework, *International Journal of Imaging Systems and Technology*, 25(3), 256-264, August 2015.

2. **P. Krishna Kumar**, Tadashi Araki, Jeny Rajan, Luca Saba, Francesco Lavra, Nobutaka Ikeda, Aditya M. Sharma, Shoaib Shafique, Andrew Nicolaides, John R. Laird, Ajay Gupta, Jasjit S. Suri, Accurate lumen diameter measurement in curved vessels in carotid ultrasound: an iterative scale-space and spatial transformation approach, *Medical & Biological Engineering & Computing*, 55(8), 1415-1434, August 2017.

3. Tadashi Araki, **P. Krishna Kumar**, Harman S. Suri, Nobutaka Ikeda, Ajay Gupta, Luca Saba, Jeny Rajan, Francesco Lavra, Aditya M. Sharma, Shoaib Shafique, Andrew Nicolaides, John R. Laird, Jasjit S. Suri, Two automated techniques for carotid lumen diameter measurement: regional versus boundary approaches, *Journal of Medical Systems*, 40(7), 1-19, July 2016.

4. Aditya M. Sharma, Ajay Gupta, **P. Krishna Kumar**, Jeny Rajan, Luca Saba, Nobutaka Ikeda, John R. Laird, Andrew Nicolades, Jasjit S. Suri, A review on carotid ultrasound atherosclerotic tissue characterization and stroke risk stratification in machine learning framework, *Current Atherosclerosis Reports*, 17(9), 1-13, September 2015.

5. Luca Saba, Tadashi Araki, **P. Krishna Kumar**, Jeny Rajan, Francesco Lavra, Nobutaka Ikeda, Aditya M. Sharma, Shoaib Shafique, Andrew Nicolaides, John R. Laird, Ajay Gupta, Jasjit S. Suri, Carotid interadventitial diameter is more strongly related to plaque score than lumen diameter: An automated tool for stroke analysis, *Journal of Clinical Ultrasound*, 44(4), 210-220, February 2016.

6. Tadashi Araki, Asheed M. Kumar, **P. Krishna Kumar**, Ajay Gupta, Luca Saba, Jeny Rajan, Francesco Lavra, Aditya M. Sharma, Shoaib Shafique, Andrew Nicolaides, John R Laird, Jasjit S Suri, Ultrasound-based automated carotid lumen diameter/stenosis measurement and its validation system, *Journal for Vascular Ultrasound*, 40(3), 120-134, September 2016.

Conference Papers

1. **P. Krishna Kumar**, C. Kesavadas and Jeny Rajan, A Semi-automatic Method for Carotid Artery Wall Segmentation in MR Images, *Proceedings of IEEE India Conference (INDICON), Thirteenth International*, IISc Bangalore, December 2016, 1-6.

Abstracts

1. Aditya M. Sharma, Tadashi Araki, **P. Krishna Kumar**, Nobutaka Ikeda, Francesco Lavra, Jeny Rajan, Luca Saba, Andrew Nicolaides, John R. Laird, Shoaib Shafique, Jasjit S. Suri, Accurate Measurement of Carotid Lumen Diameter and Narrowing Utilizing Ultrasound, *Arteriosclerosis, Thrombosis, and Vascular Biology*, 35(S1), May 2015, A509-A509.

CURRICULUM VITAE

KRISHNA KUMAR P
Perikamana, Madhurakkad,
Haripuram (PO), Anandasram,
Kasaragod, Kerala, India-671531.
Email: krishnakumarkkp@gmail.com
Mobile: 9916770272.

Academic Records

1. M.Tech. in Computer Vision and Image Processing from Amrita Vishwa Vidyapeetham, Coimbatore, Tamilnadu, India, Aug 2011- Jul 2013 (CGPA: 8.8/10).
2. B.Tech. in Electronics and Communication Engineering from Govt. Engineering College Kannur, Kerala, India, Aug 2006- May 2010 (Percentage: 73.17%).

Research Interests

Medical Image Processing, Computer Vision, Video Processing.

Programming Languages

C, CPP, Matlab, Open CV, Phython.